The insulator-metal phase transition in VO_2 measured at nanometer length scales and femtosecond time scales

by

Luciana Vidas

Thesis supervisor:
Dr. Simon Wall

A thesis submitted in fulfilment of the requirements for the degree of Doctor of Philosophy in

Ultrafast Dynamics of Quantum Solids

ICFO – Institut de Ciències Fotòniques
UPC – Universitat Politècnica de Catalunya

Barcelona, February 2019

Thesis committee:

Dr. Roman Bertoni (Institut de Physique de Rennes, France)
Prof. Dr. Kai Rossnagel (DESY – Deutsches Elektronen-Synchrotron, Germany)
Prof. Dr. Adrian Bachtold (ICFO – Institut de Ciències Fotòniques, Spain)

Abstract

The physics of transition-metal oxides presents a challenge to our current understanding of condensed matter physics. The main difficulty arises from a competition between electron-electron and electron-phonon interactions to dictate the properties of these complex materials. This issue is particularly apparent in vanadium dioxide, which undergoes an electronic and structural phase transition close to room temperature. Despite more than 50 years of research, the origin of the transformation is still actively debated, with contradictory interpretations often reported.

The main goal of this thesis is to re-evaluate the phase transition in VO_2 with a combination of new experimental techniques, ranging from the mid-infrared to hard x-rays, that can probe the transformation at nanometer length scales and femtosecond time-scales. This allows to disentangle the roles of phase separation, laser-induced heat, and electron and phonon dynamics to the insulator-metal transition. The results from these experiments provide a unified and new picture of the nature of this process, both in and out of equilibrium, in which the electron-phonon interactions are the main driving mechanism.

Furthermore, the new techniques and analysis presented here for VO_2 can be applied to the study of other controversial complex materials that exhibit remarkable properties, and answer thereby some of the key outstanding questions in condensed matter physics.

Resumen

La física de los óxidos de metales de transición constituye un gran desafío a nuestra comprensión actual de la materia condensada. El mayor obstáculo surge de la competición entre las interacciones electrón-electrón y electrón-fonón para dictar las propiedades de tales materiales complejos. Este problema es particularmente evidente en el dióxido de vanadio, el cual experimenta una transición de fase tanto electrónica como estructural a una temperatura ligeramente superior a la ambiente. A pesar de más de 50 años de investigaciones, el origen de la transformación sigue siendo motivo de debate, con multitud de interpretaciones a menudo contradictorias.

El objetivo principal de esta tesis es reevaluar la transición aislante-metal de VO_2 empleando una combinación de técnicas experimentales nuevas, desde la región del infrarrojo medio a los rayos X duros, que permiten el estudio de la transición de fase a escalas nanométricas y en tiempos de femtosegundos. Esto facilita el esclarecimiento de los roles que desempeñan aspectos como la separación de fases, el calor inducido por láser y las dinámicas de electrones y fonones en la transición de fase de VO_2. Los resultados de estos experimentos ofrecen una visión unificada sobre la naturaleza de este fenómeno, tanto en equilibrio como fuera de él, en la que la interacción de los electrones con fonones son el principal mecanismo responsable de impulsar la transición.

Asimismo, los análisis y técnicas nuevos presentados en esta tesis para el estudio de VO_2 pueden ser empleados para la investigación de otros materiales complejos que también exhiben propiedades extraordinarias y cuyo entendimiento presenta serias controversias. De esta manera, se daría respuesta a algunas de las preguntas clave pendientes de la física de la materia condensada.

Contents

List of Figures

Introduction

Transition-metal oxides (TMOs) exhibit some of the most intriguing phenomena observed in condensed matter, which arise from the complex interplay of electron and lattice degrees of freedom. In the last few decades, several materials have been discovered with remarkable exotic properties, such as high-temperature superconductivity, colossal magneto-resistance, charge and orbital ordering, or insulator-metal transitions. These extraordinary phenomena have the potential to revolutionize both the technology of the future, as well as our approach to condensed matter physics. However, such properties cannot be currently harnessed for the design of novel solid-state devices due to the lack of a proper theoretical framework that explains the behaviour of these complex materials.

Band-structure theory successfully predicts the properties of materials in which one basic physical interaction is clearly dominant over all the others. For instance, insulators and metals are considered systems with weakly interacting localized and delocalized wave-functions, respectively, in which the bands are set by the symmetry of the lattice, but otherwise fixed. Thus, their insulating or metallic nature is simply the result of the position of the Fermi energy within the band structure. The simple application of band theory does not describe correctly the properties of TMOs, for which often a metallic state is predicted when the material is actually an insulator. Furthermore, in this type of systems, changes in doping and/or temperature can lead to phase transitions. This occurs due to multiple degrees of freedom interacting on similar energy scales that strongly affect the physical properties of these materials.

Traditionally, the missing component for the theoretical models to work was believed to be related to electronic correlations. This has given rise to the concept of *strongly correlated materials*. The well-known Mott insulators belong to this group. These are materials predicted to be metals by conventional band theory due to the non consideration of electron-electron interactions, but show an insulating behaviour. However, besides these neglected interactions,

it is also worth considering the fact that in order to make band-theory calculations mathematically tractable, approximations on phonon interactions are also needed. This simplification could also explain the observed deviations of experiments from theory without the need of adding electronic-correlations-related components.

One of the key challenges in condensed matter physics is to determine the relative contributions of electron-electron and electron-phonon interactions, typified by two simplified theoretical models that capture the basic concepts of these physical interactions. This is known as the *Mott vs Peierls competition*. While in the former, strong Coulomb interactions between electrons stand as the cause of the observed properties, in the latter scenario the crystallographic distortion and electron-phonon interactions are responsible for determining the specific behaviour of the material (see Fig. 1).

One of the first materials in which the Mott *vs* Peierls competition was studied is vanadium dioxide (VO_2). VO_2 is a transition-metal oxide that undergoes an insulator-metal phase transition (IMT) at approximately 340 K. This effect was first discovered by Morin in 1959 [1], and shortly after, in 1961, it was shown that the system also undergoes a structural change [2]. For more than 50 years, an enormous amount of experimental and theoretical research has been devoted to determining the relative contributions of the electronic and structural degrees of freedom to this phase transition. In 1971, Goodenough was the first to propose a Peierls-like lattice distortion as the origin of the phenomenon [3], in which the dimerization, or pairing, of the vanadium atoms acts as the driving force for the phase transition. Nonetheless, some years later, in 1975, Zylbersztejn and Mott suggested that electronic correlations are the main responsible for opening the insulator band-gap, as in a typical Mott insulator, and proposed a Mott-Hubbard model for the description of the phase transition of VO_2 [4].

From the experimental side, results pointing to both scenarios have been reported. Driven by the discovery in 1971 that the insulator-metal transition in VO_2 can be induced by light pulses in an ultrafast way [5], a new approach was adopted for studying the phase transition. Probing the process out of equilibrium has enabled the separate examination of the electronic and lattice contributions, as the respective responses can be disentangled in the time domain.

VO_2 has in fact represented a key material for the development of ultrafast methods. However, the results provided by subsequent time-resolved studies of the phase transition have presented several discrepancies, and nowadays, a

unified description of this phenomenon still lacks. The aim of this thesis is to address the key challenges involved when examining the phase transition in VO_2, such as phase separation and coexistence, heat-related issues, and phonon dynamics. To this end, a broad range of techniques are applied to probe the different aspects of the material and build thereby a complete comprehension of the phase transition.

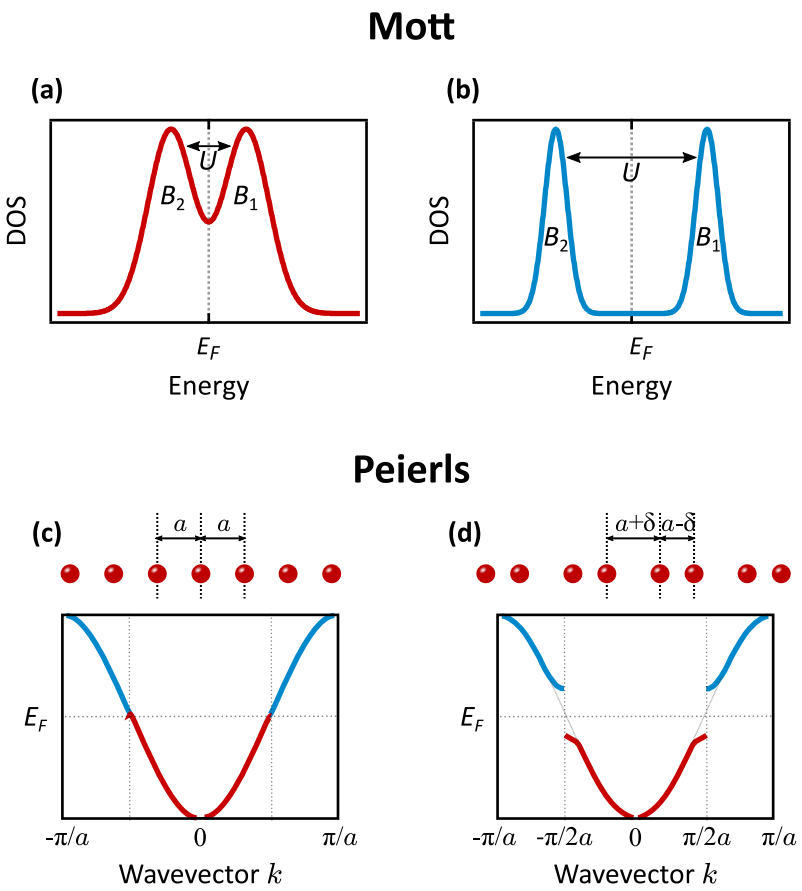

Fig. 1: The Mott *vs* Peierls competition. Mott: (a) In the metallic phase, large screening leads to delocalized bands with large bandwidths, B_1 and B_2, and weak repulsion U. **(b)** Screening reduction gives rise to a high Coulomb interaction, which localizes electrons and leads to the insulating phase. **Peierls: (c)** In the metallic state, the electron states are filled up to the Fermi energy, and the lattice is a periodic array of atoms with lattice constant a. **(d)** When lowering the temperature, the system gains energy by pairing the atoms, changing thereby the periodicity of the atomic chain. This effective doubling of the unit cell leads to the formation of band-gaps at half the original Brillouin zone.

Thesis outline

The structure of this thesis is organized as follows:

- Chapter 1 gives an introduction on the physics of VO_2 and the insulator-metal phase transition, together with the current state of the research. The specific challenges needed to be overcome for studying this phenomenon are described in detailed, as well as the methods proposed to do so.
- Chapter 2 presents the phenomena of phase separation and coexistence, which hinder the interpretation of measurements conducted on VO_2. A soft X-ray holographic imaging technique is successfully applied for the first time on VO_2 to address this issue.
- Chapter 3 focuses on the measurements of the threshold fluences required to drive the photo-induced phase transition, with the contribution of laser-induced heat issues. A pump-probe-measurement approach is employed over long time-scales to study heat dissipation dynamics, of particular importance in ultrafast experiments.
- Chapter 4 studies the dynamics of phonon interactions during the phase transition by means of time-resolved soft X-ray absorption spectroscopy, and ultrafast hard X-ray total scattering.
- Finally, chapter 5 summarizes the main achievements of the present thesis, along with a prospect of future experiments to be performed.

1 | An overview on VO_2

This chapter presents a summary of the extensive research performed on vanadium dioxide up to the present day. It involves more than 50 years of measurements, from which only the most relevant for the present work are mentioned. Section 1.1 is focused on the description of the physical properties of VO_2, as well as the theoretical models proposed for understanding the insulator-metal phase transition. The sequence of measurements and theoretical calculations points towards the importance of two different aspects regarding the phase transition that need careful consideration in order to understand the physical origin of the IMT: the existence of a transient monoclinic metallic phase, covered in Section 1.2, and the ultrafast dynamics of the photo-induced phase transition, introduced in Section 1.3.

1.1 The physics of VO_2

Vanadium dioxide is a correlated transition-metal oxide that exhibits an electronic and structural phase transition as a function of temperature. At approximately 340 K [1], VO_2 undergoes a first-order reversible phase transition from a low-temperature monoclinic M_1 phase to a high-temperature rutile R phase. Concurrently, an increase of up to five orders of magnitude of the conductivity occurs, switching the material from an insulator to a metal. The corresponding crystallographic structures for temperatures below and above T_c are displayed in Fig. 1.1, and the lattice parameters of each phase are summarized in Table 1.1. These values were obtained from X-ray diffraction experiments on VO_2 in the rutile [6, 7] and in the monoclinic phase [7, 8].

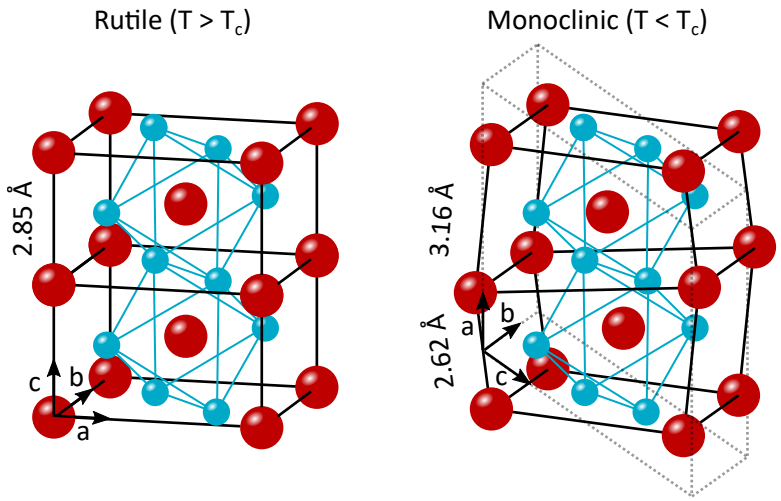

Fig. 1.1: Crystallographic structures of VO_2. Vanadium atoms are represented by the red balls, while the oxygen atoms are in blue. For temperatures above T_c, the material has a rutile structure (left), which transforms into a monoclinic lattice (right) when lowering the temperature below T_c. The unit cell is indicated by the dashed line.

Lattice	a (Å)	b (Å)	c (Å)
M_1	5.75	4.53	5.38
R	4.55	$= a$	2.85

Table 1.1: Lattice parameters of the monoclinic and rutile phases of VO_2 obtained by X-ray diffraction experiments [6, 8].

As in many transition-metal compounds, metal ions (vanadium in this case) are surrounded by oxygen anions (or ligands) forming an octahedral structure. At high temperature, the metallic phase has a rutile crystal structure, with each unit cell containing two vanadium and four oxygen atoms (Fig. 1.1). When the temperature is decreased below T_c, the vanadium atoms dimerize forming V-V pairs along the rutile c-axis with two different V-V bond lengths: a short intra-dimer length of 2.62 Å and a longer inter-dimer length of 3.16 Å, in contrast to the equally spaced V-V bonds from the rutile phase. This leads to the doubling of the unit cell, which now contains four vanadium and eight oxygen atoms. Dimerization is accompanied by a slight tilt of the dimers away from the c-axis in a zigzag-like pattern, resulting in one of the V-O separations shorter than the rest. As opposed to the vanadium ions, the oxygen atoms are only slightly disturbed across the phase transition. In the low-temperature M_1 phase, an insulating gap of ≈ 0.6 eV has been measured [9, 10]. Altogether, the crystallographic change from a monoclinic to a rutile structure constitutes an increase of symmetry and a volume change of $\sim 0.044\,\%$ [11, 12], as well as a transition from an insulating to a metallic electronic structure.

Whereas the crystal structures of VO_2 could be easily determined by X-ray diffraction measurements, the electronic configurations have been much more elusive, and different theoretical models have been proposed to describe them and the mechanism that drives the transformation from one phase to the other. A first description of the electronic structure in both phases was given by Goodenough based on crystal-field theory and the lattice distortion [3]. Later on, due in principle to the inability of this model to reproduce the right magnitude of the band-gap in the insulating phase, Mott and Zylbersztejn argued that electronic correlations must be included in the calculations [4]. The models proposed by Goodenough and Mott, which gave rise to the so-called Peierls *vs* Mott competition, are described in detail in the following.

1.1.1 Goodenough model

In order to understand the band-theory model proposed by Goodenough, a brief introduction to crystal-field theory is required. Vanadium, as a transition-metal ion, has five d orbitals: d_{xy}, d_{yz}, d_{xz}, $d_{x^2-y^2}$, and d_{z^2}. When isolated or surrounded by a field with spherical symmetry, these five orbitals have the same energy, i.e., they are degenerate. However, in the presence of an octahedral crystal field, as the one formed by the oxygen atoms in VO_2 (Fig. 1.1), this degeneracy is lifted due to the charge interactions of the metal cation and the ligands, in which the d-electrons closer to the ligands have a higher energy than

those further away. The V 3d orbitals are then split in energy into threefold-degenerate t_{2g} states, built from the $d_{x^2-y^2}$, d_{xz}, and d_{yz} orbitals, and twofold-degenerate e_g states, comprising the d_{xy} and d_{z^2} orbitals, as illustrated in Fig. 1.2. The latter have higher energy, as these orbitals are closer to the ligands and experience therefore more Coulomb repulsion.

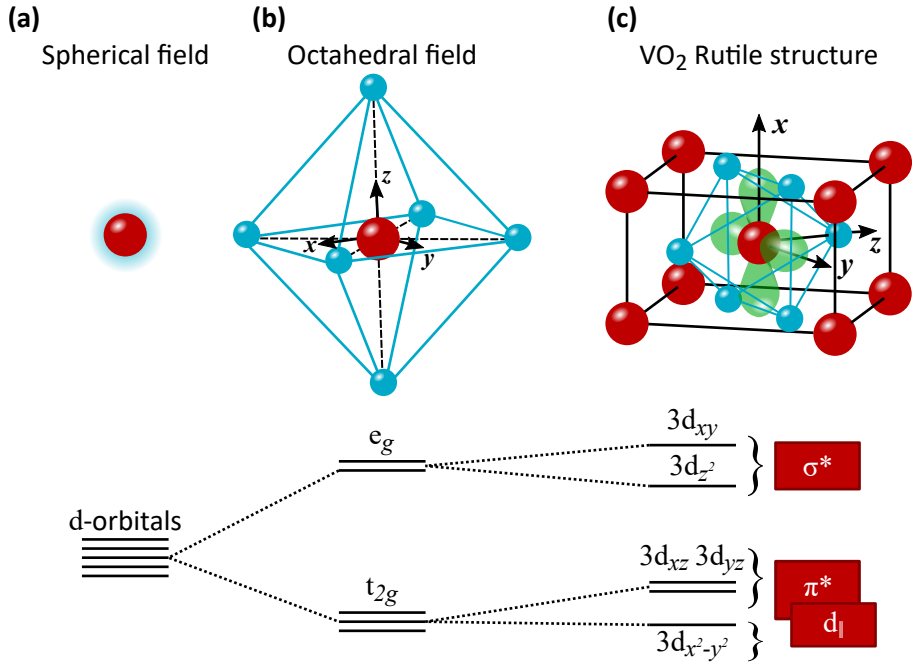

Fig. 1.2: Schematic energy levels of the d-orbitals in a transition-metal ion. **(a)** The five d-orbitals of the ion placed in a crystal field with spherical symmetry are degenerate. **(b)** When the ion is located within an octahedral crystal field, the d-orbitals are split into twofold-degenerate e_g orbitals and threefold-degenerate t_{2g} orbitals. **(c)** A distortion of the octahedron along the z-axis, as in the case of the rutile phase of VO_2, the orbitals degeneracies are further lifted. The crystal structure corresponds to the rutile unit cell with the c-axis along x, with the angular part of the $d_{\parallel} = d_{x^2-y^2}$ orbital represented. Adapted from [13].

According to Goodenough's model [3], schematically illustrated in Fig. 1.3, because of the orthorhombic component of the crystal field, the t_{2g} states are further split into two π^* states, formed by the $3d_{xz}$ and $3d_{yz}$ orbitals, which point in between the ligands and have a component along the z-axis, and one $d_{\parallel}$ state, formed by the relatively non-bonding $3d_{x^2-y^2}$ orbitals, which are parallel to the rutile c-axis and mediate hence the V-V bonds. On the other hand, the $3d_{z^2}$ and $3d_{xy}$ orbitals, that point towards the ligands, constitute the σ^* states, which, given their σ-bonding nature, present the strongest p-d overlap and the

largest energy difference between the bonding and antibonding orbitals.

During the insulator-metal transition, the vanadium atoms dimerize along the rutile *c*-axis, leading to the splitting of the $d_{\parallel}$ band into filled bonding and empty antibonding states. In addition, the tilting of the dimers in the zigzag pattern aforementioned increases the p-d bonding and leads to the lift in energy of the π^* states above the Fermi level (see Fig. 1.3(b)). This shift has been found to be of $\approx 0.5\,\text{eV}$, with the π^* band located at the lower edge of the conduction band, well below the antibonding $d_{\parallel}$ band [10, 13]. In addition, a change in the width of the π^* band is also found, narrowing from 2.5 eV in the rutile phase to 2 eV in the monoclinic phase. Therefore, the insulator state is regarded as the result of the vanadium zigzag distortion with the assistance of dimerization, and strong electron-phonon interactions as the driving mechanism for the phase transition.

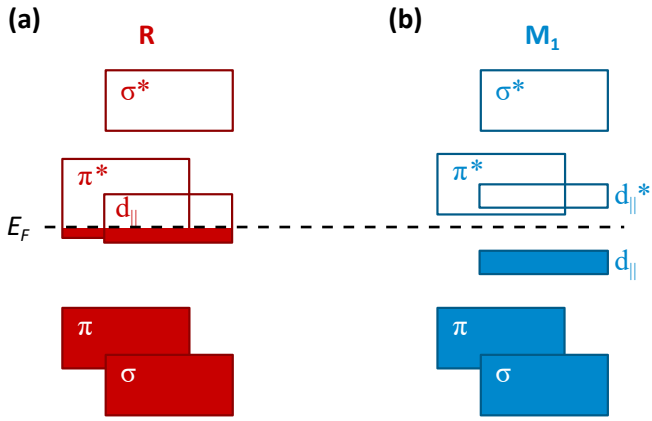

Fig. 1.3: Schematic of the band structures proposed by Goodenough above and below the phase transition. (a) In the rutile structure, VO_2 exhibits a metallic behaviour due to the location of the π^* and $d_{\parallel}$ states, crossing the Fermi level. **(b)** At temperatures below T_c, VO_2 has a monoclinic structure, in which the dimerization and tilting of the vanadium ions lead to the division of the $d_{\parallel}$ band and the upwards shift of the π^* states that result in the opening of an insulating band-gap.

It is worth mentioning that this model and later theoretical calculations built upon it [13, 14] are benefited from the very small mixing of these states, with the exception of the hybridization of the V 3d and O 2p orbitals that give rise to the π^* states. In fact, the $d_{\parallel}$ and π^* bands can be regarded as nearly independent, with a one-dimensional $d_{\parallel}$ band embedded in a three-dimensional background of π^* states, resulting in a proper scenario for a structural Peierls distortion. This, together with the fact that in d^1 compounds the energy gain

from lowering the occupied electronic states is larger than the energy cost of the lattice distortion, and the absence of magnetic properties in the insulating phase, makes VO_2 a suitable Peierls insulator. In materials that present such a Peierls instability, electron-phonon interactions act as the main force for the dimerization and resulting change in periodicity of the one-dimensional atoms chain [15, 16], as previously seen in Fig. 1.

Nonetheless, in the early days, these theoretical models within a band-structure framework were unable to explain both phases of VO_2 at the same time. Calculations based on density functional theory (DFT) within the local density approximation (LDA), despite yielding correct crystallographic structures and describing a significant distortion of the energy bands around the Fermi level [14], dramatically failed to reproduce a finite band-gap in the monoclinic structure required for the insulating behaviour observed [13, 14]. This fact led to the belief that the energy gain obtained via the lattice distortion was not enough to account for the opening of the band-gap, but calculations must include a parameter U associated to electronic interactions.

1.1.2 Mott scenario

In 1975, shortly after Goodenough's publication, Zylbersztejn and Mott proposed a Mott-Hubbard model to describe the phase transition in VO_2 [4]. While in single-electron band theory it is assumed that interactions between electrons can be represented by an average effective periodic potential, and that no dynamical interactions occur (which is actually the basis for DFT methods), the theoretical work presented by Mott placed electronic correlations as the primary force driving the phase transition in VO_2, with the lattice distortion only as a side effect [4].

In this scenario, VO_2 is described as a Mott insulator, in which the on-site Coulomb repulsion between electrons become comparable to the single-electron bandwidth, which makes necessary the addition of this term into the model. Therefore, the description of the system is based on a Hubbard's model for a system with interacting particles [17], represented by a two-terms Hamiltonian, which includes the tunnelling of electrons between sites of the lattice t, and the on-site Coulomb interaction U:

$$H = -t \sum_{(i,j),\sigma} \left(c^{\dagger}_{i,\sigma} c_{j,\sigma} + c^{\dagger}_{j,\sigma} c_{i,\sigma} \right) + U \sum_{i} n_{i\uparrow} n_{i\downarrow} \tag{1.1}$$

In this equation, t is the transfer integral that represents the kinetic energy of electrons hopping between atoms, (i, j) stands for the summation over all nearest-neighbour lattice sites, $c^{\dagger}_{i,\sigma}$ and $c_{i,\sigma}$ are the creation and annihilation operators for electrons of spin σ at site i, and $n_{i,\sigma} = c^{\dagger}_{i,\sigma} c_{i,\sigma}$ gives the number operator that represents the density of electrons at site i with spin σ.

In the non-interacting limit, the first term leads to a metallic behaviour when the system is half filled, and is simply the Hamiltonian in regular band theory. On the other hand, in the strongly interacting limit, the second term favours charge localization and hence an insulating behaviour. For the case of VO_2, the opening of a band-gap can be regarded then as a competition between the U Coulomb interactions of vanadium 3d electrons and the transfer integral t of the 3d electrons tunnelling to neighbouring atoms.

Zylbersztejn and Mott attributed the electronic correlations that lead to the opening of the band-gap in VO_2 to the strong electron-electron interactions occurring in the $d_{\parallel}$ band. In the metallic state, though, these Coulomb interactions are well screened by the π^* states. When lowering the temperature of the system, the charge density is reduced and so is the screening, until the Coulomb potential gets high enough to support bound states, localizing electrons away from the conduction band causing the splitting of the $d_{\parallel}$ band, as already seen in in Fig. 1.

The band-gap opened in such a system was first formulated by Mott in the form:

$$E_{\text{gap}} = U - \frac{1}{2}\left(B_1 + B_2\right), \tag{1.2}$$

where U is the Hubbard intra-atomic correlation energy (Coulomb repulsion), and B_1 and B_2 are the bandwidths of the upper (empty) and lower (occupied) Hubbard bands. In this scenario, the M_1 phase transforms to the R phase only when the free electron density reaches a certain threshold sufficient to screen the strong Coulomb interactions.

The inclusion of the U term in DFT calculations led to a different conception of the phase transition, in which the electronic and structural transitions are no longer concomitant, with only a causal relation between them. This decoupling results in the existence of an intermediate state between the IMT and the structural transition that presents a monoclinic lattice exhibiting metallic properties. The electronic band structure at each phase for such a material is illustrated in Fig. 1.4. The intermediate monoclinic metallic phase, depicted in

purple, consists of a split $d_{||}$ band as in the M_1 phase, together with π^* states overlapping with the Fermi level, as in the R phase.

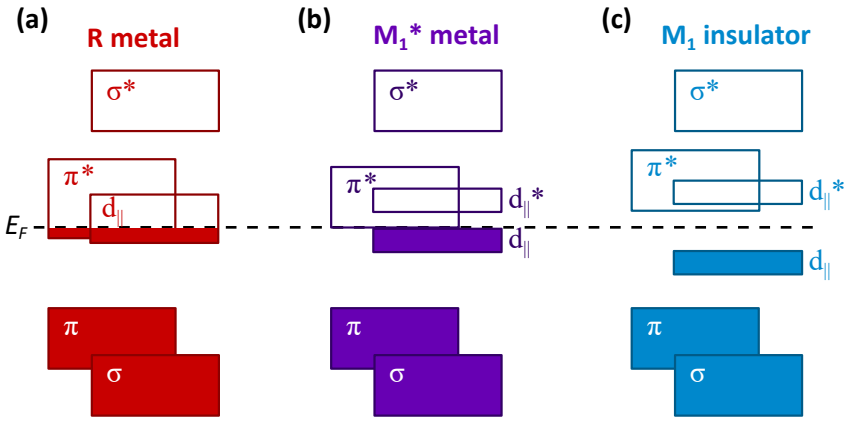

Fig. 1.4: Electronic band structure in a Mott phase transition. **(a)** In the metallic phase with the rutile structure, both the π^* and $d_{||}$ states overlap with the Fermi level. **(b)** In the intermediate phase, the $d_{||}$ band is split due to a reduction of screening and the structure changes into monoclinic. However, the metallic behaviour remains as the π^* states barely shift. **(c)** In the insulating monoclinic phase, Coulomb interactions lead to an increase separation of the π^* bonding and antibonding states, and the band-gap is further enlarged.

Such DFT+U method has been applied by several theoretical studies to describe the physics leading to the phase transition in VO_2 [18, 19]. However, despite yielding the right opening of the insulating band-gap in the monoclinic phase, the description of the system has not been perfect, as it failed to predict the magnetic ground state of VO_2 [20]. Fortunately, theoretical models and calculation methods have evolved in the last years and led to more consistent results. It has been demonstrated that band-theory based on DFT calculations is capable of describing the insulator-metal transition in VO_2 and all the involved phases, provided that the appropriate hybrid functionals are used [21], without the need of introducing any other interaction parameters.

The obvious contradictions between the theoretical models suggested by Goodenough and Mott have been translated into the experimental domain as well. Several experiments have reported conflicting results on VO_2, some supporting the electronic correlations scenario, while others point towards electron-phonon interactions as the driving mechanism. In order to reveal the true role of electronic correlations in the phase transition, these studies have been focused on two key aspects. Firstly, the observation of the intermediate state predicted by Mott with a monoclinic structure and metallic properties would

provide unambiguous evidence for the electronic nature of the phase transition, as its existence would mean that if electron-electron interactions could be screened, the M_1 phase would be metallic. Secondly, studying the phase transition in the time domain would reveal the true nature of the process, given that electrons have been traditionally considered to act on much faster time scales (typically of a few femtoseconds) than phonons (of hundreds of femtoseconds – picoseconds) [22].

However, one of the main reasons for the current discrepancies between different experiments is that the interpretation of results have been generally hindered by the phenomenon of phase separation, common to many correlated materials and directly related to the strain and type of sample, and the existence of more than one insulating phase in VO_2. Therefore, before addressing the methods for distinguishing between an electron- or phonon-driven transition, the physics of VO_2 should be discussed beyond the M_1-R transition.

1.1.3 The phase diagram of VO_2

In VO_2, as in many correlated materials, the specific characteristics of the phase transition, such as the transition temperature and sharpness, are strongly dependent on the strain within the sample measured. In fact, by measuring the temperature-dependent hysteresis curves of VO_2 across the phase transition, useful information about the strain within the sample, and thereby its quality, can be obtained, directly related to the transition temperature and hysteresis width.

Several studies of the correlation between crystal structure and hysteresis curves have been performed, arriving to the conclusions that large transition widths in films can be attributed to local differences related to the presence of grains with different sizes, defects densities and strain interactions [7, 23, 24]. Samples grown by diverse methods present different hysteresis curves due to their particular insulator-metal domain structure. Figure 1.5 displays a schematic comparison of the resistivity hysteresis curves as a function of temperature followed by a high-quality single crystal, where single-domain behaviour is expected, and a thin film, in which multiple domains coexist during the transition. Experimentally, it has been observed that, while transitions in single crystals can be very sharp and occur within 0.01 K [7], even the highest-quality thin films can show broadened transition widths that span several degrees in temperature [25], which result from different regions of the sample switching at different temperatures. This variation indicates the presence of defects that locally modify the transition temperature.

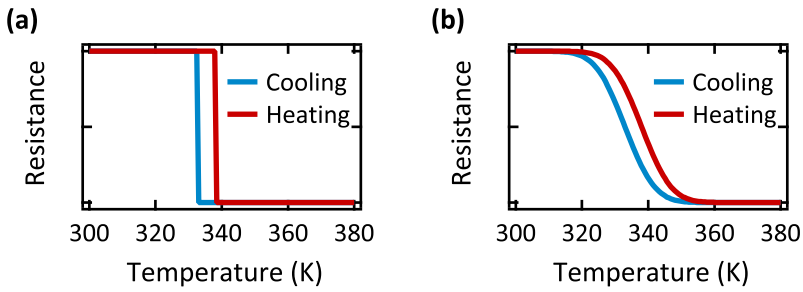

Fig. 1.5: Schematic hysteresis curves. Resistance as a function of temperature of a single crystal **(a)** and a thin film **(b)**

Measurements on VO_2 were originally conducted on single crystals, which provide a more pure response on the behaviour of the material. However, the lattice distortion and the derived volume change that occur across the phase transition are enough for bulk single crystals to break when subjected to thermal cycling, i.e., repeated heating and cooling cycles across T_C [26]. Therefore, the majority of the experiments have been conducted on polycrystalline thin films of VO_2, which can withstand the strain arising from the lattice distortions. More recently, a type of sample has been developed that unites both desired qualities, namely, high quality together with an ability to accommodate strain: single-crystals nanobeams [27–36]. These free-standing nanomaterials can be subjected to tunable uniaxial strain and, due to their lack of extended structural defects, can resist much higher strain ($> 3\,\%$) than their bulk counterpart ($< 0.2\,\%$) without fracturing [35, 36]. These properties enable the investigation of strained states otherwise inaccessible and, thereby, the stress-temperature phase diagram of VO_2, which involves other phases than the already mentioned M_1 and R.

Indeed, the application of Cr-doping [37] or uniaxial strain along the rutile c-axis [38] on VO_2 samples led to the discovery already in the early days, that VO_2 can exist in two other insulating states, besides the monoclinic M_1 [37, 38]: a second monoclinic structure, M_2, and a triclinic structure, T. As depicted in Fig. 1.6(a), while in the M_1 phase, the pairing and zigzag displacements are observed in each chain of V atoms, in the M_2 phase there are two different types of chains, displaying either dimerization or the zigzag pattern, but not both. On the other hand, T is an intermediate structure, in which those chains that are dimerized in the M_2 phase start to tilt, and those tilted start to pair, until both distortions are the same as in the M_1 phase. The boundaries of each state in the phase diagram of VO_2 were roughly determined in 2010 via the study of bent nanobeams [36].

It was not until recently, though, that the solid-state triple point compris-

ing the M_1, M_2 and R phases was exactly located, and the phase diagram of VO_2 mapped out with unprecedented precision through the study of individual single-crystal nanobeams [39]. Before that, the general consideration was that a sample with no strain at all presented a direct transition from M_1 to R at T_c. The mentioned work found this assignment not true, and revealed that the triple point is precisely at the zero-stress point, which matches thus T_c (see Fig. 1.6(b)). This fact is consistent with early thoughts regarding the free energies of M_1 and M_2, believed to lie very close around T_c, being therefore the reason for the difficulty in the stabilization of pure M_2 [38].

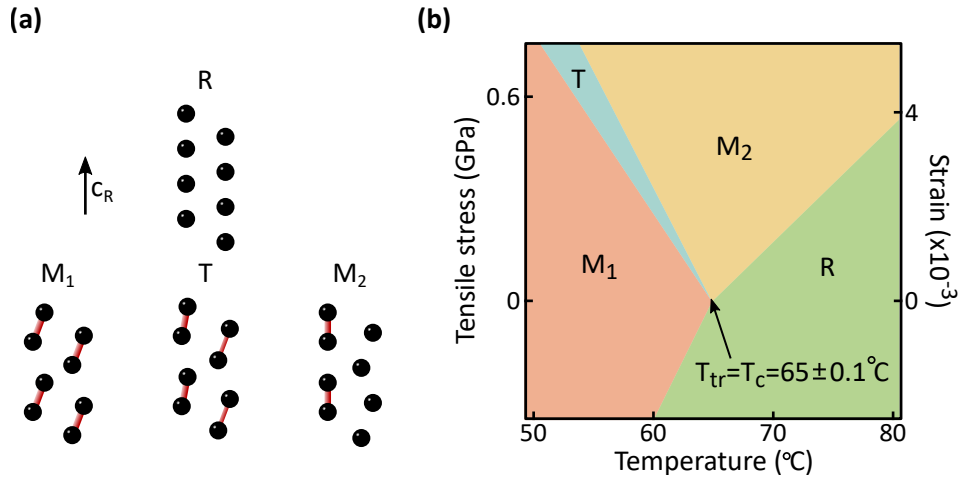

Fig. 1.6: Phase diagram of VO_2. **(a)** Arrangement of vanadium atoms chains along the rutile *c*-axis in the different phases of VO_2. The three insulating phases present different dimerization degrees and/or tilting. **(b)** The schematic stress-temperature phase diagram indicates the boundaries of each phase and the location of the solid-state triple point, which matches that of the transition temperature at zero stress and leads to phase competition near the IMT. The system can take different paths when transforming from M_1 to R, involving the other two insulating phases: M_2 and T.

According to this phase diagram, the insulator-metal transition in VO_2 can be complicated by high strain values or high doping, which can induce the presence of the M_2 phase [13, 30, 31, 38, 40]. Also, given the location of the triple point, VO_2 exhibits an extreme sensitivity to external factors. The phase transition is thus harder to interpret, as the transition pathway can easily involve other phases beyond the generally considered M_1 and R phases.

Nonetheless, as mentioned before, the studies on VO_2 intended for revealing the true nature of the phase transition have focused on the search of a monoclinic metallic phase and the dynamics of the transformation, often

neglecting, though, the issue of phase separation and the existence of other phases. This is discussed in the following sections.

1.2 Evidence for a monoclinic metallic phase

The simultaneous measurement of the electronic and structural properties of VO_2 during the insulator-metal phase transition is no simple task, which complicates the potential observation of a metal-like monoclinic phase. Furthermore, the transient nature of such a phase makes the measurement of its electronic states more of a challenge. Several experiments employing various techniques have attempted to achieve this over the years. In 2007, Arcangeletti *et al.* claimed decoupled insulator-metal and M_1-R transitions at high pressure by measuring the mid infrared (MIR) reflectivity and Raman spectra as a function of applied pressure [41]. The former probes the optical band-gap, while the latter provides information about the lattice. Applying pressure to the sample compresses the lattice, increasing orbital overlap and electronic bandwidth. This way, they aimed to monitor independently the electronic and structural transitions, which were found to occur at different pressures. However, although the conductivity increased, it was not shown whether the system switched into a truly metallic phase.

Later, in 2010, Yao *et al.* attempted as well to perform such a simultaneous measurement, in which they tracked the electrical resistivity and the twisting angle of the vanadium dimers by temperature-dependent *in situ* X-ray absorption fine structure (XAFS), in combination with DFT calculations [42]. They observed stabilization of the metallic state caused by the melting of V-V dimers before the rutile symmetry was adopted, that is, before the twisting angle was completely vanished. In this range, an intermediate monoclinic-like structure with metallic character was detected. With further development of *in situ* observation techniques, a breakthrough regarding this subject in 2014, when Laverock *et al.* reported a direct observation of decoupled structural and electronic components of the insulator-metal transition in VO_2 [43]. By comparing electron microscopy images of VO_2 thin films, which probed their crystallographic structure, with photoemission spectroscopy to explore the electronic properties of each phase at selected temperatures across the phase transition, they discovered that within 60–80 °C the fraction of metallic phase predicted by photoemission spectroscopy was much larger than the total amount of metallic domains observed in the microscopy images. Therefore, they concluded that within this temperature range the sample is formed by a mixture of rutile metallic and monoclinic metallic phases, with the latter ascribed to a possible weakening of the bonds that constitute the V-V dimers, as predicted by Zylbersztejn and Mott [4].

The phenomenon of electronic and structural transitions occurring at dif-

ferent temperatures was also observed in 2016 by Gray *et al.* via X-ray absorption spectroscopy on thin films of VO_2. In this experiment, by assigning different XAS features to the electronic correlations and to the structural distortion, and measuring their temperature dependence, they suggested that correlations within the V-V dimers weaken some temperature degrees before the crystallographic transition takes place. In this three-step scenario, similar to [43], several degrees below the IMT, in the monoclinic-insulating phase, the two $3d^1$ electrons of the dimerized V atoms form a strongly correlated singlet state, which start to soften with increasing temperature until they become weak enough for the band-gap to collapse. In the final step, the crystal structure gets distorted as a consequence.

In conclusion, the experiments that report evidence on a monoclinic-like metallic phase suggest that vanadium dimers play an important role in the phase transition, in which the softening and loss of the strong correlations within them lead to the formation of the intermediate transient correlated phase. The constitution of strongly correlated vanadium singlet pairs resulting from the strong dimerization is supported as well by electronic-structure calculations based on cluster dynamical mean-field theory (CDMFT) [44].

However, the above-listed results share two common aspects that are worth mentioning. Firstly, the assumption of spatially homogeneous insulator-metal phase transitions in the employed VO_2 thin films. Despite claiming high-quality samples, thin films are not comparable to high-quality single-domain crystals, which is evidenced by the transition sharpness and hysteresis curves they display. Moreover, many of the samples employed are epitaxial thin films, grown on substrates such as Al_2O_3, which present an aggravating aspect regarding biaxial strain that results from the lattice mismatch between both films. Therefore, the premise based on homogeneous probing may not be fully correct and the system response might be more complex to interpret than a simple M_1-to-R transition. Secondly, the evidence provided for the existence of an intermediate monoclinic-metallic phase is rather indirect, in the sense that at least two separated experiments employing different techniques need to be performed in order to measure the electronic and structural aspects of the phase transition. Given the extreme sensitivity of these thin films to external parameters, it would be no surprise that different experimental conditions lead to different results.

Moreover, despite the volume fraction across the phase transition being studied in [43], this was not directly measured. Proper direct information on the volume fraction of the constituents of the phase transition in VO_2 is required in order to understand the true evolution of it. To date, no technique

has been able to directly probe the electronic and structural components simultaneously with sufficient spatial resolution to ensure homogeneous probing. As a consequence, the question regarding the existence of a monoclinic metallic phase and, if so, the position of it within the phase diagram of VO_2 (Fig. 1.6), remains unanswered.

The large controversy with respect to the so-called Mott vs Peierls competition is due to a large extent to a poor comprehension of the near-threshold behaviour of VO_2, hindered by domain formation and phase separation preventing the direct measurement of the intrinsic electronic and structural properties of the material. Therefore, techniques able to probe with nanoscale spatial resolution are imperative for a full understanding of the insulator-metal phase transition in VO_2.

1.3 Phase-transition dynamics

The reported experiments so far rely on static techniques to study the phase transition in VO_2, such as Raman spectroscopy [40, 41], electron diffraction [6, 8], and photoemission spectroscopy [10, 43]. While these are suitable for capturing the properties of the monoclinic-insulating and rutile-metallic phases of VO_2, they lack the ability to unambiguously determine cause-effect relationships in a material in which more than one degree of freedom are changing simultaneously, such as electron and lattice contributions. Therefore, in order to access the characteristic short time scales of these competing interactions and disentangle their responses in real time, ultrafast time-resolved studies are an ideal approach.

Such measurements make use of the so-called *pump-probe* technique, in which the material is excited by a strong laser pulse generating a non-equilibrium state that is subsequently tracked by a weaker pulse of either laser light, X-rays or electrons. The time delay between both pulses can be controlled in a way that enables the monitoring in real time of the redistribution of energy among different degrees of freedom of the system. In fact, the electronic and crystallographic phase transition in VO_2 can be induced and probed in such a manner, paving the way for revealing the nature of its driving mechanism.

The main focus of ultrafast experiments has been the determination of the time scales necessary for the phase transformation completion after photoexcitation. These values have shown a tendency to decrease over the years as advances in the techniques employed have provided improved temporal resolutions. The first time-resolved experiments on VO_2, conducted by Cavalleri *et al.* in 2001, that probed the electronic and structural dynamics by means of femtosecond visible-light and X-ray pulses, reported a subpicosecond structural transition in VO_2 when excited by sufficiently high laser fluences [45]. A later experiment with superior temporal resolution measured the transient reflectivity and transmission, which showed the existence of a limiting time scale for the completion of the phase transformation [46]. No faster transition than 80 fs was observed, even when exciting with pump pulses with a time duration as short as 15 fs. This time delay between photoexcitation and the phase transition occurrence was attributed to a *structural bottleneck* related to an optical phonon period that connects the initial and final structures. This result pointed towards a Peierls-driven phase transition in VO_2.

These initial experiments inspired many subsequent reports of the photo-induced phase transition in VO_2, and further efforts have been made for disen-

tangling the electronic and structural contributions. A large amount of these studies have claimed a temporal decoupling of the electronic and crystallographic transitions. In 2006, Kim *et al.* conducted the first simultaneous analysis of both transitions by means of an optical pump-probe experiment, which concluded in the existence of a transient monoclinic and correlated metal [19]. The observation of a time delay between electron rearrangement and the structural transition has also been reported by measurements of the time-dependent optical and electrical properties [47–49], and by ultrafast electron diffraction (UED) experiments [50, 51].

The emergence of such a transient monoclinic metallic phase implies that the time scales necessary for closing the band-gap are shorter than those required for making changes in the lattice structure. This sequence has been generally attributed to the generation of holes at the top of the valence band by photo-excitation, as proposed by the static observations of the monoclinic metal [52, 53], which strongly enhances the screening of the Coulomb interactions through free carriers, leading to the collapse of the band-gap. An instantaneous band-gap collapse after photo-excitation was indeed suggested from measurements by Wegkamp *et al.* by means of time-resolved photoemission spectroscopy [54].

As a consequence of the ultrafast onset of the phase transition, which rules out the presence of a structural bottleneck, together with the evolution of the electronic and structural transformations over multiple time scales, time-resolved ultrafast measurements have in general tended for a Mott-physics-mediated phase transition in VO_2. The general assumption has been that the temporal dynamics of the phase transition provides information about the nature of the driving mechanism and hence enables to distinguish between a transformation dictated by Mott physics or by a Peierls distortion. Within this picture, if driven by electronic correlations, the transition should occur in a prompt manner, as photoexcitation originates suddenly a charge redistribution and a consequent change in screening. On the other hand, if driven by electron-phonon interactions, the lattice needs to change before the band-gap can be closed, so that the time scales for the transition are set by atomic motion, resulting in a slower transformation. However, in a non-equilibrium situation, the lattice potential, which determines the phonon spectrum of the solid, may respond in shorter time scales than the atomic motion towards their new equilibrium positions. In fact, the lattice response out of equilibrium has not been as extensively studied as electron dynamics, and therefore a full comprehension of phonon dynamics across the phase transition is still missing.

Attempts on studying the lattice evolution across the phase transition in

VO_2 have been made by means of ultrafast elastic X-ray [45, 55] and electron-diffraction [50, 51, 56] experiments. These techniques make use of the Bragg peaks recorded to obtain information about the ionic positions, the disturbance of which after photo-excitation is translated into changes in the corresponding Bragg peaks. Electron-diffraction experiments performed this way by Baum *et al.* in 2007 [56], by Tao *et al.* [50] in 2012, and Morrison *et al.* [51] in 2014, in combination with optical techniques, led to the conclusions that the structural and electronic transitions are temporally decoupled and a photo-induced metal-like phase of monoclinic VO_2 exists in between them, just as the ultrafast optical measurements previously mentioned.

A problem emerges, though, with the fact that Bragg peaks probe the equilibrium position of the ions, but not the dynamics of the lattice potential, which sets the driving force for the atomic motion and may not be concomitant in a non-equilibrium situation. As an approach to overcome this limitation, Wall *et al.* suggested that changes in the lattice symmetry can be measured through the evolution of the phonon spectrum across the phase transition by the optical transient reflectivity of VO_2, with sub-50-fs time resolution [57]. This way, they observed a dramatic phonon collapse occurring immediately after photoexcitation before ionic rearrangement could take place, suggesting that energy transfer from electrons to the lattice proceeds faster than usually expected. The "fast"-electrons *vs* "slow"-phonons scenario is then strongly challenged, with a lattice-mediated phase transition now compatible with the reported ultrafast photo-induced phase transition. An extensive analysis of the role of lattice vibrations during the out-of-equilibrium insulator-metal phase transition in VO_2 is hence necessary in order to clarify the observed discrepancies and elucidate the true driving mechanism. Furthermore, whether the ultrafast phase transition is fundamentally different from the equilibrium thermal behaviour is a question that remains still open.

2 | Phase separation

This chapter introduces one of the major challenges when studying the insulator-metal phase transition in VO_2: phase coexistence on the nanoscale. This property, overlooked in VO_2 and correlated materials in general, makes it necessary to employ techniques with the ability to spatially resolve the response of the material at nanometer length scales. In Section 2.1, an introduction to the phase-coexistence phenomenon is presented, followed in Section 2.2 by a description of the employed technique in this thesis to approach the problem: resonant soft X-ray holographic imaging. The performed experiment is described in Section 2.3 while the results achieved on imaging the insulator-metal phase transition in VO_2 are presented in 2.4. The chapter ends with conclusions in Section 2.5.

2.1 Introduction

Correlated materials are known for their sensitivity to external parameters, such as strain, magnetic fields and chemical doping. Small variations in these parameters can drive the system into different phases with widely diverse, and often contradictory, properties, such as magnetism, superconductivity, or insulating-metallic states. The domains of such phases can coexist, leading to the so-called phase separation [58]. In manganites, for instance, phase coexistence on the nanoscale is believed to be key for understanding the colossal magneto-resistance effect [59], while superconductivity and charge-density-wave order coexist in the cuprates [60–62] and pnictides [63, 64]. As a result, inhomogeneity may play an important role in a wide range of correlated materials.

As explained in Section 1.1.3, recent research on this topic has in fact demonstrated that VO_2 sits close to a solid-state triple point close to room temperature [39]. As a result, the material exhibits an extreme sensitivity to external factors, so that small changes in parameters such as temperature or stress can drive the system into different phases beyond the generally considered M_1 and R phases. Due to the strong first-order nature of the phase transition in VO_2, these phases can coexist in spatially separated regions reaching sizes of several micrometers. Such a phase competition is strongly dependent on the sample type [65]. Thin films are much more defective than single crystals, which, together with strain inhomogeneity arising from the substrate, make the former more sensitive to external parameters, modifying the transformation kinetics and causing the transition from M_1 to R to be more complex to interpret.

The small length-scales of this phase separation and the lack of contrast mechanisms make it extremely challenging to measure real-space images of the coexisting phases with high spatial resolution. Yet, these images are vital for understanding how this phenomenon, and the consequent domain boundaries, dictate the material properties. Recent experiments have employed various imaging techniques to visualize the formation of domains of the different phases during the insulator-metal transition in VO_2. Infrared near-field spectroscopy [65] and nanoscale X-ray-diffraction measurements [66] have shown how, close to the transition temperature, phase separation occurs and local defects and strain can cause different regions of the sample to switch at different temperatures. On the other hand, optical microscopy on single-crystalline nanobeams have demonstrated the effect of strain in the formation of alternating nanoscale insulator-metal domains in a striped pattern [27, 32].

As discussed in Section 1.2, several investigations have reported evidence for decoupled electronic and structural transitions, in which an additional phase is observed with a monoclinic structure but metallic properties. But so far, the employed methods have provided indirect evidence of such transient phase, as the probes average over large sample areas or require multiple techniques to probe the different phases. Hence, no real-space image of the monoclinic metallic phase has yet been measured.

In order to assess the existence of each phase and the role they play during the phase transition, a method that can image with nanometer spatial resolution and is sensitive to both electronic and structural degrees of freedom is necessary. Resonant soft X-ray holography is an ideal tool to overcome this challenge, as it exploits the power of element and polarization specificity of soft X-ray absorption spectroscopy (XAS) as the source for imaging contrast, and it has also the potential to be extended to the time-domain, enabling the capture of the spatial growth of transient states in the near future.

2.2 Lensless X-ray spectro-holography

X-ray holography belongs to a group of techniques named as *Coherent Diffraction Imaging* (CDI) that have drawn great attention in the past decade as a new and much-simpler form of aberration-free microscopy with a resolution only limited, in principle, by the X-rays wavelength. Conventional microscopes rely on the use of imaging optics, such as lenses, to form the magnified image of a certain object. However, the difficulty in fabricating high-resolution lenses for X-rays in the early days stimulated the interest in a lensless imaging approach, where the optics were replaced by numerical computations. In the basic scheme, a detector records the distribution of the diffracted X-rays from the object of interest obtained by illuminating it with coherent X-rays, and this pattern is afterwards digitally reconstructed to obtain a real-space image of the object.

Although nowadays high-resolution X-ray optics, like zone-plates, are much more available, their experimental constraints, such as low transmission and the wavelength-dependent alignment, represent a major drawback with respect to the simpler CDI setup. Specifically, full field transmission X-ray microscopy (TXM) is capable of forming a 2D image in a matter of seconds. However, the need of using two zone-plates results in the requirement of a great interferometric stability, and also, given the low efficiency of the objective optics, the sample located before it receives a high dose of X-rays, making radiation damage a big problem. These issues are overcome by scanning X-ray transmission microscopy (STXM), which employs only one objective zone-plate placed before the sample [67, 68]. The disadvantage, though, comes with the longer times required for the large field scanning, which makes this approach unsuitable for time-resolved measurements. Lensless CDI, on the other hand, is free from these experimental disadvantages, and provides a full-field imaging approach that can be implemented in ultrafast measurements.

2.2.1 Coherent imaging fundamentals

A typical experimental setup for lensless coherent diffraction imaging is formed by three basic elements: coherent X-rays, sample and detector, as schematically illustrated in Fig. 2.1. Note that here diffraction is not related to Bragg scattering, but just to the propagation of a wave when it encounters an object with a spatial dependent refractive index. In this transmission geometry, the X-rays impinge upon the sample and the diffracted waves propagate a distance z, where they reach the detector. According to the laws of electromagnetic

waves propagation, the far-field diffraction distribution formed at the detector plane is given by the Fraunhofer approximation in the form:

$$\Psi(X,Y) = \frac{e^{ikz}e^{i\frac{k}{2z}\left(X^2+Y^2\right)}}{i\lambda z}\iint_{-\infty}^{\infty}\psi(x,y)e^{-i\frac{2\pi}{\lambda z}(xX+yY)}\,dx\,dy, \tag{2.1}$$

where $\psi(x,y)$ is the exit wave at the sample plane and the variables are defined in Fig. 2.1. By comparing this expression with the two-dimensional Fourier transform in space and spatial frequency, i.e.,

$$\mathcal{F}\left[g(x,y)\right] = G(u,v) = \iint_{-\infty}^{\infty} g(x,y)e^{-i2\pi(ux+vy)}\,dx\,dy, \tag{2.2}$$

where u and v are the frequencies in reciprocal space [69], it is evidenced how, aside from multiplicative factors, the diffracted wave recorded at the detector is nothing but the Fourier transform of $\psi(x,y)$ evaluated at the spatial frequencies $u = X/\lambda z$ and $v = Y/\lambda z$.

However, detectors are only able to measure intensity $\left(I = |\Psi(X,Y)|^2\right)$, with the phase information being inevitable lost. This is known as the *phase problem*, as a real-space image of the object cannot be obtained with the wave amplitude information alone. The problem of CDI is then reduced to reconstructing $\psi(x,y)$ from $I = |\Psi(X,Y)|^2$.

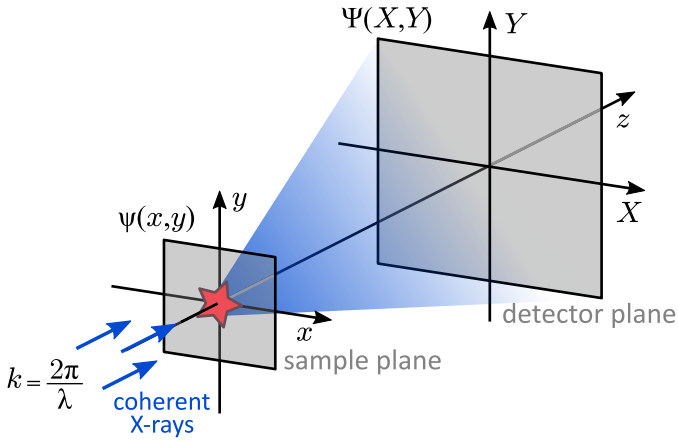

Fig. 2.1: Coherent diffraction imaging setup. The X-rays beam of wavelength λ impinge on the sample, and the diffracted light is recorded by a detector in the far field.

Generally, under this imaging approach, the maximum pixel resolution and field of view achievable are set by the distance between sample and detector in the following way:

$$\delta = \frac{\lambda D}{N\omega}, \tag{2.3}$$

where δ is the size of the resolution element, or pixel size, λ is the chosen X-rays wavelength, D the distance between sample and camera, and N and ω are the detector parameters, namely, the number N of pixels of size ω. The field of view is given then by:

$$N\delta = \frac{\lambda D}{\omega}. \tag{2.4}$$

As a result, the pixel resolution and field of view are competing quantities. However, in reality, the final object size and resolution are decided by the exact experimental conditions, as will be discussed later for the particular imaging method adopted here.

With the aim of obtaining the reconstructed real-space image $\psi(x, y)$, phase-retrieval numerical algorithms were greatly developed [70, 71], which, together with the increased coherent photon flux delivered by 3rd-generation synchrotron sources [72, 73], made it possible to achieve the first experimental demonstration of such a technique in a non-crystalline object in 1999 by Miao *et al.* [74]. Yet, iterative phase-retrieval algorithms require an *a priori* knowledge of the object of interest that defines strong real-space constraints for the calculations to converge to a solution, which increases in complexity when imaging non-binary objects.

X-ray holography fundamentals

In this thesis, a different approach is used to solve the phase problem, based on recording the phase information of the wave front by encoding it in intensity modulations, rather than retrieving it by numerical algorithms. This idea, built upon Young's double-slit interferometer, was first proposed in 1948 by Gabor *et al.* [75], who suggested that by introducing a reference source aside from the object, the interference pattern created by both waves would have the phase information embedded in the form of fringes. This pattern is the so-called *hologram*, which can deliver the real-space image of the object by

Fourier inversion. A thorough historical review of X-ray holography can be found in [76].

In lensless holography, an additional source is located at the sample plane that generates the reference wave intended to interfere with the wave scattered from the object. Following the notation used in Eq. 2.1, the wave transmitted by the ensemble of object and reference can be written as the superposition of the object and reference waves:

$$\psi(x,y) = o(x,y) + r(x,y), \tag{2.5}$$

where each of the waves is given by the product of the incoming wave ψ_0 with the transmittance functions, $t_r(x,y)$ and $t_o(x,y)$. Note that $o(x,y)$ and $t_o(x,y)$ are centred at $(0,0)$, while $r(x,y)$ and $t_r(x,y)$ are centred at $d = (d_x, d_y)$, all of them having a finite size at these areas. According to the Fraunhofer approximation, the propagated wave in the far field is then the Fourier transform of the transmitted wave:

$$\begin{aligned} \Psi(X,Y) &= \mathcal{F}\{\psi(x,y)\} = \mathcal{F}\{o(x,y)\} + \mathcal{F}\{r(x,y)\} \\ &= O(X,Y) + R(X,Y), \end{aligned} \tag{2.6}$$

with capital letters indicating Fourier transforms, and the recorded intensity:

$$\begin{aligned} I(X,Y) = |\Psi(X,Y)|^2 &= |O|^2 + |R|^2 \\ &= OO^* + RR^* + OR^* + RO^* \end{aligned} \tag{2.7}$$

This sum constitutes what is known as *Fourier transform hologram*, which gives the name to the imaging method, Fourier Transform Holography (FTH). Fourier inverting the term corresponding to the object independently is not possible, but it becomes necessary to calculate the inversion of the full hologram to get the real-space image of interest,

$$\begin{aligned} \mathcal{F}^{-1}\{I(X,Y)\} = \mathcal{F}^{-1}\left\{|O|^2\right\} &+ \mathcal{F}^{-1}\left\{|R|^2\right\} \\ &+ \mathcal{F}^{-1}\{OR^*\} + \mathcal{F}^{-1}\{RO^*\} \\ = o \star o + r \star r &+ o \star r + r \star o \end{aligned} \tag{2.8}$$

The first two terms are the autocorrelations of the object and reference apertures alone, and the last two are the cross-correlation terms derived from the interference of the waves coming from both apertures. Assuming the reference is a real function, the cross-correlation term $o \star r$ can be considered as a convolution, which results in a blurred image of $o(x, y)$. However, if the reference is a point source small enough to be described by a delta function, and considering the convolution with a two-dimensional Dirac distribution results as

$$f(x, y) * \delta(x - X, y - Y) = f(x - X, y - Y), \tag{2.9}$$

the reconstructed wave-field is then given by:

$$\begin{aligned} \mathcal{F}^{-1}\{I(X, Y)\} = & \, o \star o + \delta(x, y) \\ & + o(x - d_x, y - d_y) \\ & + o^*(-x - d_x, -y - d_y), \end{aligned} \tag{2.10}$$

where $d = (d_x, d_y)$ is the distance between object aperture and reference point source. Note that the third term is in fact the real-space image of the object displaced a distance d from the center of the reconstructed hologram, and the fourth term represents the inverted conjugate localized in a symmetric opposite position. On the other hand, the first two terms, resulting from the autocorrelations of the two apertures, appear centred at the origin of coordinates and require extra methods for retrieving useful information out of them.

These equations result in certain constraints for the design of the object-reference ensemble. It should be noticed that the size of the $o \star o$ term is twice that of the real sample, therefore, the distance between the apertures should be at least twice the sample size to avoid overlap in the reconstruction. Yet, this distance is ultimately limited by the X-rays transverse coherence length.

In Fourier transform holography, the spatial resolution is not limited by the pixel size of the detector, as seen for CDI in Eq. 2.3. Instead, it is dictated by the spatial bandwidth of the hologram, that is, a higher resolution is achieved in the reconstruction when the hologram captures scattering with a higher momentum transfer. In reality, though, the reference source is not a perfect delta function, but its finite extent does blur the image and this stands as the final limitation of the spatial resolution achieved in the reconstruction. However, as tempting as it could be to have the smallest hole achievable, in

doing so, a higher spatial resolution is achieved at the expense of the image quality, as having less photons going through the reference hole results in a drop of interference recorded. An adequate size needs to be chosen so that a good compromise is achieved between spatial-resolution and signal-to-noise ratio (SNR).

The major technical drawback of Fourier transform holography was therefore to create a small enough reference source, so that the spatial resolution achieved would exceed that obtained with an optical microscope. McNulty *et al.* [77] were the first to accomplish this by using a Fresnel zone plate to create the bright point reference. The current lensless version of this technique was finally accomplished in experiments by Eisebitt *et al.* [78] and Schlotter *et al.* [79], who replaced the last lens with a gold mask that contained the micron-sized aperture that defined the object field of view and a sub-100-nm hole as the off-axis holographic reference. Furthermore, Eisebitt *et al.* demonstrated the use of resonantly tuned soft X-rays as the source for contrast in the Fourier transform hologram, while Schlotter *et al.* showed how the SNR can be greatly enhanced by having multiple reference holes in the holography mask without increasing the X-ray dose in the sample. The arrangement of the apertures had to fulfil the condition that, when translating the object around the mask, it did not overlap with more than one reference hole at a time [80]. These two features constitute the basics of the imaging measurement performed in this thesis.

2.2.2 Soft X-ray absorption spectroscopy

In this work, X-ray holography is employed to study the insulator-metal phase transition of VO_2. The combination of this imaging technique with soft X-rays that can be tuned to the vanadium and oxygen resonances stands as an ideal approach. In fact, soft X-ray absorption spectroscopy (XAS) not only provides element specificity, but is also sensitive to changes in the electronic structure near the Fermi level, as well as in the crystal field [25, 52, 53, 81–84], which are important for imaging phase transitions.

XAS is a local process in which the core electrons of the studied material are promoted to higher, unoccupied states [85]. These core electrons are strongly localized and have very specific binding energies. The absorption probability of an X-ray photon in such a process is described by the cross-section given by Fermi's Golden Rule that states the transition probability between a system in its initial state E_i and its final state E_f by absorbing an incident

photon with energy $h\nu$:

$$\sigma \sim \frac{2\pi}{\hbar} \left|\langle \psi_m \left| H \right| \psi_n \rangle\right|^2 \delta \left(E_f - E_i - h\nu\right), \tag{2.11}$$

where H is the interaction Hamiltonian, the first and dominant term of which describes the electric dipole transition of the form:

$$H_{\text{dip}} = \frac{e}{mc} \boldsymbol{p} \cdot \boldsymbol{E}, \tag{2.12}$$

with $\boldsymbol{p}$ the electron momentum and $\boldsymbol{E}$ the photon electric field. This inner product implies how, in XAS, the polarization of the X-rays provides orbital sensitivity.

In particular, in *soft* X-ray absorption, the photon is absorbed by a *shallow* core electron and excited to unoccupied levels above the Fermi level [81]. Within this energy range, comprised between 300 eV and 1000 eV, the K and L-edges of transition-metal oxides can be investigated. Specifically, in VO_2 the main edges are the oxygen K-edge (or 1s) and the vanadium L-edge (or 2p), which have been extensively studied both experimentally and theoretically [86]. Because dipole selection rules apply, electrons from an s-orbital can only go into unoccupied p-orbitals and electrons from p-orbitals can only get excited into either unoccupied s- or d-states. In VO_2, this means that the O K-edge probes $1s \rightarrow 2p$ transitions, and the V L-edge probes $2p \rightarrow 3d$ transitions. However, due to the strong interactions between core holes and valence electrons comparable to the band-width in the vanadium edge, the oxygen edge is easier to interpret, as the spectra resemble the oxygen p unoccupied density of states (DOS) in a first-order approximation [81]. Also, because of the strong covalent hybridization between the O 2p and V 3d orbitals resulting from the crystallographic structure of VO_2, XAS spectra at the oxygen K-edge also probe the 3d orbitals of the vanadium ions. Therefore, many studies on VO_2, as well as the work presented in this thesis, are focused on the oxygen K-edge.

VO_2 XAS spectra

Transmission spectra at the oxygen K-edge of a 75-nm-thick VO_2 sample are shown in Fig. 2.2. The XAS features (labelled in the graph) are well described by the crystal-field model, first proposed by Goodenough [3] and presented in Section 1.1.1, that results from the octahedral environment and the consequent hybridization of the O 2p orbitals with the V 3d ones. The first peak in the

spectrum at 529 eV corresponds to transitions into the π^* states, which shows a small red shift on entering the metallic phase as the band crosses the Fermi level and lower-energy transitions can be probed. The second main peak, found at 532 eV, is assigned to the σ^* states, which are higher in energy above the Fermi level due to a stronger p-d overlap. These states do not show any significant change across the insulator-metal transition. Between these two peaks there is a third one at 530.5 eV, only observable in the insulating phase, as it corresponds to the unoccupied $d_{\|}$ band that is split due to the structural distortion in the low-temperature phase [13, 83, 87]. The insulator-metal transition can then be tracked through changes in the π^* and $d_{\|}$ states. According to this theoretical

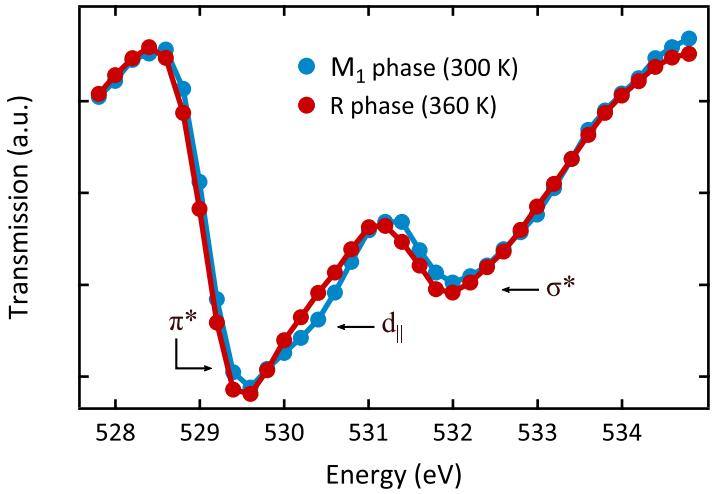

Fig. 2.2: X-ray transmission spectra of VO_2 at the O *K*-edge measured at low and high temperatures in the UE52-SGM beamline at BESSY II.

model, the $d_{\|}$ bands are derived from the $d_{x^2-y^2}$ orbitals parallel to the rutile *c*-axis that mediate the V-V bonds. Therefore, these states can only be probed when the polarization of the X-rays electric-field vector is parallel to the *c*-axis. As a result, this polarization-sensitive $d_{\|}$ peak allows the measurement of both the structural transformation as well as the orientation of the sample *c*-axis. Figure 2.3 shows the normalized spectra of the insulating phase measured with X-rays parallel and perpendicular to the rutile *c*-axis, where the $d_{\|}$ peak is no longer observable.

Noteworthy, there is an extra polarization-dependent feature noticeable around 529 eV, labelled as $d_{\|}^c$ in Fig. 2.3, which is not consistent with the π^* states, as they are isotropic according to the crystal-field model [3]. This small, polarization-dependent shift to lower energies, has been previously observed by other researchers and ascribed to effects resulting from electronic correla-

tions [25, 83], as predicted by CDMFT calculations [44], where electronic correlations were shown to provide an additional contribution from the $d_{\parallel}$ states to the bottom of the conduction band due to the formation of a correlated vanadium singlet-state in the M_1 phase. In the metallic phase, this dichroism is lost as the singlets are no longer present in the rutile crystallographic structure. As a result from this interpretation of the spectral features, while the

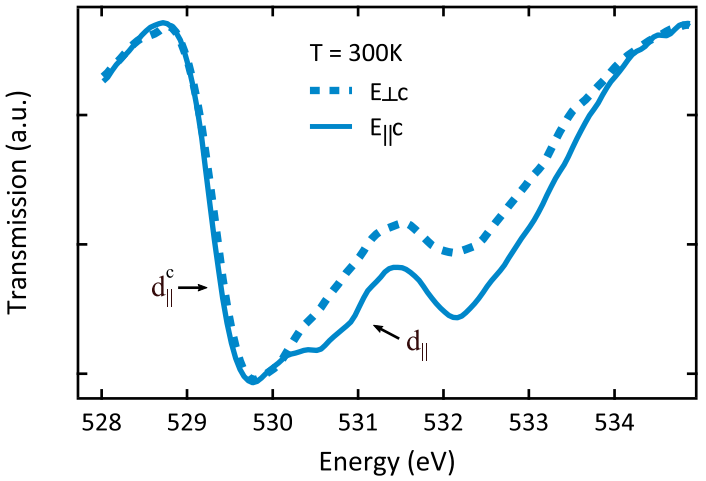

Fig. 2.3: Polarization-dependent X-ray transmission spectra of VO_2 at the O *K*-edge measured at room temperature in BOREAS beamline at the ALBA synchrotron light source.

insulator-metal transition can be tracked through changes in real-space images recorded at the π^* and $d_{\parallel}$ states, the electronic correlation variations can be measured via images at the $d_{\parallel}^{c}$ state.

2.3 Resonant holography on VO_2

2.3.1 Mask-sample fabrication

The correct fabrication of the mask-sample ensemble represents a key element for the proper functioning of this holography experiment and a few requirements must be fulfilled. Figure 2.4 illustrates the sample-mask design. VO_2 thin-film samples were fabricated by collaborators in Richard Haglund, Jr.'s research group at Vanderbilt University, to be afterwards processed into a suitable mask by collaborators from Stefan Eisebitt's research group at Technische Universität in Berlin.

The 75-nm-thick samples were deposited using Pulsed Laser Deposition (PLD) onto Si_3N_4 membranes on a silicon support frame featuring a 1.2-µm-thick Cr(5 nm)/Au(55 nm) multilayer on the reverse side. Unlike the Si_3N_4 membrane, the gold multilayer is opaque for the soft X-rays within the energy range used in this experiment and was used to define the holography mask. A focused ion beam (FIB) was used to mill a circular aperture of diameter 2 µm through the gold film, down to the Si_3N_4 membrane, which defines the object beam through the sample. Next to this aperture, at a center-to-center distance of 4–5 µm, three reference holes with exit diameters of 50–90 nm were drilled by a FIB through the entire mask-sample arrangement: gold multilayer, Si_3N_4 membrane, and VO_2 sample (see Fig. 2.4(b)). These aperture diameters (object and references) ratio is adequate for the relative sample and reference beam intensities.

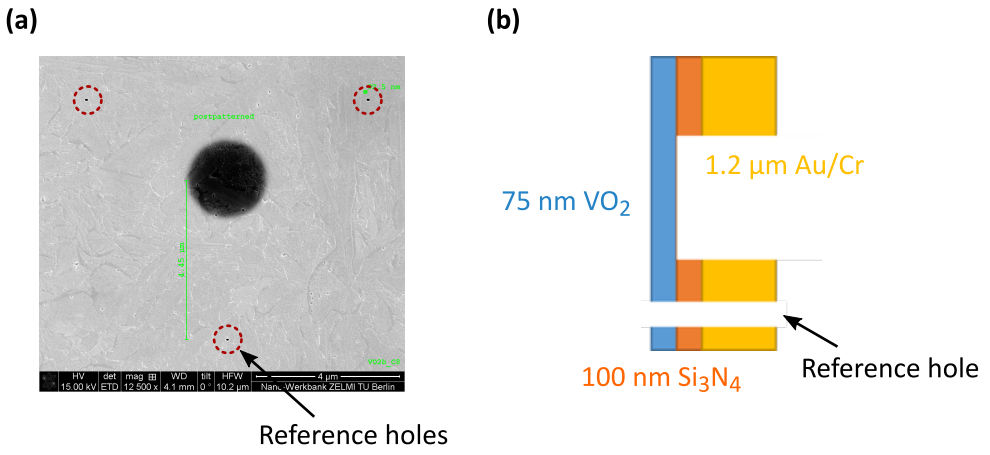

Fig. 2.4: Holography mask. **(a)** SEM of the mask-sample ensemble. The object aperture is in the center of the mask surrounded by the three reference holes. **(b)** Drawing from the side of the holography mask.

2.3.2 Samples characterization

Initial characterization of the samples was made by means of optical measurements. Knowing the phase-transition temperature of the sample is vital for imaging phase coexistence. The optical transmission was measured on a witness sample (without the gold mask used for holography) with white-light from a tungsten-halogen lamp (300–2600 nm) and detected with an amplified InGaAs PIN. The hysteresis curves obtained (see Fig. 2.5) are typical of high-quality VO_2 films.

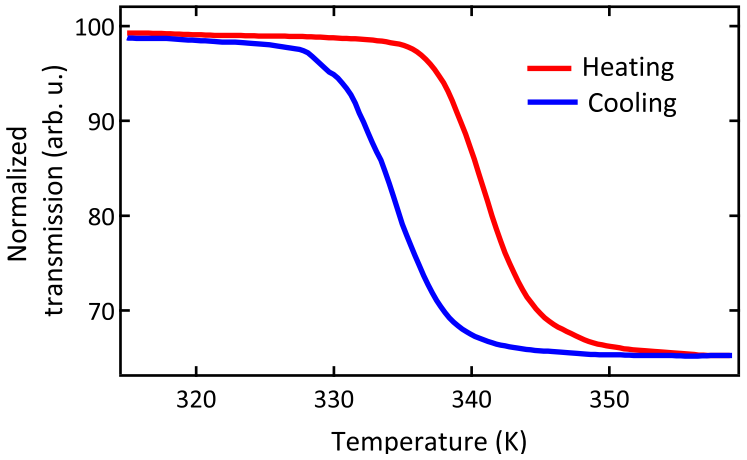

Fig. 2.5: Temperature-dependent optical transmission of the employed thin-film sample of VO_2. The hysteretic behaviour shows a width of ~ 6 K. Courtesy of Kent A. Hallman.

Additionally, given the phase-diagram of VO_2 (see Section 1.1) and the consequent possibility that the initial phase of the sample at room temperature is other than the generally considered M_1 phase, it is crucial to verify the state of the sample for the correct interpretation of the results obtained. This can be done by means of a Raman scattering measurement. The corresponding spectrum is shown in Fig. 2.6, which exhibits the characteristic peaks of the monoclinic M_1 phase [88].

Finally, before imaging the sample, X-ray absorption spectra were measured in order to find the relevant photon energies. XAS spectra across the vanadium and oxygen L- and K-edges, respectively, were measured via transmission of the thin film through the areas not covered by the gold mask, with the incident X-ray beam parallel to the sample normal. Full spectra at temperatures below and above the phase-transition temperature are shown in Fig. 2.7,

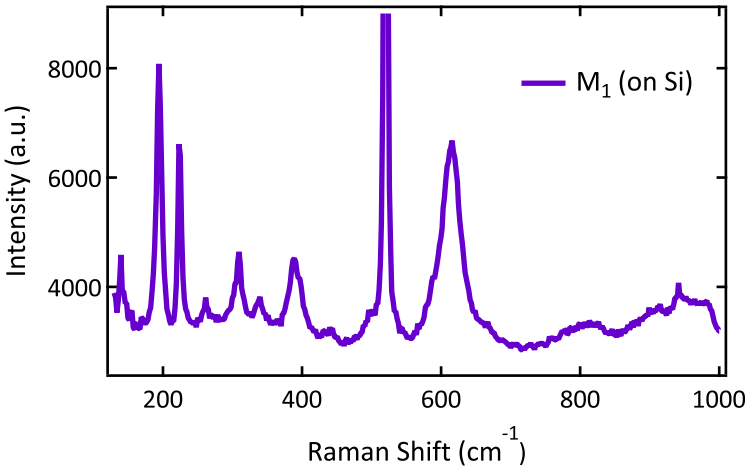

Fig. 2.6: Raman spectrum of the employed thin-film sample of VO_2 at room temperature. The observed peaks manifest the monoclinic M_1 structure. The two low-frequency modes at ~ 190 and $\sim 220\,\mathrm{cm}^{-1}$ are ascribed to V motion, while the peak at $\sim 620\,\mathrm{cm}^{-1}$ is believed to correspond to the oxygen ions connecting the V chains along the *c*-axis [88, 89]. The saturated peak at $\sim 500\,\mathrm{cm}^{-1}$ arises from the silicon of the substrate. Courtesy of Kent A. Hallman.

while the full discussion regarding the XAS features assignment can be found in Section 2.2.2. According to the differential spectrum, the maximum contrast between the insulator and metallic phases can be measured with a photon energy of 530.5 eV, the energy that probes the splitting of the $d_{\|}$ band.

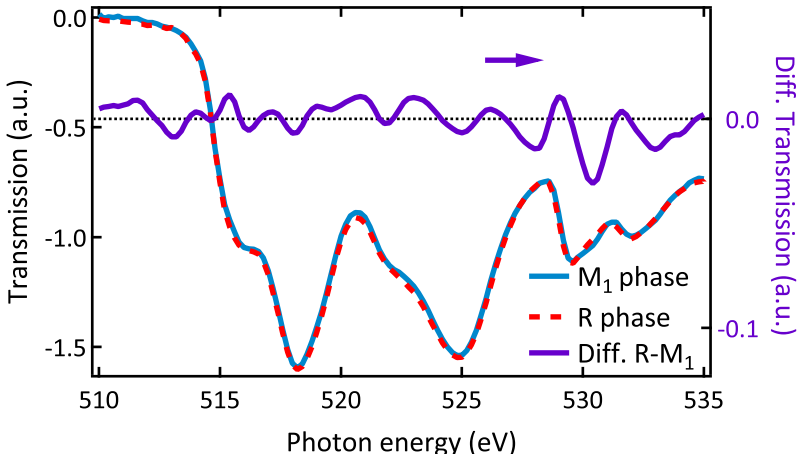

Fig. 2.7: VO_2 X-ray transmission spectra across the V *L*- and O *K*-edges. The differential spectrum (purple trace) shows the maximum contrast between the M_1 and R phases at 530.5 eV, the photon energy that probes the splitting of the $d_{\|}$ band.

2.3.3 Experimental details

The majority of the holography experiments on VO_2 were realized at the UE52-SGM undulator beamline of the BESSY II synchrotron radiation source of the Helmholtz-Zentrum Berlin using the ALICE X-ray scattering instrument [90]. This beamline provides a coherent soft X-rays beam with a flux of $\sim 10^{12}$ photons with a spectral resolution of 0.1 eV, focused down into a 60 µm spot size. Photon energy is variable by means of a monochromator. By placing the sample 40 cm downstream of the focus, the beam illuminating the holography mask is approximately 200 µm (vertically) x 1 mm (horizontally).

The ALICE instrument is equipped with a cryostat and resistive heaters that allow for the control of the sample temperature below and above T_c with a stability of 0.1 K. The detector, a charge-coupled device (CCD), is located approximately 40 cm away from the sample, resulting in an angular acceptance of 2°. This geometry corresponds to a maximum detectable in-plane momentum transfer of $\sim 90\,\mu m^{-1}$ and a maximum spatial resolution, i.e., diffraction-limited, of 35 nm.

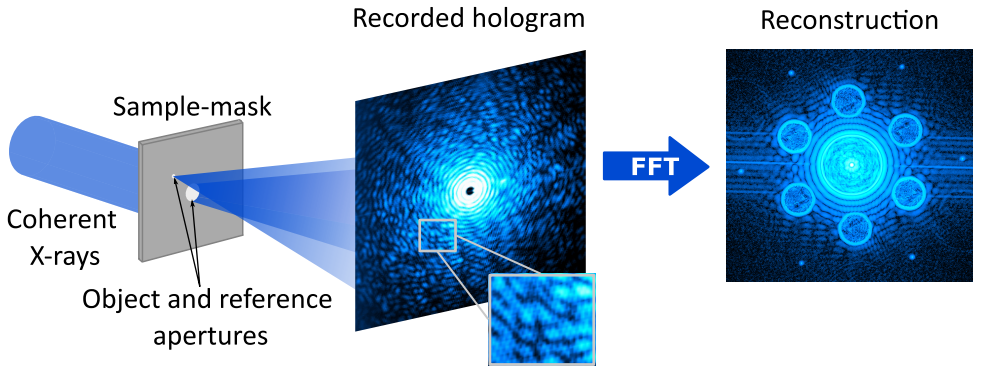

Fig. 2.8: Schematic Fourier-transform holography setup. The coherent X-rays beam is diffracted by the object and reference apertures, the interference pattern of which is recorded in the far field. After Fourier inverting the measured hologram, the real-space images of the sample can be obtained.

Fourier-transform holograms were recorded in transmission geometry. The experimental setup, illustrated in Fig 2.8, follows the lines of the CDI scheme presented in Fig. 2.1, with the additional holography mask that contains the object and reference apertures within the same plane. A central black shadow can be seen in the recorded hologram due to the beamblock located in front of the CCD that stops the highly intense direct beam from impinging onto the detector. This beamblock is needed due to the fact that most detectors are not

capable of imaging the high dynamic range encountered at low spatial frequencies. As a consequence, the information close to zero momentum transfer is lost. Details about the effects introduced by the beamblock can be found later in this section. It is worth mentioning however, that even when no beamblock is used, the scattering data close to $\boldsymbol{q} = 0$ is still not reliable, as the forward scattering gets overlapped by direct transmission from the sample. A typical exposure time of $\sim 5\,\mathrm{s}$ per frame was required to record high-angle scattering, which saturates the first Fraunhofer ring (or Airy disk) outside the beamblock. Ten frames were accumulated at each photon energy to improve the counting statistics in the images.

The recorded hologram in Fig. 2.8 stands as an example of the diffraction measured from the sample. The shadow of the beamblock in the center is surrounded by the Airy rings that originate from the sample aperture with $2\,\mu\mathrm{m}$ diameter. Speckles created from the structure of the sample are visible throughout the hologram, in addition to the fringes arising from the object-reference interferences, as observed in the zoomed pattern. In order to reconstruct the images, the hologram is Fourier inverted by means of computational Fast Fourier Transformation (FFT), after first applying a Gaussian high-pass filter to remove effects arising from the abrupt change in intensity caused by the beamblock. This process results in the reconstruction shown in Fig. 2.8. The four terms of Eq. 2.10 are present in this reconstruction: the object-object and reference-reference autocorrelations form the undistinguishable pattern in the center of the image, while the six surrounding images are the object-reference cross-correlations from the three reference holes and their complex conjugates. The three object images are independent and identical apart from noise. Averaging them improves the image quality, and, since they have the exact same orientation, this can be done by mere translation of the images.

Beamblock effects

As a consequence from the limited dynamic range of the CCDs used, a beamblock needs to be placed in front of the detector in order to acquire good statistics from the high-angle scattering information. The size of the beamblock is chosen appropriately for the optimized acquisition of useful information. When the diameter is too small, the highly intense beam at $\boldsymbol{q} = 0$ saturates the detector limiting the data quality at higher $\boldsymbol{q}$ range, which results in reconstructed images with a poor SNR. On the other hand, using a beamblock too large starts blocking the information of relevant $\boldsymbol{q}$'s, with the consequent loss of data on the sample structure and domains. The optimum diameter is found to be the

one that blocks approximately the first ring outside the Airy disk.

In order to understand the effects of the beamblock on the reconstructed images, the actual transmitted intensity recorded in the CCD should be considered. Following Eq. 2.7, the measured intensity at the plane of the camera is given by:

$$I_M = MI, \tag{2.13}$$

where $M = M(X, Y)$ represents the beamblock function. The reconstructed image is, thus, obtained by Fourier transforming I_M:

$$\begin{aligned} \mathcal{F}^{-1}\{I_M(X,Y)\} = \mathcal{F}^{-1}\{MI\} = \\ + \mathcal{F}^{-1}\left\{M\left(OO^* + RR^* + OR^* + RO^*\right)\right\}. \end{aligned} \tag{2.14}$$

As before, the interesting term is the cross-correlation of the object with the reference, given by:

$$\begin{aligned} I_o = \mathcal{F}^{-1}\{MOR^*\} = \ & \mathcal{F}^{-1}\{M\} * \mathcal{F}^{-1}\{OR^*\} \\ & = \overline{M} * (o * r) \\ & = \overline{M} * o(x - d_x, y - d_y), \end{aligned} \tag{2.15}$$

where $\overline{M}(x, y)$ is the Fourier transform of the beamblock function. For the sake of simplicity, let's consider one dimension, where the beamblock mask can be represented as: $M = 1 - \mathrm{rect}(2X\omega)$, with $\mathrm{rect}(2X\omega) = 1$ for $|X\omega| < 1$, being ω the width of the mask. The resulting intensity of the displaced image of the object is:

$$\begin{aligned} I_o &= \left[\delta(x) - \frac{1}{2\omega}\mathrm{sinc}\left(\frac{x}{2\omega}\right)\right] * o \\ &= o - \frac{1}{2\omega}\mathrm{sinc}\left(\frac{x}{2\omega}\right). \end{aligned} \tag{2.16}$$

In the limit of a very small beamblock, $\omega \to 0$, it has no effect and the intensity of the object is simply $I_o \approx o$. For large beamblocks, several times bigger than the object aperture, the last term in the right hand side can be considered

nearly spatially independent, and effectively acts as a low-pass Gaussian filter that gives the average intensity of the object. Therefore, in the reconstructed image, the intensity obtained of each pixel is that of the real object subtracted by the average response of the sample.

As a result from the complete loss of $\boldsymbol{q} = 0$, the central beamblock can be regarded as a high-pass filter on the reconstructed image that subtracts the average transmission of the entire sample and enhances the edges of the structure. The immediate consequence of this effect for the current experiment is the loss of the absolute values of the transmission of VO_2, directly related to the absorption coefficient of the material. However, it is important to notice that relative spectra can still be obtained, as the last right-hand term in Eq. 2.16 cancel out when subtracting the intensities of two different pixels in the image, as given by:

$$I_o(x_1) - I_o(x_2) \approx o(x_1) - o(x_2). \tag{2.17}$$

The absolute values of intensity recorded for each phase depend thus on the average phase of the whole sample, which changes with temperature as the phase fractions grow. However, the contrast between phases remains, which allows the imaging of different phases when they are coexisting in the sample.

2.4 Nanoscale phase separation during the IMT of VO_2

Holographic imaging was performed on two different samples, both fabricated as explained in Section 2.3.2. As a first verification of the technique employed, the comparison of the scanning electron microscopy (SEM) images of the samples with the ones measured holographically is shown in Fig. 2.9. An excellent agreement is found between the two techniques, demonstrating the adequate spatial resolution of holography. Although the substrate of the films is amorphous, there are regions of the samples where micron-sized single crystals are formed among nanoscale crystallites. On the perimeter of these single crystals (indicated by the dotted white line), several defects can be observed, with features as small as 50 nm (indicated by arrows). The comparison of the spatial resolution of the holography image with that obtained by SEM is depicted in Fig. 2.9(b), where the line-cuts of the same feature show a comparable resolution. A sub-50-nm spatial resolution is achieved with holography, consistent with the size of the reference holes.

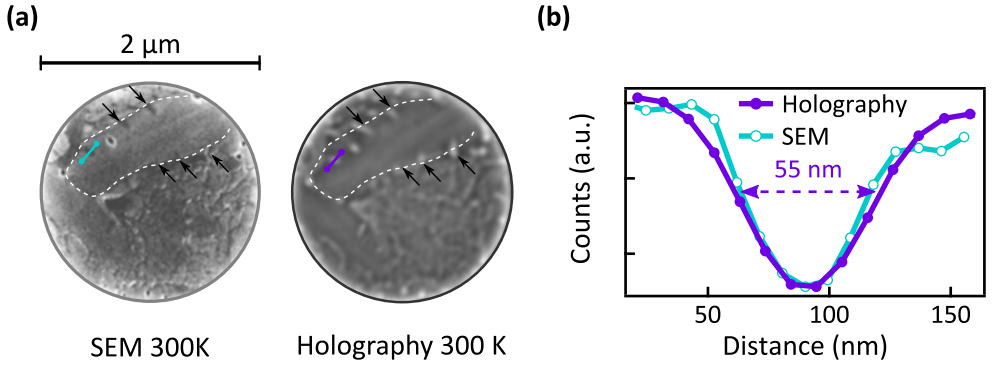

Fig. 2.9: Comparison of SEM with holography images. **(a)** Comparison of the images obtained at room temperature with the two techniques. The real-space image corresponds to the real part of the complex reconstruction measured at a photon energy of 530.5 eV. The field of view is 2 µm. **(b)** Line-cuts of one of the defects that demonstrate the adequate resolution of holography for the employed samples.

2.4.1 Metallic domain growth

According to the hysteresis curve seen in Fig. 2.5, 330 K marks the onset of the phase transformation. Heating the sample to this temperature and imaging

with X-rays tuned to the $d_{\|}$, should allow for the observation of the metallic phase growth. Indeed, in the images shown in Fig. 2.10, bright stripes appear across the crystals. These stripes are metallic domains observed due to the higher transmissivity of VO_2 in the metallic phase at 530.5 eV, as a result from the loss of the $d_{\|}$ absorption peak. Interestingly, these domains, while long, can be as narrow as 50 nm. From the domains evolution with temperature, it is clear that the nanoscale defects (pointed by arrows) nucleate the metallic phase, which grow with increasing temperature between such defects and spanning the single crystals. This demonstrates the role local strain plays in locally lowering the transition temperature. In addition, thermally cycling the sample proved that these domains are pinned, given their repeated growth in the same locations.

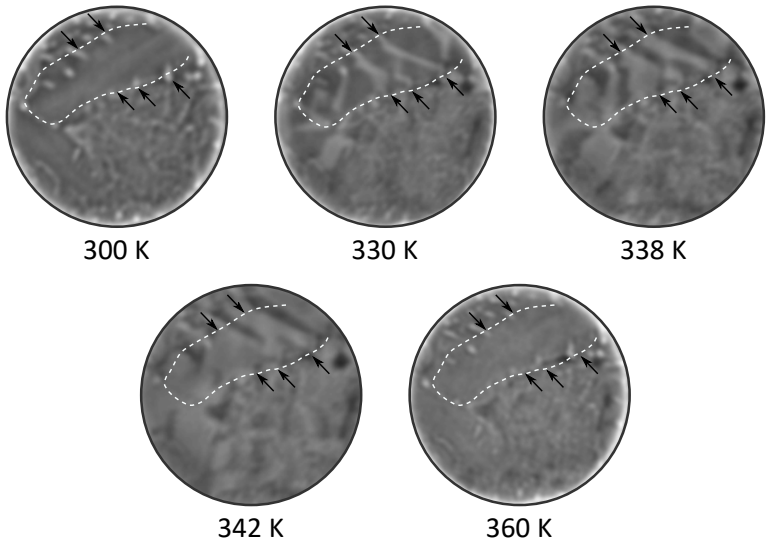

Fig. 2.10: Metallic domain thermal growth. The dotted white line indicates the perimeter of a single crystal, while some of the defects on the edges of the crystal are pointed out by arrows. The brighter stripes, corresponding to metallic domains, grow with increasing temperature spanning the single crystal, until the entire sample becomes metallic.

A further increase of the temperature results in the growth of the metallic filaments until the whole sample becomes metallic at 360 K. Given that defects appear as dark features in the SEM image and bright in the holography images, indicating high transmission, they can be associated with grain boundaries between VO_2 crystallites. In fact, nucleation sites at VO_2 grain boundaries are consistent with previous work that showed how oxygen vacancies created by strain at such locations present a decreased phase-transition energy [91].

2.4.2 The role of phase coexistence in the IMT

The investigation of coexisting M_1 and R phases during the insulator-metal transition in VO_2, as well as the potential presence of other phases, can give insight into the role played by phase separation and electronic correlations in the IMT. With this aim, spectrally resolved imaging at multiple X-ray wavelengths is performed. Ideally, extracting XAS spectra of each point in the images would allow to identify the state of the system. However, this is not possible due to the loss of information close to $\boldsymbol{q} = 0$ caused by the presence of the beamblock. In fact, when looking at Fig. 2.10, the images measured at the initial and final states at 300 K and 360 K, that correspond to the monoclinic M_1 and R phases, respectively, show no significant differences neither in structure nor in absolute intensity values between each other. However, provided the sample is within the temperature range where it is not fully M_1 nor R and phases coexist, the contrast between them remains and the different states of VO_2 can be thus imaged and studied. As demonstration, Fig. 2.11 shows the comparison of the differential spectrum of those measured at the low-temperature insulating phase and high-temperature metallic phase (shown in Fig. 2.7) with that obtained by subtracting the intensities of pixels from the insulating and metallic domains in Fig. 2.10. A very good agreement can be observed between them, which proves that relative transmitted intensities from different phases on the nanoscale can be obtained by this technique.

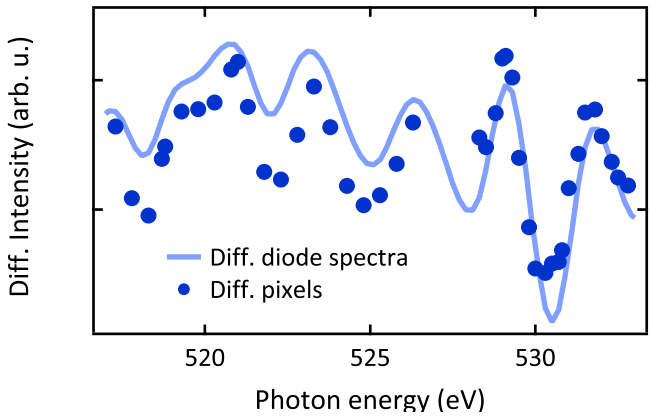

Fig. 2.11: Nanoscale relative spectrum of a metallic domain. The solid line corresponds to the difference of the metallic and insulating spectra shown in Fig. 2.7, obtained by measuring the transmission on a diode. The markers correspond to the relative spectrum of two selected regions of a few pixels wide within the insulating and metallic nanoscale domains shown in Fig. 2.10. The observed deviations from one another arise from the different background drifts between the two data sets.

The selection of the photon energies for imaging is not arbitrary, though. Recalling the interpretation of the XAS features in Section 2.2.2, images of the VO_2 sample are recorded at 530.5 eV, resonant to transitions into the $d_{\parallel}$ states, and at 529 eV, sensitive to the π^* and $d_{\parallel}^c$ states. Additionally, a photon energy on the vanadium L_2-edge of 518 eV is selected, since it is sensitive to the $d_{\parallel}$ states as well [52].

Given the dichroism of the $d_{\parallel}$ and $d_{\parallel}^c$ states in the insulating phase of VO_2, the orientation of the sample with respect to the X-rays electric field needs to be determined. For that purpose, images were recorded at the $d_{\parallel}$ peak at room temperature with different X-ray polarizations. This part of the experiment was performed using a different sample (Fig. 2.12) in a different setup: the MaReS end-station at BOREAS beamline [92] of the ALBA synchrotron light source. The geometry of the setup was held the same as the one employed at BESSY II. The X-ray polarization vector was rotated by 180° in 5° steps, and the differential images were studied at each angle in order to find the maximum dichroic signal (see Fig. 2.13). When the X-rays are parallel/perpendicular to the crystals rutile *c*-axis, the contrast is maximum due to the anisotropy of the $d_{\parallel}$ peak. This difference is lost when each polarization is rotated by 45° with respect to the *c*-axis.

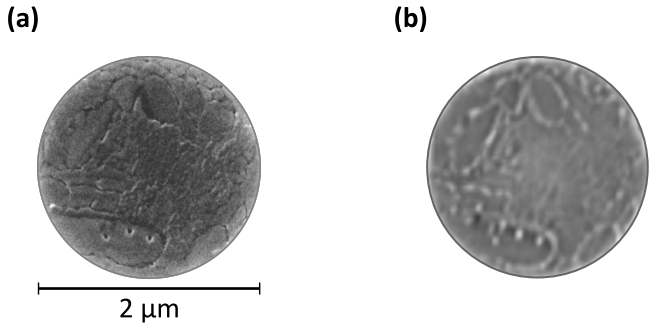

Fig. 2.12: SEM of the VO_2 sample used for phase-identification analysis. Again, both the SEM and holographic images are in good agreement. As with the previous sample shown, small crystals can be found among smaller crystallites.

Once the sample orientation is known, imaging with the photon energies selected and the X-rays polarized along the rutile *c*-axis can be performed. Images were recorded at intermediate temperatures between the M_1 phase and the complete transformation into the R phase. An RGB (red, green, blue) colour encoding is used to create a false-colour image to investigate thereby the changes of the above-mentioned states across the IMT. Images recorded

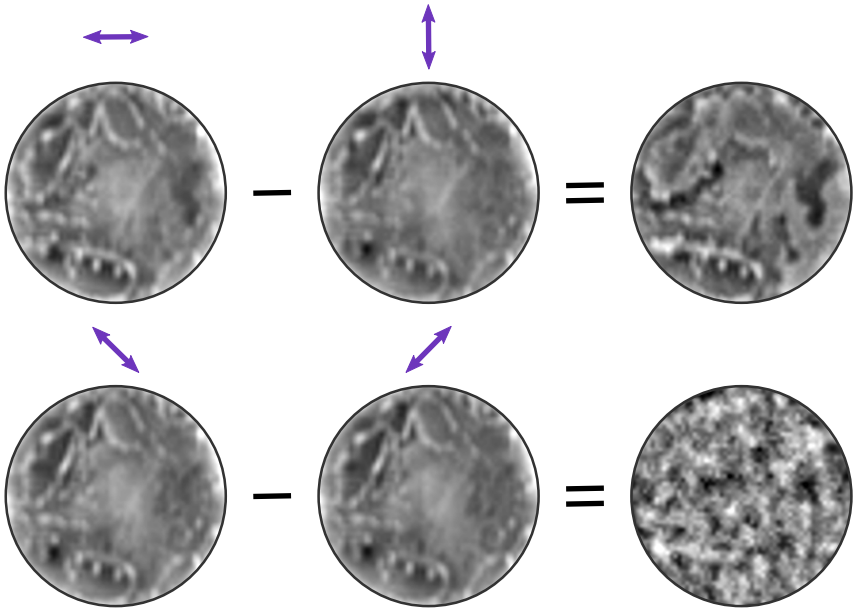

Fig. 2.13: Polarization-resolved imaging in VO_2. X-ray dichroic images of VO_2 measured at the $d_{\parallel}$ peak at room temperature. The tendency of the observed crystals is to grow along the rutile *c*-axis, giving rise to the existence of defined axes within the field of view. The dichroic images in the top row display brightest/darkest regions for those that have the *c*-axis aligned mostly along/perpendicular to the X-rays polarization. The contrast is gone when the X-rays are rotated by $45°/-45°$ with respect to the predominant *c*-axis.

at 518 eV, 530.5 eV, and 529 eV are used to encode the red, green, and blue channels of this composite image, respectively. In this spectral fingerprinting approach, it is easier to observe changes occurring in different regions of the sample and at different temperatures. For instance, according to Gray *et al.* [25], a weakening of electronic correlations precedes the structural transition. Thus, this would result in the blue channel ($d_{\parallel}^{c}$) changing before the green one ($d_{\parallel}$), and giving rise to a change of colour in the composite image.

The resulting RGB images at four selected temperatures are shown in Fig. 2.14. The nanoscale domains nucleate at the defects of the sample and span the single crystals, the same behaviour as observed in Fig. 2.10. However, with this colour encoding it now becomes evident that different regions of the sample change in a different way with increasing temperature. At 330 K, the start of the phase transition, there is an increase in intensity of the green channel. However, as the sample is heated further, the blue channel also changes but in different zones of the sample. As a result, at 334 K, at least three distinct phases can be observed: the initial M_1 phase and two new phases. One shows a change in the $d_{\parallel}^{c}$ state (blue channel), while the second presents the greater

change at the $d_{||}$ state (green channel).

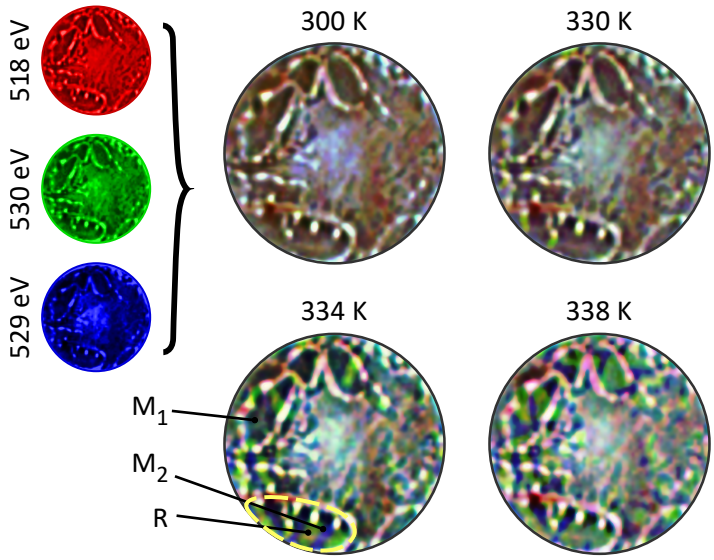

Fig. 2.14: RGB colour-encoded images formed by spectrally resolved images at the V and O edges. The images measured at 518 eV, 530.5 eV, and 529 eV are used to encode the three colour channels of an RGB false-colour image, respectively. New phases, depicted by different colours, nucleate and grow with increasing temperature. The dashed line delimits the selected ROI for further analysis.

To understand the growth of these three phases, a finer temperature scan is performed and the analysis is focused on the small single crystal indicated by a dashed line in Fig. 2.14, the new region of interest (ROI). To amplify the changes, an additional threshold is applied to each colour channel. Due to the loss of the absolute intensity values of each phase and the effective subtraction of the average intensity of the sample caused by the presence of the beamblock, when the temperature is increased and the metallic phase fraction grows, a manual adjustment of the threshold is required to ensure the contrast is not lost for each temperature. An upper threshold is also applied to each colour channel in order to move the white regions (corresponding to defects and boundaries of the crystals in Fig. 2.14) into the red channel of the new RGB composites formed by the binary images.

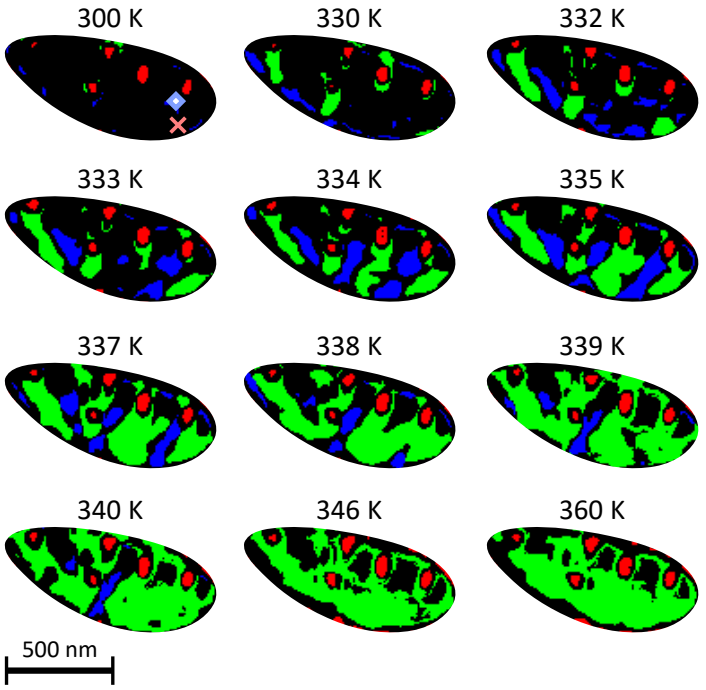

Fig. 2.15: Threshold images of domain growth in VO_2 of the single crystal outlined in Fig. 2.14. Growth starts from defects (red) and the striped phase formed by the M_2 and R phases is seen at $\sim$ 334 K. The diamond and cross markers are the ROIs used in Fig. 2.16.

.

The resulting images at some key temperatures are presented in Fig. 2.15. Initially, at room temperature, the sample is predominantly black within this colour-coding scheme, indicating that the crystal is in the M_1 phase, whereas the red spots correspond to defects. As the sample is heated, the new phases (green and blue) nucleate at the boundaries and defects of the single crystal. At 334 K, a striped pattern is formed by the green and blue channels, which is already visible in Fig. 2.14, before the green channel dominates the region at higher temperatures. This phase growth is captured in Fig. 2.16(a), which displays the volume fraction of the blue and green regions as a function of temperature within the ROI. Both phases start to nucleate at similar temperatures and grow, before the green area dominates.

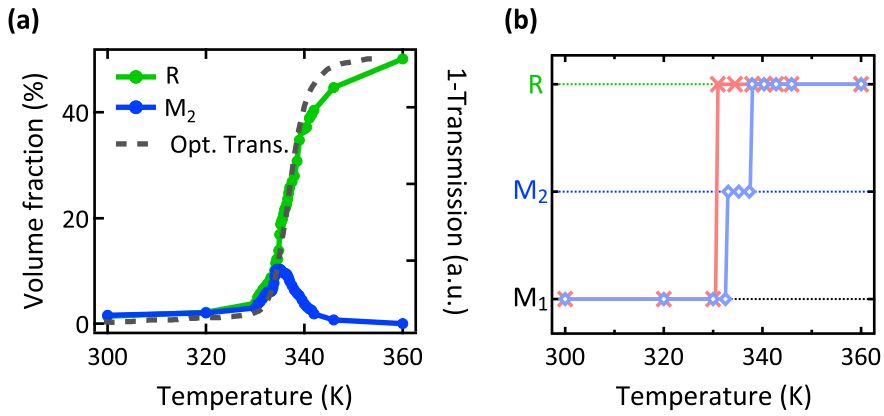

Fig. 2.16: Temperature-dependent growth of two phases in VO_2. **(a)** The volume fraction of the M_2 phase peaks at $\sim 335\,K$ before the whole sample becomes metallic. As indicated by the dashed line, the growth of the R phase is in good agreement with the optical transmission shown in Fig. 2.5. **(b)** Temperature dependence of the local transition pathway of the two regions marked in Fig. 2.15. The area marked with the cross shows a direct transition from M_1 to R, while that marked with a diamond transitions via the M_2 phase at a slightly higher temperature.

.

The green regions, which probe changes in the $d_{\parallel}$ states, can be easily identified as the metallic R domains, the one that dominates at high temperatures. If, as discussed in Section 2.2.2, the $d^c_{\parallel}$ states are probing electronic correlations, and changes in these precede the structural transition, all the green regions should first turn blue. However, this is not the case, as most regions present a direct transition from the initial M_1 to R, without any intermediate changes. Only in some spatially distinct areas, the intermediate blue domains are observed. This is highlighted in Fig. 2.16(b), which shows the phase of two selected nanoscale areas ($\sim 50\,nm$, depicted with symbols in Fig. 2.15) as a function of temperature. The region marked with the cross follows a direct M_1-to-R transition, while the one marked with the diamond goes through an intermediate phase.

This behaviour suggests that the loss of correlations is not the driving mechanism for the insulator-metal phase transition. In the light of these new results, the two different transition temperatures reported by Gray *et al.* [25] for the electronic and structural transitions correspond instead to regions of the sample taking different pathways towards the metallic phase.

As strain appears responsible for nucleating the phase transition, and considering VO_2's phase diagram, the blue regions can be assigned to the mono-

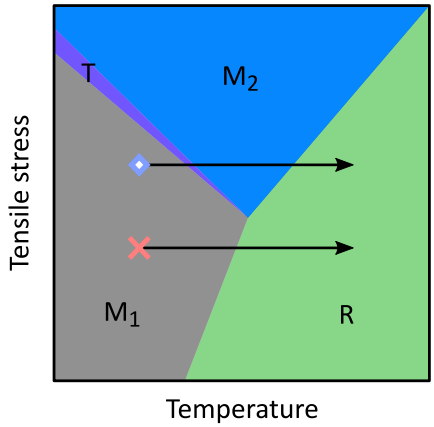

Fig. 2.17: Local transition pathways within the phase diagram of VO_2 of two different nanoscale regions of the sample. Areas in the sample that support higher strain transforms from the insulating M_1 to the metallic R phase by going through the intermediate insulating M_2 phase.

.

clinic M_2 phase, which is frequently observed in macroscopically strained samples. This interpretation, in which regions of the sample follow different local pathways from the M_1 to the R phase, is schematically depicted in Fig. 2.17. This assignment is further justified by recent DFT calculations of the M_2 density of states, which show anisotropic changes in the d_{xz} and d_{yz} orbitals [93], the ones that form the π^* states. This results in polarization-sensitive changes in the vicinity of the $d_{\|}$ XAS feature. However, the triclinic insulating phase cannot be excluded.

2.4.3 Discussion

The presented spatially resolved measurements suggest a new interpretation of the insulator-metal phase transition in VO_2 thin films. Nanoscale defects existing in the sample modify the strain environment, locally reducing the phase-transition temperature for the M_1-to-R transformation. Due to the large volume difference of the rutile phase, a new strain field is generated that can in turn also nucleate the M_2 phase. Both phases, M_2 and R, continue to grow and form a striped-phase pattern due to the interaction of the strain field. This phenomenon has also been observed in larger nanobeam single crystals [27, 40, 65, 94]. As the temperature is further raised, a complete transformation of the M_2 to the R phase occurs. The temperature separation observed in Fig. 2.16(b) between the formation of M_2 and R domains, of $\sim 5\,\mathrm{K}$, is in good agreement with the shift in temperature observed by Gray *et al.* [25].

In some respects, observation of the M_2 phase is unexpected, as the samples used have no epitaxial strain arising from the substrate to move the material away from typical M_1-to-R pathway. However, this is explained by the role nanoscale defects play in locally modifying the strain environment, which can dramatically modify the phase transition in VO_2 and in correlated materials in general.

This interpretation can also account for previously reported XAS observations, in which irreversible changes in the vicinity of $d_{\|}^{c}$ were reported during thermal cycling the sample [82], as a stabilization of the M_2 phase at room temperature due to a change in the local strain field. Nevertheless, the transition temperatures and growth patterns will depend on the local distribution, which is sample specific. In the measurements reported here, the observed domain patterns were repeatable after thermal cycling the samples, again suggesting that strain derived from extrinsic defects is the dominant mechanism, pinning domain walls and giving rise to the observed structure [95].

2.5 Conclusions

The reported imaging experiment during the insulator-metal phase transition in VO_2 presents no evidence for decoupled electronic and structural transitions, where the weakening of electronic correlations gives rise to the existence of a monoclinic metallic phase. Instead, these results demonstrate that the phase transition can be explained in terms of phase separation into the known phases of VO_2 and the different transition pathways among them.

This work shows that soft X-ray resonant holographic imaging can be used to image domain growth on the nanoscale, providing polarization- and energy-resolved measurements of samples that have a heterogeneous response. As phase separation is a common property of correlated materials, this technique will be vital in understanding the role played by defects in the electronic and structural properties of them. Furthermore, the main advantage becomes apparent when combining holography with ultra-short X-ray pulses generated by free-electron lasers as the light source. The first attempts of imaging domain growth on the nanoscale over a wide field of view in VO_2 with femtosecond time resolution are described in Appendix A.

3 | The role of heat in the phase transition of VO_2

This chapter describes the effect laser-induced heating and the recovery dynamics of VO_2 may have on the photo-induced phase transition. Section 3.1 provides an introduction about the threshold-like behaviour of VO_2, which can be affected by the recovery dynamics. These are studied in Section 3.2 under different experimental conditions, followed by a measurement of the threshold fluence required to drive the ultrafast transition when probed with different optical wavelengths in Section 3.3. The conclusions of the chapter are discussed in Section 3.4.

3.1 Introduction

Many materials that exhibit a light-induced phase transformation do so when the energy density of the employed pump laser exceeds a specific threshold [96, 97]. In VO_2, threshold fluences in the range of 4.6–7 mJ cm^{-2} have been reported for the photo-induced transition with 800-nm laser light at room temperature [45, 47–49, 54, 56]. In the linear absorption regime, this excitation density corresponds to 10 % of the vanadium atoms.

In VO_2, there are generally three different regimes in the photo-induced phase transition as a function of pump fluence, as depicted in Fig. 3.1, which can be observed in optical as well as in X-ray experiments. For fluences below the threshold, the response is linear with fluence. Above threshold, a sharp change occurs, which results in a significantly larger dependence of the materials properties on increasing fluence. Finally, above the saturation fluence, the response exhibits a weak dependence on excitation density. The below-threshold regime can be interpreted as the sample in the insulating phase, where the pump fluence values are not sufficient to induce the phase transition. Just above threshold, but below the saturation regime, the response is mixed, with both fast and slow dynamics observed. Most likely, this results from only a small part of the probed volume transforming instantly into the metallic phase. Thermal diffusion of heat then results in nucleation and growth of metallic domains [98]. Increasing the pump fluence leads to a more rapid transition, until saturation is reached, where the whole probed volume has been transformed and optical or X-ray-probed properties do not further change.

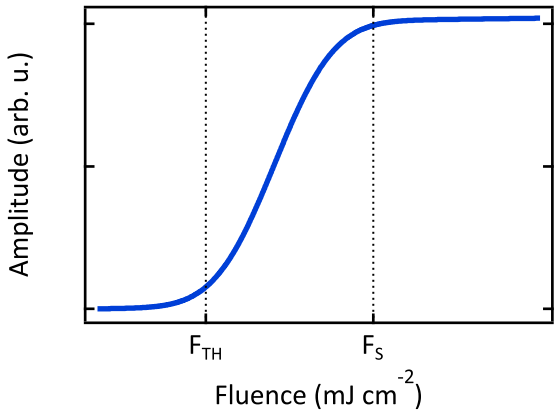

Fig. 3.1: Fluence-dependent optical/X-ray response during the photo-induced phase transition of VO_2. The three regimes observed are characterized by the values of F_{TH} and F_S, which are the threshold and saturation fluences, respectively.

Recently, the threshold fluence values for triggering the phase transition in VO_2 have been employed as evidence for the existence of a transient metal-like monoclinic phase. Through ultrafast electron diffraction experiments, Morrison *et al.* provided evidence for the existence of not one, but two threshold fluences for the phase transition [51]. Above $2\,\mathrm{mJ\,cm^{-2}}$, they observed slow ($1.6 \pm 0.2\,\mathrm{ps}$) dynamics of the measured diffraction peaks intensity, which suggested a valence charge density reorganization within the monoclinic structure. The fast melting ($310 \pm 160\,\mathrm{fs}$) of the V-V dimerization, and hence the structural phase transition, was found to occur above a threshold fluence of $9\,\mathrm{mJ\,cm^{-2}}$. The authors complemented these results with fluence-dependent time-resolved IR transmittance measurements that showed a metal-like response for fluences below the required $9\,\mathrm{mJ\,cm^{-2}}$ for the crystallographic transition. As a result, they suggested the presence of an intermediate monoclinic phase with metallic properties existing in the intermediate fluence regime between the two thresholds reported.

The observation of different thresholds through pump-fluence dependent studies for the onset of the metallic state and the structural distortion stands as evidence for supporting the decoupled nature of the phase transition in VO_2, as well as the existence of an intermediate monoclinic metallic state. While structure-sensitive probes, such as electron [50, 51, 56] and X-ray [45] diffraction, have provided fluence threshold values within the range 4–$8\,\mathrm{mJ\,cm^{-2}}$, metallic-like behaviours have been measured by exciting the sample with fluences as low as in the 1–$2\,\mathrm{mJ\,cm^{-2}}$ range [51, 99, 100].

However, determining the absolute excitation strength necessary for driving the transition is a challenging task which has been approached by several different techniques in the past. The difficulty of experimentally measuring accurate fluence values, together with variations arising from different types of VO_2 samples and technique-dependent probed volumes, causes the comparison of threshold fluences to have a limited validity.

The high sensitivity of threshold fluences on external parameters was already observed in the early pump-probe measurement conducted by Cavalleri and co-workers in 2001 [45], where the pump threshold fluence in VO_2 was found to strongly depend on the initial base temperature of the sample. This effect was subsequently reported by the group of Leitenstorfer *et al.* [48, 49] through multi-THz probe pulses. They measured a decrease of the threshold fluence and a longer-lived photo-induced conductivity upon raising the sample temperature towards T_C. Furthermore, the energy required to drive the transition optically was found to be the same as the energy difference between the metallic and the insulating phase at a given initial temperature, that is, the

energy necessary to thermally drive the transition, in agreement with previous experiments [56].

While the coincidence of the thermal and photo-induced phase transition thresholds seems to suggest a common pathway for both processes, some research groups claim that this is not the case. Instead, they attributed this effect not to a thermal nature of the phase transition, but to a softening of the insulating phase near threshold caused by the existence of metallic precursors at temperatures closer to T_C that facilitate the metallic phase growth [47]. Additionally, other experiments based on time-resolved THz spectroscopy [101], which compared a phase transition triggered by laser-induced heating to thermal predictions, found that, although these coincide near room temperature, there is a strong divergence of the observed thresholds from thermal predictions at low temperature. They measured a metallic-like conductivity when exciting the sample with fluences below those necessary to thermally drive the transition.

The temperature dependence of the threshold fluence in [47–50, 56] was observed by deliberately heating the sample *in situ*. Threshold fluences are normally determined by scanning the response of the material to increasing pump fluences. However, in these experiments, which assume the sample always recovers back to its ground state, the initial temperature of the sample is assumed to be always the same. Yet, due to the repetitive nature of pump-probe measurements, this premise results not necessarily true. Laser-induced heating can in fact lead to heat accumulation when the repetition rate of the laser pulses is too high for the material to fully recover back to the ground state before the next pulse arrives. When this is the case, the system may be driven towards a new quasi-equilibrium temperature that is higher than the initial one and depends on the fluence with which the sample is excited. Consequently, the responses at different fluence values cannot be compared to each other, as these are relative to different base temperatures.

The recovery of VO_2 samples in pump-probe measurements has been discussed by a few experiments. In the femtosecond electron diffraction experiments conducted in 2007 by Baum *et al.*, the repetition rate of 1 kHz was found sufficient for a single crystal of VO_2 held at room temperature to completely recover to the initial monoclinic phase [56]. Nonetheless, in the later UED measurements led by Morrison *et al.* in 2014 on free-standing thin-film samples, a repetition rate of 50 Hz between pump pulses was necessary for the samples to relax back to the ground state [51]. More recently, in a femtosecond XUV transient absorption spectroscopy study of 2017, Jager *et al.* had to take an extra measure to avoid heat accumulation, as the minimum feasible repetition

rate of 100 Hz in their experimental setup was comparable to the inverse time for heat dissipation in the thin-film samples employed. With that aim, the sample mount was rapidly rotated normal to its surface, so that subsequent pump pulses did not impinge on the same region of the film. In 2018, the same group provided theoretical simulations for estimating the rate of heat buildup between laser pulses in particularly heat-sensitive VO_2 samples under vacuum conditions. They showed how, even at low repetition rates of 100 Hz, after the first six pulses the temperature of the material had already raised above T_C. As a result, all subsequent probe pulses measured the response of the metallic instead of the insulating phase.

In order to understand the different recovery time scales found for single crystals and thin films it should be noted that the time scales for heat dissipation are set by the temperature gradient generated in the sample by the laser pulses. In absorbing samples, the penetration depth of laser light is generally of a few hundred nanometers, leading to temperature gradients on these length scales for thick samples, such as single crystals. This results in recovery times on the nanosecond time-scales for thermal diffusivities of $10^{-5}\,m^2s^{-1}$. However, for free-standing thin-films, which are thinner than the absorption length, there is no thermal gradient into the depth of the material. Therefore, heat transport can only occur in the transverse direction. The thermal gradient on this plane is set by the pump spot-size, of the order of a few hundreds of microns in X-ray and electron diffraction experiments such as those mentioned above. This results in recovery times that are six orders of magnitude longer, within the millisecond regime. Ideally, all measurements would be performed on single crystals to avoid heat accumulation issues. This is not always possible, though, as the extremely short penetration depths of electron and X-rays makes necessary the use of free-standing samples for this type of experiments.

Despite the interplay between temperature and optical excitation being acknowledged by the few above-mentioned experiments, the precise relationship between them remains still mostly unknown, and the distinction between thermal and non-thermal transitions results hindered by the high temperatures at which the experiments are generally performed. Understanding the time scales required for the samples to recover is crucial for the correct execution of time-resolved pump-probe measurements. Unfortunately, laser-induced heat buildup and the consequent fluence-threshold sensitivity to external parameters have been mostly neglected, which may have result in apparently contradictory results over the course of the past 50 years of studies of the insulator-metal phase transition of VO_2.

In order to give insight into the influence of laser-induced heating on driv-

ing the insulator-metal phase transition, a thorough study is presented in the following sections of the different experimental parameters that affect the phase transition threshold by means of long-delay time-resolved optical experiments on thin film samples. These measurements are complemented by the fluence-dependent change in transmission of the sample in femtosecond time scales probed with different wavelengths, to determine the existence of decoupled thresholds within the phase transition.

3.2 The recovery dynamics of a thin film of VO_2

As previously explained, according to literature, the type of free-standing thin films of VO_2, as those employed for the work of this thesis, exhibit total recovery times of the order of tens of milliseconds. The aim of this work is to measure the exact times required for the samples to relax back to their initial state. Typically, pump-probe setups involve the use of mechanical delay stages for controlling the arrival times of the pump and probe pulses to the sample. However, using stages longer than several nanoseconds becomes impractical, as the required lengths are too large. As a result, a different approach needs to be adopted for the measurement of recovery times in the millisecond regime.

Here, a combination of ultrashort-laser pulses with a CW light source was employed for the measurement of long dynamics. The experimental setup, which follows a typical pump-probe configuration, is schematically depicted in Fig. 3.2. The pump pulses have a time duration of approximately 40 fs centred at a wavelength of 800 nm, the repetition rate of which can be varied by integer division of the highest 5 kHz. The probe is a continuous-wave helium-neon (HeNe) laser with a central wavelength of 632.8 nm used to monitor the transmission of the sample after photo-excitation. The transmitted light is recorded by a high-bandwidth silicon balanced amplified photodetector connected to a LeCroy oscilloscope that provides a maximum bandwidth of 4 GHz and 40 $GS\,s^{-1}$ sampling rate. This way, a long-range time-resolved signal can be measured, limited by the electronics of the employed detector and oscilloscope. The ultimate temporal resolution is limited though by the RF output bandwidth of the photodetector of 1 MHz. The HeNe probe is split into two beams that follow different paths before impinging on the detector. One measures the transmitted light from the sample while the other acts as a reference. The sample is held inside a liquid-nitrogen cryostat that allows measurements at lower temperatures at pressures in the order of 10^{-6}–10^{-8} mbar.

Given the long time scales dynamics measured here, the contributions to the response of the system can be considered mostly thermal, as in the microsecond regime, electrons have already transferred their energy to the lattice. Therefore, as demonstrated throughout the next sections, the dynamics measured with this experimental setup can be understood in terms of heat transport within the sample and temperature differences. In the following section, the time traces measured under different experimental conditions are presented.

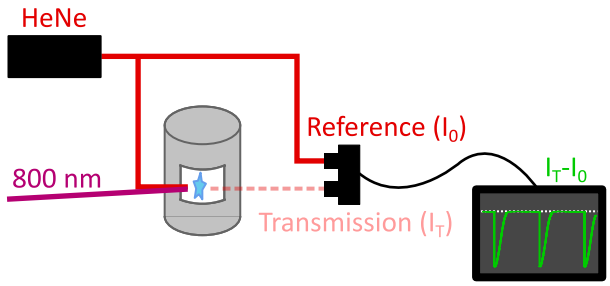

Fig. 3.2: Optical pump-probe experimental setup. The transmitted intensity from the sample is recorded by a balanced photodiode, the output of which is the difference between the transmission and the reference source.

Case 1: 50 Hz, room temperature, air

As a first step, the recovery of a thin-film sample is studied at atmospheric pressure and room temperature when excited by pump pulses at a repetition rate of 50 Hz, as 20 ms has been reported enough time for the sample to recover [51]. A total time range of 50 ms was recorded with the oscilloscope at a sampling rate of 1 MSs^{-1}, which provides a temporal resolution in the microsecond regime. The photodetector was balanced to a zero amplitude for the transmission of the sample without excitation. The resulting time traces obtained by exciting with different fluences are shown in Fig. 3.3(a), where it can be seen how the sample is excited every 20 ms and recovers back to the ground state before the next pump pulse arrives.

By looking into a shorter time range, the detailed traces can be studied, as displayed in Fig. 3.3(b). Three pump fluence regimes can be extracted from these measurements. At low fluences and below the phase transition threshold (Fig. 3.3(c)), the transmission is reduced immediately after photo-excitation, followed by an exponential recovery. The starting of the photo-induced phase transition can be clearly seen, when the sample is excited with higher fluences, by the emergence of an increase in transmission (Fig. 3.3(d)). Further increasing the excitation density leads to a saturation regime, where the amplitude of the signal no longer increases as the whole probed sample volume has already transformed into the metallic phase (Fig. 3.3(e)). As expected, the elapsed time between photo-excitation and full recovery gets elongated as the pump fluence is increased. However, under the present conditions, the repetition rate of 50 Hz appears to be sufficient for the sample to recover between pulses, at least up to the damage threshold of the sample.

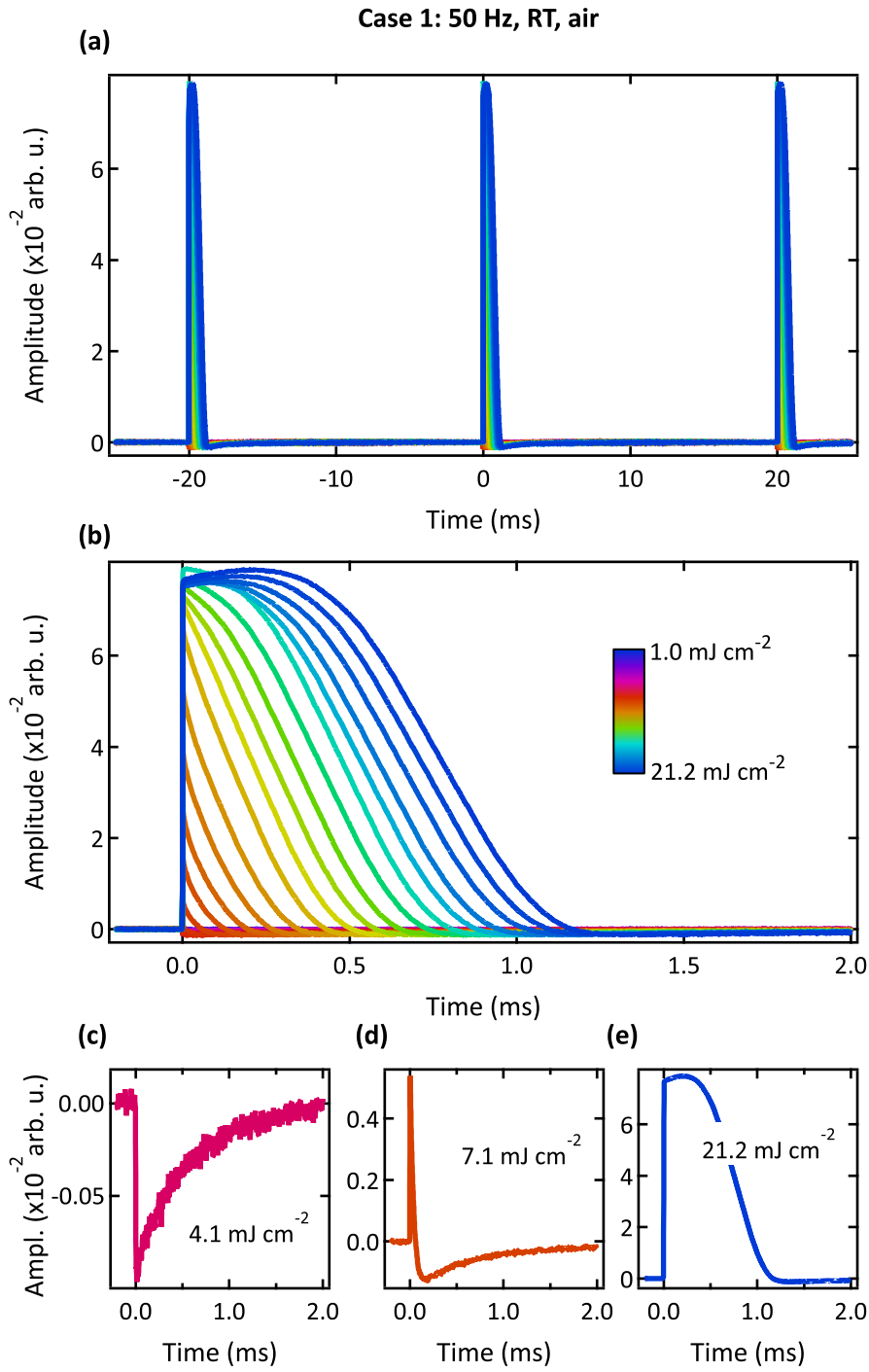

Fig. 3.3: Time traces at 50 Hz repetition rate, room temperature, atmospheric pressure. **(a)** Total temporal range measured. **(b)** Zoomed-in temporal window of 2 ms, where it can be appreciated how the response changes for increasing fluences. Time traces measured after pump excitation in the below-threshold regime (**(c)**), above the threshold fluence in **(d)**, and in the saturation regime in **(e)**.

Case 2: 50 Hz, room temperature, vacuum

Interestingly, when analysing the response of the sample to photo-excitation under identical pump-probe conditions but with the material held at 10×10^{-7} mbar, as opposed to the atmospheric pressure of the previous case, the behaviour is quite different. Figure 3.4(a) shows the time traces measured over the entire time range of 20 ms. It can be easily observed how, as the pump fluence is increased, the response of the sample has not enough time to recover within the employed repetition rate. Figures 3.3(c) and 3.4(b) were measured with the same excitation of $4.1\,\mathrm{mJ\,cm^{-2}}$, however, in the latter, the response amplitude is about the same, but the recovery time is significantly longer (note the different time range) due to the lack of thermal transport between the air and the sample in vacuum conditions. Also, the threshold fluence appears to be lower than $6.5\,\mathrm{mJ\,cm^{-2}}$, as in Fig. 3.4(c), after an excitation of $5.1\,\mathrm{mJ\,cm^{-2}}$ the sample has already started to switch into the metallic phase. From these time traces, the threshold fluence is found at $\approx F_{\mathrm{TH}} = 4.5\,\mathrm{mJ\,cm^{-2}}$. It should be noted that, even at these low fluences, the transmission is non-zero at negative time delays, and becomes positive above $\approx F_{\mathrm{TH}} = 10.5\,\mathrm{mJ\,cm^{-2}}$. This suggests, as observed in Fig. 3.4(d), that the sample is still in the metallic phase when the next pump pulse arrives.

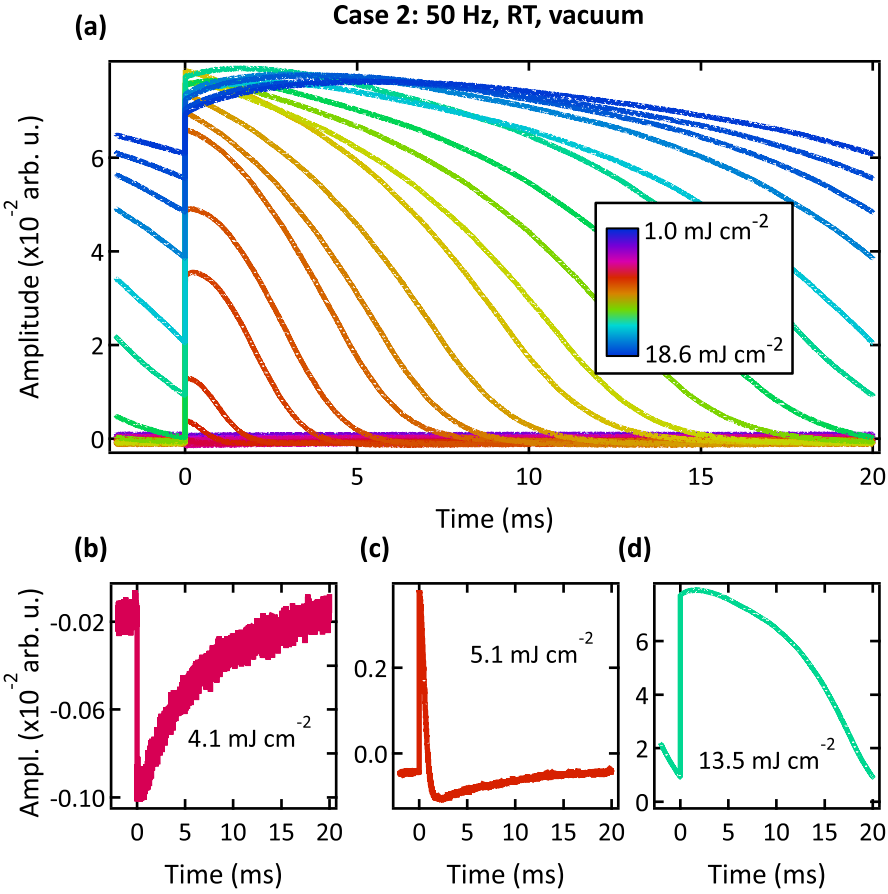

Fig. 3.4: Time traces at 50 Hz repetition rate, room temperature, in vacuum. **(a)** Fluence-dependent recovery of the sample within the 20 ms between pump pulses. Time traces measured after pump excitation in the below-threshold regime in **(b)**, above the threshold fluence in **(c)**, and in the saturation regime in **(d)**.

Case 3: 50 Hz, 90 K, vacuum

As reported in literature [47–49, 56], the threshold fluence depends on the base temperature of the sample. This is tested now by keeping the same pump-probe conditions from the previous case, but lowering the temperature of the sample to 90 K. As shown in Fig. 3.5, the resulting behaviour is quite different, and heat accumulation effects are not as dramatic, if present. Figure 3.5 displays again the time trace corresponding to a low excitation density of $4.1\,\mathrm{mJ\,cm^{-2}}$, which shows a recovery time of the same order as that exhibited in Fig. 3.4. The amplitude of the signal is slightly larger in this case, which could be due that at this fluence, when the sample was held at a base temperature of 294 K, some small fractions of the probed volume have already transformed into the metallic phase. Fig. 3.5(c) shows the response just after the start of the phase transition, which appears to occur at $\approx F_{\mathrm{TH}} = 15.5\,\mathrm{mJ\,cm^{-2}}$, a much higher value than in the previous cases. Also, at $20.8\,\mathrm{mJ\,cm^{-2}}$ (Fig. 3.5(d)), the saturation regime has not been reached yet, as opposed to the previous cases.

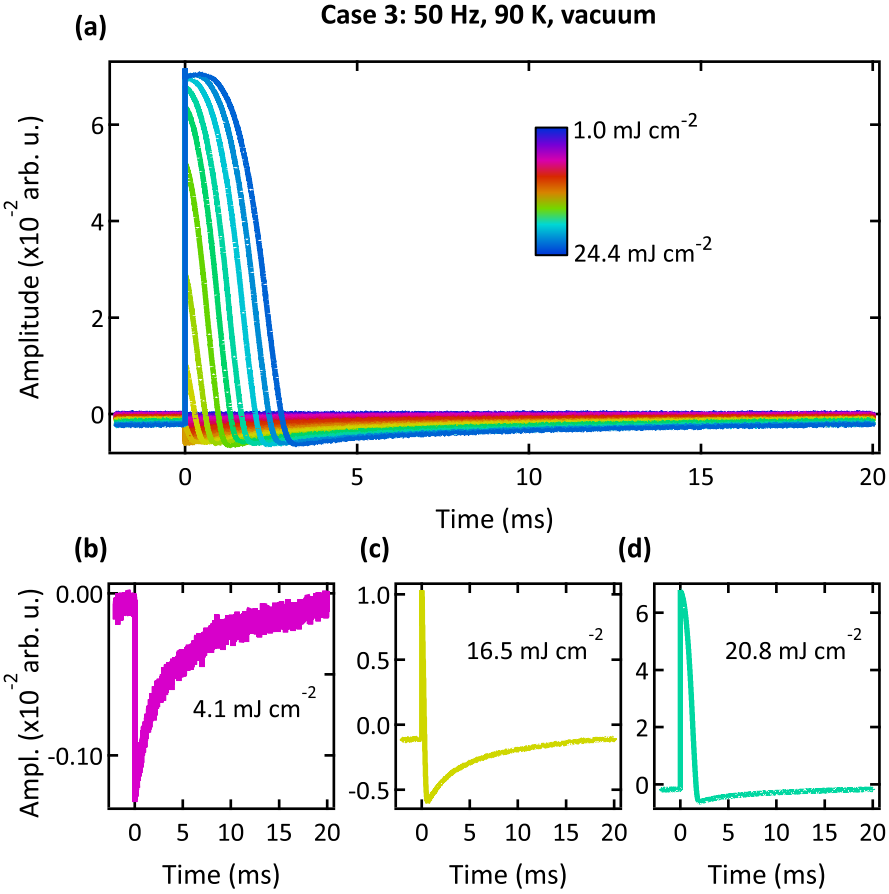

Fig. 3.5: Time traces at 50 Hz repetition rate, 90 K, in vacuum. **(a)** Fluence-dependent recovery of the sample within the 20 ms between pump pulses. Time traces measured after pump excitation in the below-threshold regime in **(b)**, above the threshold fluence in **(c)**, and in the saturation regime in **(d)** .

Case 4: 500 Hz, room temperature, air

From the three cases presented before, it can be concluded that the optimum conditions for performing pump-probe measurements on free-standing thin films is with a laser pump repetition rate of 50 Hz and the sample held in air. Nonetheless, these conditions are not always feasible, especially when working at external facilities, such as synchrotrons and FELs, where the sample chamber and laser settings are not tunable. Many of the experiments conducted on VO_2, both within this thesis (see Chapters 4 and A) and reported in literature, are in fact carried out in this type of facilities, where the sample needs to be maintained under vacuum conditions, or there exists a lower limit for the laser repetition rates due to experimental constraints, for instance. Therefore, it is worth considering the consequences of these possible scenarios for the thermal recovery of the films employed.

Figure 3.6 presents the temporal response of the sample held at atmospheric pressure, but excited with a repetition rate of 500 Hz. For this frequency, a total time range of 5 ms was recorded at a sampling rate of 10 MS/s. At low fluences (Fig. 3.6(a)), the recovery rate seems to be of the same order as in Case 1, in air conditions. The start of the phase transition, though, is found at $\approx F_{\mathrm{TH}} = 5.2\,\mathrm{mJ\,cm^{-2}}$, slightly lower, which stands as an indication for some DC heating. This is evidenced by the fact that above $\approx F_{\mathrm{TH}} = 21\,\mathrm{mJ\,cm^{-2}}$, fractions of the sample are still in the metallic phase when the next pump pulse arrives (Fig. 3.6(d)). The fluence range in which the insulator-metal transition can be probed is quite large, though.

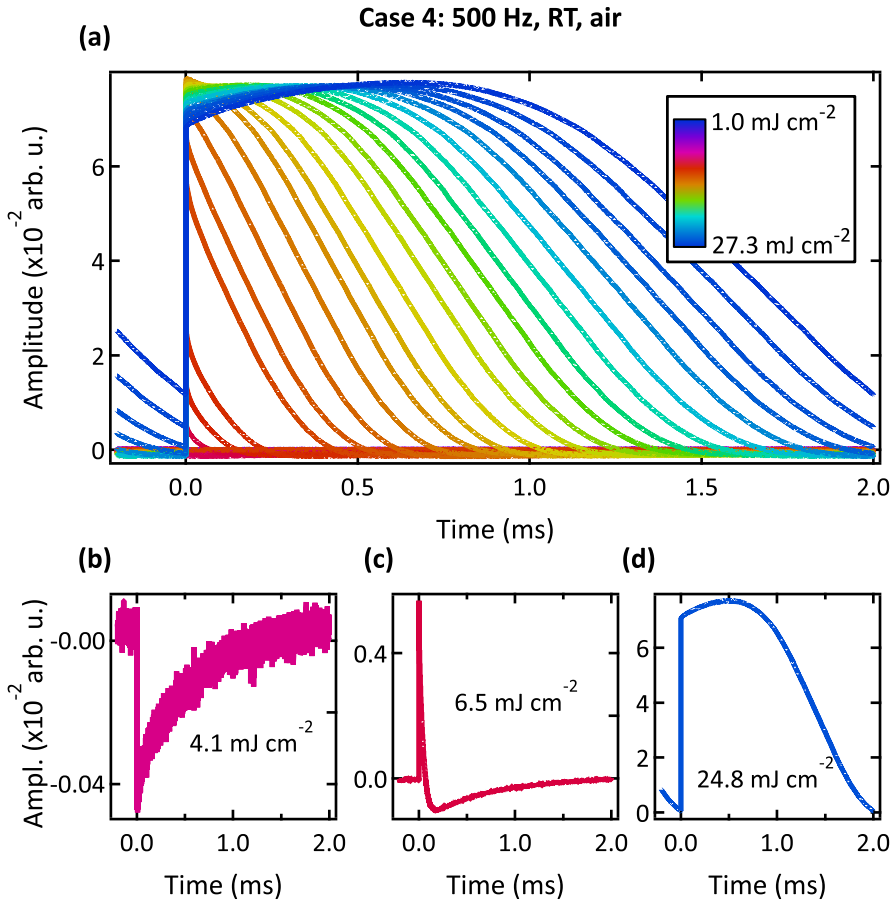

Fig. 3.6: Time traces at 500 Hz repetition rate, room temperature, at atmospheric pressure. **(a)** Fluence-dependent recovery of the sample within the 2 ms between pump pulses. Time traces measured after pump excitation in the below-threshold regime in **(b)**, above the threshold fluence in **(c)**, and in the saturation regime in **(d)**.

Case 5: 500 Hz, 90 K, vacuum

An alternative scenario corresponds to the situation where the sample needs to be maintained in vacuum. Not surprisingly, in the light of results from Case 2, it is not possible to measure the photo-induced insulator-metal transition in vacuum at room temperature, as laser-induced heating at this repetition rate permanently switches the sample into the metallic phase already at very low fluences. This can be partially overcome by lowering the base temperature, so that the induced heat is not sufficient to induce the transition.

The response of the sample held in vacuum at 90 K and excited with a frequency of 500 Hz is displayed in Fig. 3.7(a), where a quite different behaviour can be immediately appreciated. The heat build-up appears already at low fluences, as shown in Fig. 3.7(b), identifiable by the linear-like behaviour within the repetition rate employed, consequence of the short time range allowed for the exponential to grow. Because of this heat effect, the phase transition is induced at a fluence threshold of $\approx F_{\mathrm{TH}} = 4.7\,\mathrm{mJ\,cm^{-2}}$ and not at a higher value than in case 4, as it would be expected for a lower base temperature. When the initial temperature of the sample is above T_{C}, excitation leads to a further growth of the metallic volume, as seen in Fig. 3.7(d).

These two last cases represent a possibility for measuring the photo-induced insulator-metal dynamics when the experimental setups do not allow working under optimum conditions, namely, low repetition rates and atmospheric pressure. Despite the presence of heat accumulation, the phase transition can still be probed within a limited fluence range.

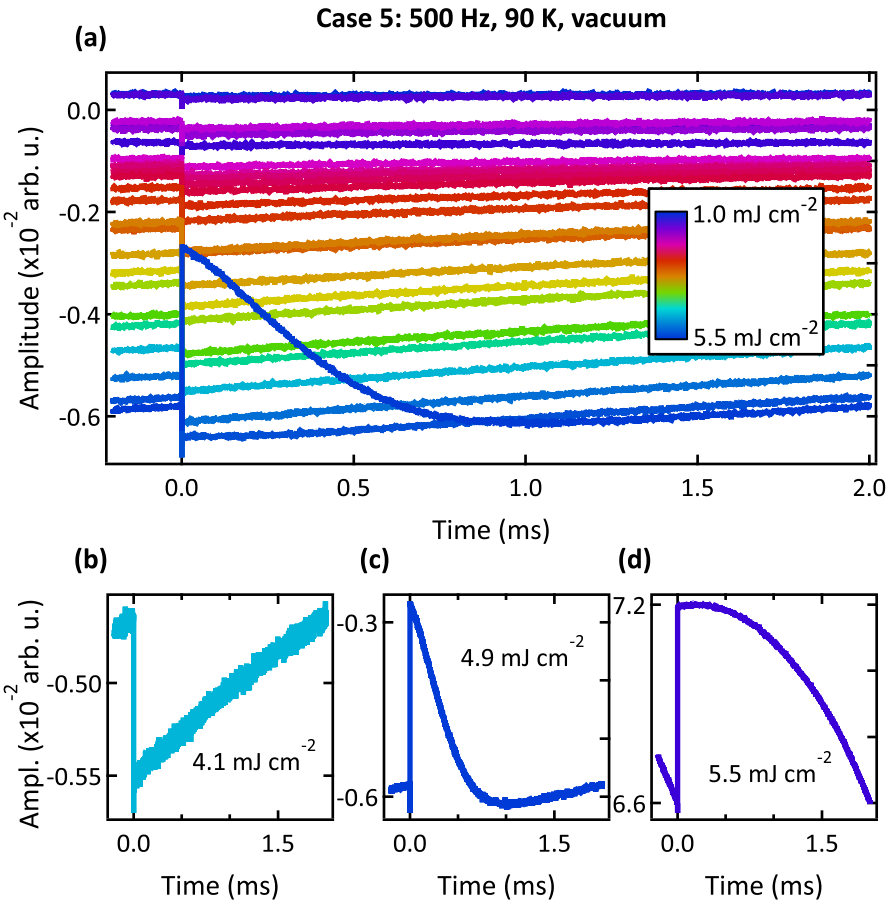

Fig. 3.7: Time traces at 500 Hz repetition rate, 90 K, in vacuum. **(a)** Fluence-dependent recovery of the sample within the 2 ms between pump pulses. Time traces measured after pump excitation in the below-threshold regime in **(b)**, above the threshold fluence in **(c)**, and in the saturation regime in **(d)**.

3.2.1 Threshold fluences comparison

Traditionally, in ultrafast measurements, the threshold fluence for the phase transition in VO_2 has been defined as the value at which the amplitude of the system response at an arbitrary time delay of 1 ps starts to become nonlinear with fluence [48, 54, 56]. Here, an analogous analysis is performed of the fluence-dependent change in transmission to determine the threshold value for the phase transition. In these long-dynamics measurements, the response in the picosecond time scales is not available, though, and is evaluated instead at 1 µs after photoexcitation.

In Fig. 3.8, the response amplitude at 1 µs time delay is displayed as a function of fluence for Cases 1-4 from the previous section. The four traces

share a common behaviour consisting of a linear dependence at low fluences with negative slope, followed by a nonlinear regime where the signal switches to a positive change in transmission. The dashed traces correspond to linear fits of the responses below and above threshold, the intersection of which is defined as the starting point for the phase transition. The values for the fluence thresholds obtained by this method are listed in Table 3.1. Noteworthy, there is a difference of more than 10 mJ cm^{-2} between the measurements performed in vacuum, with a difference in the base sample temperature of 200 K. Interestingly, while above threshold the rate of increase in transmission per fluence unit is of the same order for all the cases, below threshold two different trends can be distinguished. The rate of decrease in transmission per mJ cm^{-2} in the measurements performed at atmospheric pressure is faster than those conducted under vacuum. This points towards different cooling rates for each ambient conditions, and will be further detailed in the following sections.

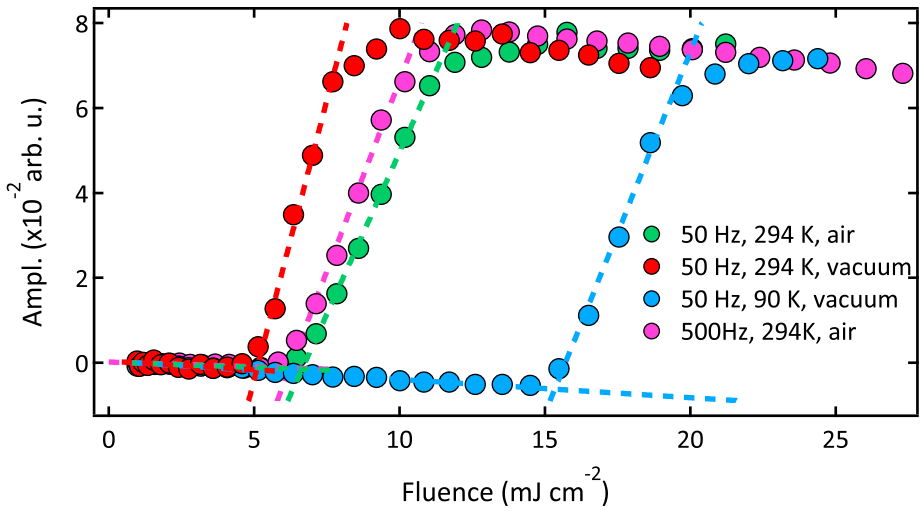

Fig. 3.8: Fluence-dependent transmission change at 1 µs for Cases 1-4.

Case	Below F_{TH} $\Delta I/F$ (x10^{-2})	F_{TH} (mJ cm^{-2})	Above F_{TH} $\Delta I/F$ (x10^{-2})
50 Hz, 294 K, air	-0.026 ± 0.001	6.6	1.52 ± 0.03
50 Hz, 294 K, vac.	-0.04 ± 0.02	5.1	2.5 ± 0.1
50 Hz, 90 K, vac.	-0.042 ± 0.001	15.3	1.7 ± 0.1
500 Hz, 294 K, air	-0.022 ± 0.005	6.2	1.72 ± 0.08

Table 3.1: Fit results from the fluence dependent change in transmission.

3.2.2 Thermal model

As mentioned before, the long time scales dynamics and the experimental results presented above point towards thermal contributions as the main aspects for understanding the observed behaviours. Therefore, with the aim of having a quantitative understanding of the recovery dynamics observed under different experimental conditions, the transmission of the sample upon different excitation densities can be simulated via a temperature-dependent model.

In order to simulate the sample response, the dependence of transmission upon time after photoexcitation is required. As already known and measured, the transmission of VO_2 follows a hysteresis curve with temperature (see Fig. 2.5), which can be mathematically modelled as an error function centred at T_C. On the other hand, the temperature of the system is assumed to follow Newton's law of cooling, in which the temperature rate of change is proportional to the difference between the temperature of the system and its surrounding. This way the dependency of transmission upon time can be calculated. The equation for simulating the change in transmission as a function of temperature is the following:

$$I(T) = A + BT + C\frac{1}{2}\left[\text{erf}\left(\frac{T - T_C}{T_w}\right)\right], \tag{3.1}$$

where the 1/2 factor corresponds to the normalization of the error function of width T_w, the term $A + BT$ accounts for the effect of carrier dynamics in the low-fluence response, that is, at low temperatures before entering the hysteresis loop. The equation for the temperature rate of change as a function of time is split into two regimes that correspond to the insulating and metallic phases, which are assumed to change at $T_C - 2T_w$ (reached at time t'_0), the point where the two hysteresis branches are separated as portions of the sample are

transformed into the metallic phase. The equation for the sample temperature as a function of time results as:

$$T(t) = \begin{cases} T_i + \frac{1}{2}\left(1 + \mathrm{erf}\left(\frac{t-t_0'}{t_r}\right)\right)\Delta T' e^{\frac{t-t_0}{\tau_1}}, & \text{for } t > t_0' \\ T_i + \frac{1}{2}\left(1 + \mathrm{erf}\left(\frac{t-t_0}{t_r}\right)\right)\Delta T e^{\frac{t-t_0}{\tau_2}}, & \text{for } t_0 < t < t_0', \end{cases} \tag{3.2}$$

where T_i is the initial temperature, ΔT is the increase of temperature induced by the pump excitation (from T_i to T_f) at t_0, $\Delta T' = T_C - 2T_w - T_i$ at t_0', the normalized error function is used to model the rising edge of width t_r, and τ_1, τ_2 are the time constants of the cooling rates in the insulating and metallic phases, respectively (the model parameters can be seen in Fig. 3.9). Combining these equations, $I(t)$ can be obtained. Moreover, this model allows the calculation of the temperature rise at negative times delays arising from heat accumulation, if any, when the sample does not fully recover back to the initial temperature.

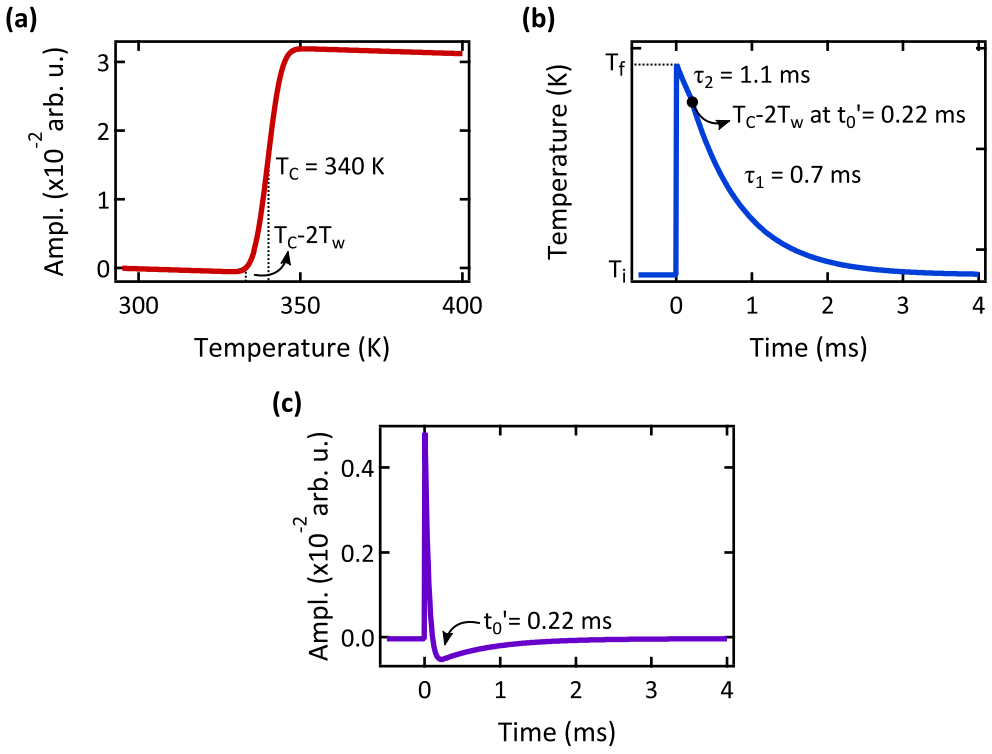

Fig. 3.9: Simulated dynamic response to photo-excitation via a temperature model (a) Simulated transmission as a function of temperature as described by Eq. 3.1. **(b)** Sample temperature as a function of time according to Eq. 3.2. **(c)** Resulting time-dependent transmission through combination of (a) and (b).

As an example, $I(T)$, $T(t)$, and the resulting $I(t)$ are simulated in Fig. 3.9 for excitation just above the threshold fluence. Figure 3.9(a) represents the dependence of change in transmission upon temperature described by Eq. 3.1. The values of $T_C = 340\,K$ and $T_w = 4.6$ are extracted from the sample characterization shown in Fig. 2.5. Figure 3.9(b) displays the temperature as a function of time as interpreted in Eq. 3.2 for an initial increase in temperature of 42 K. And the resulting transmitted intensity as a function of time is represented in Fig. 3.9(c), where the distinct feature observed at t_0' is considered as the time it takes for the system to re-enter into the insulating phase after it has been excited into the metallic phase.

3.2.3 Quantitative results of the recovery dynamics of VO_2

Atmospheric pressure conditions

Figure 3.10 shows the results obtained from the application of the temperature-based recovery model to the temporal response of the sample measured with a repetition rate of 50 Hz at room temperature and atmospheric pressure. An excellent agreement can be found between theoretical and experimental traces. According to this model, the measured threshold fluence of 10.5 mJ cm^{-2} corresponds to excitation of the sample to a temperature of 334.5 K. The largest discrepancies can be found at higher pump fluences, specifically in the temporal width of the response at times $t > t_0'$. The main origin for this lies mostly in the fact that this model does not account for the different paths followed by the sample when heating and cooling caused by the hysteretic nature of VO_2.

The calculated parameters are shown in Fig. 3.11. The temperature reached by the sample presents a linear dependence with fluence at low excitations, up to $T_C - 2T_w$, point at which increasing fractions of the probed volume are transformed into the metallic phase. The temperature increase with fluence is slowed down in this region as part of the absorbed energy accounts for the latent heat of VO_2. The linear behaviour is expected to be back above $T_C + 2T_w$, which lies just at the limit of Fig. 3.11(a). On the other hand, the initial temperature (T_i) remains constant at 295 K, which stands as a clear indication for the complete recovery of the sample for each fluence. In Fig. 3.11(b), the characteristic times of the dynamics are shown. The time constant for the cooling rate for the insulating phase (τ_1) is found to be of 0.61 ms. However, both the onset of the insulating phase, defined as t_0' in the previous section, and the characteristic time of the recovery rate of the above-threshold dynamics (τ_2) are found to increase with higher fluences. This is not surprising

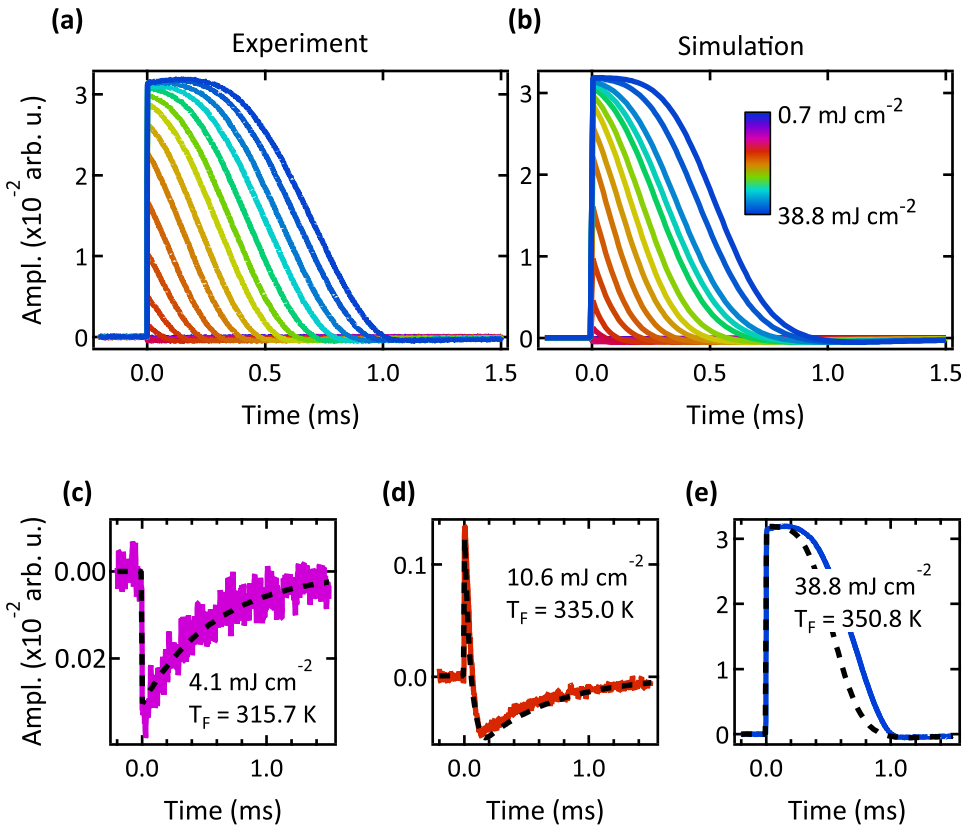

Fig. 3.10: Simulated dynamic response to photoexcitation at 50 Hz, room temperature, and atmospheric pressure. **(a)** Experimental time traces obtained by increasing pump-fluence excitation. **(b)** Theoretical time traces obtained by application of the thermal model. Measured (coloured lines) and simulated (black dashed lines) in the below-threshold regime in **(c)**, above the threshold fluence in **(d)**, and in the saturation regime in **(e)**.

as, within this temperature range, the sample is expected to be formed by a mixture of insulating and metallic domains. At temperatures above $T_c + 2T_w$, τ_2 is stabilized to a value of ≈ 2.5 ms. t_0', on the other hand, keeps growing with increasing fluence, as expected for recovering from higher temperatures.

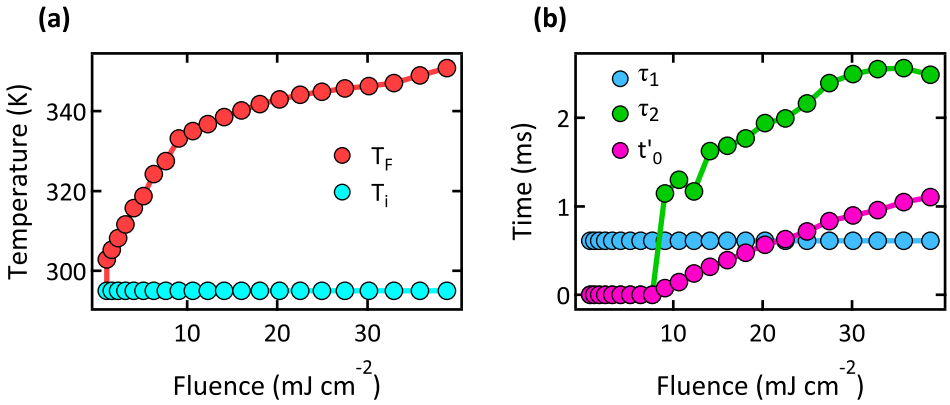

Fig. 3.11: Thermal model parameters for the dynamic response at 50 Hz, room temperature, and atmospheric pressure. **(a)** The maximum attained temperature by the sample upon photoexcitation (T_f) grows with increasing fluence, while the initial temperature (T_i) remains constant at room temperature. **(b)** Characteristic times of the recovery rates in the insulating phase (τ_1), of 0.61 ms, and in the metallic phase (τ_2), stabilized to a value of 2.5 ms. The time it takes for the system to relax back into the insulating phase (t'_0) increases with fluence above the threshold.

Vacuum conditions

An analogous analysis is performed for the dynamics measured with a repetition rate also of 50 Hz, but with the sample held under vacuum conditions at a base temperature of 90 K (Case 3 in Section 3.2). The calculated traces are displayed in Fig. 3.12. Again, a very good agreement between the simulations (dashed lines) and the experimental results is observed, and the threshold fluence measured under these conditions, of 15.3 mJ cm^{-2}, corresponds to excitation to a temperature of 334.5 K, as in the previous case.

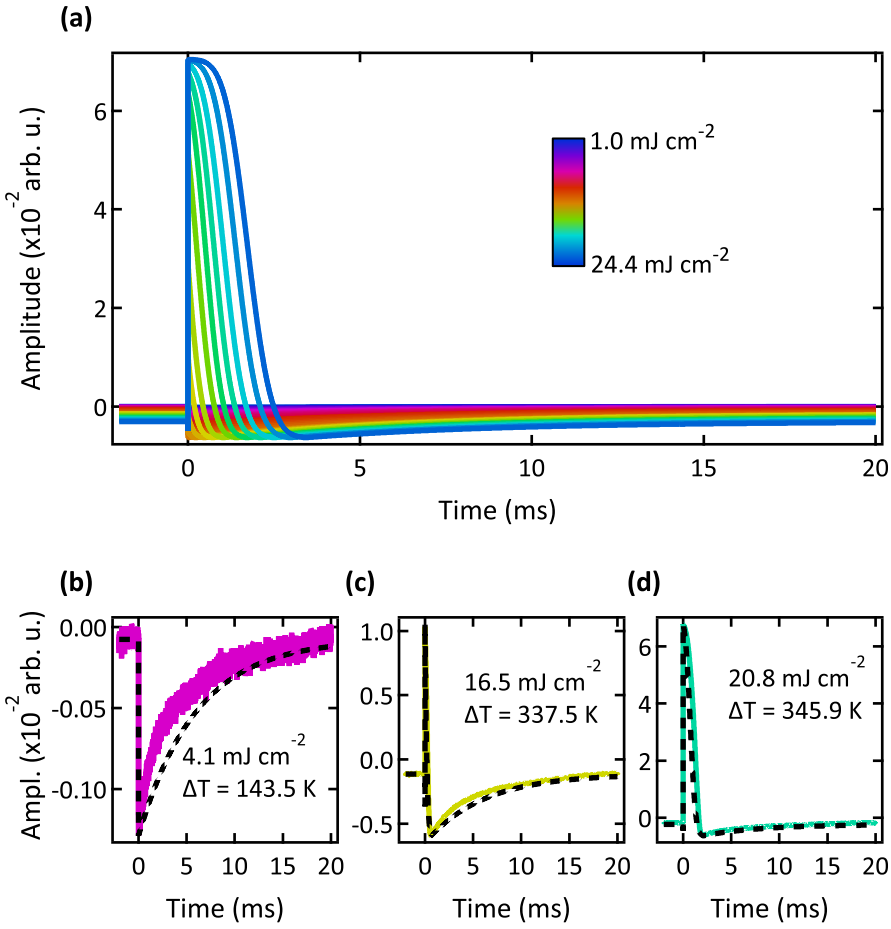

Fig. 3.12: Simulated dynamic response to photoexcitation at 50 Hz, 90 K, and vacuum conditions. (a) Calculated time traces obtained by application of the thermal model. Measured (coloured lines) and simulated (black dashed lines) in the below-threshold regime in **(b)**, above the threshold fluence in **(c)**, and in the saturation regime in **(d)** .

Figure 3.13 shows how ambient conditions lead to significant different results. Whereas the final temperature achieved by the sample at each excitation fluence follows a similar behaviour than in the previous case measured in air, with a linear increase followed by a slower growth above the fluence threshold, the initial temperature does not stay constant at the base 90 K set by the cryostat. As shown in Fig. 3.13, the time constant for relaxation in the insulating phase (τ_1) is found to be of 6 ms, a factor of ≈ 10 slower than at atmospheric pressure conditions, while τ_2 stabilizes to a value of 22 ms in the metallic phase. Such long recovery times within this 20 ms period lead to heat accumulation that results in an increasing temperature rise. Noteworthy, this phenomenon was not apparent when first looking at the measured traces in Fig. 3.5, as compared with the obvious case in Fig. 3.4. However, a careful analysis of the data demonstrates that ultrashort laser pulses can induce a static temperature increase of up to 100 K for an excitation fluence of 24 mJ cm^{-2}.

It is worth noticing that, in a typical pump-probe measurement under these experimental conditions, where the differential signal between the pumped and unpumped sample is measured, this heating effect could be easily overlooked for intermediate fluences, when a partial volume has permanently switched into the metallic phase, as it is only reflected in a decrease in amplitude of the signal.

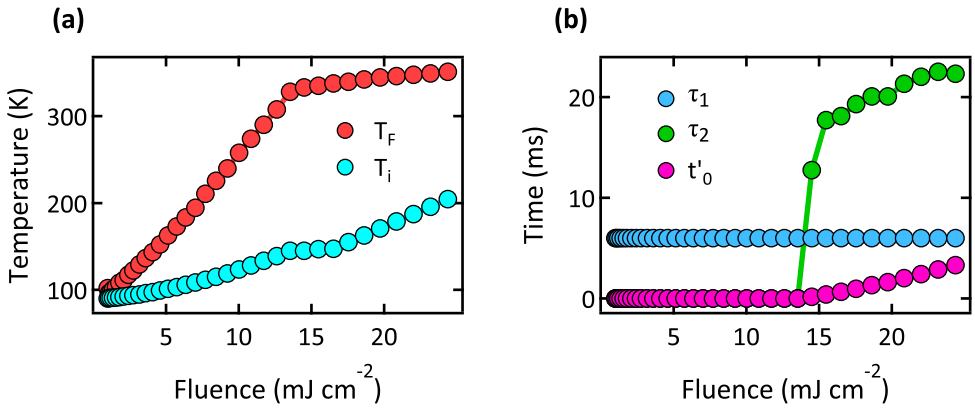

Fig. 3.13: Thermal model parameters for the dynamic response at 50 Hz, 90 K, and vacuum conditions. **(a)** Both the maximum attained temperature by the sample upon photo-excitation (T_f) and the initial temperature (T_i) grow with increasing fluence. **(b)** Characteristic times of the recovery rates in the insulating phase (τ_1), of 6 ms, and in the metallic phase (τ_2), stabilized to a value of 22 ms. The time it takes for the system to relax back into the insulating phase (t'_0) increases linearly with fluence above threshold.

3.2.4 Pump spot-size effect

The measurements presented in cases 1-5 were performed under identical laser conditions, with the exception of the specified changes. It has been shown how different pump repetition rates, ambient pressure conditions and initial temperature, can result in the VO_2 thin film providing a significantly different response for the same excitation density. This is directly related to the heat transfer velocity within the material after a certain amount of energy is deposited by the pump laser pulse. Now, the effect of modifying the pump spot-size area on the resulting temperature change rates is investigated. With that aim, the transmission of the sample is probed immediately after photoexcitation, at a time delay of 1 µs, with Gaussian-shaped pump beams of different area sizes on the film. Both cases shown in Fig. 3.14, at room temperature and 90 K, were measured with two different pump spot-sizes: 93.4 µm × 85.1 µm and 289.2 µm × 261.9 µm, which result in excited areas on the sample of 0.006 mm and 0.059 mm, respectively. This factor of ≈ 9.5 is reflected in the fluence dependence of the transmission change after photoexcitation. In Figs. 3.14(a)

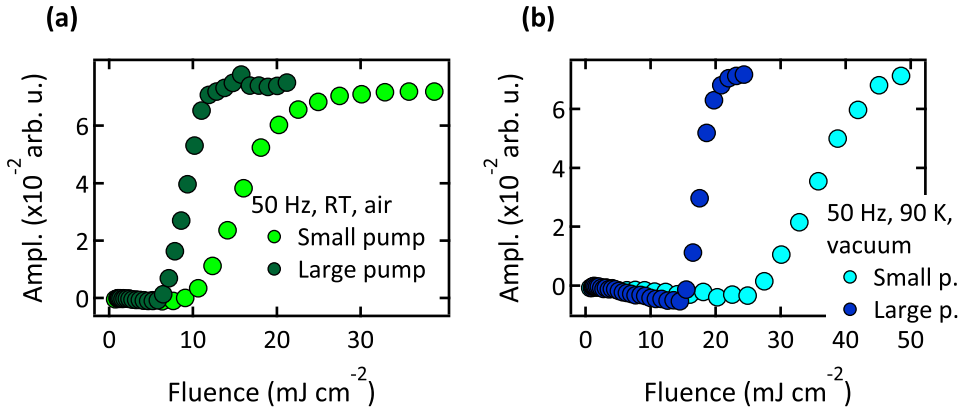

Fig. 3.14: Comparison of the fluence-dependent transmission change at 1 µs after excitation with pump pulses of different spot-sizes. Both under atmospheric pressure **(a)** and vacuum conditions **(b)**, for a smaller pump spot-size, higher fluences are required for triggering the phase transition.

and 3.14(b), it can be seen how the threshold is shifted towards higher fluences for the smaller pump spots, with a value of 10.5 mJ cm^{-2} and 26.4 mJ cm^{-2} for air and vacuum conditions, respectively. This effect can be understood by considering that cooling rates in the sample are dictated by the temperature gradient generated in the film upon photoexcitation. Given the sub-100-nm sample thickness, heat transport can only occur in the transverse direction. Therefore, larger spot-sizes lead to smaller temperature gradients and longer

cooling times. As a result, a smaller increase of fluence is necessary to achieve the same temperature rise.

Here, the theoretical temperature model is applied to these results. The respective comparison is represented in Fig. 3.15. Consistently with what seen for the fluence-dependent transmission, where it was shown how larger spot-sizes result in lower threshold fluence values, in Fig. 3.15(a) the dependence of the maximum attained temperature upon excitation density increases in a slower fashion when the spot-size is smaller. Therefore, the characteristic times for the relaxation dynamics (Fig. 3.15(b)) are not the same for every fluence.

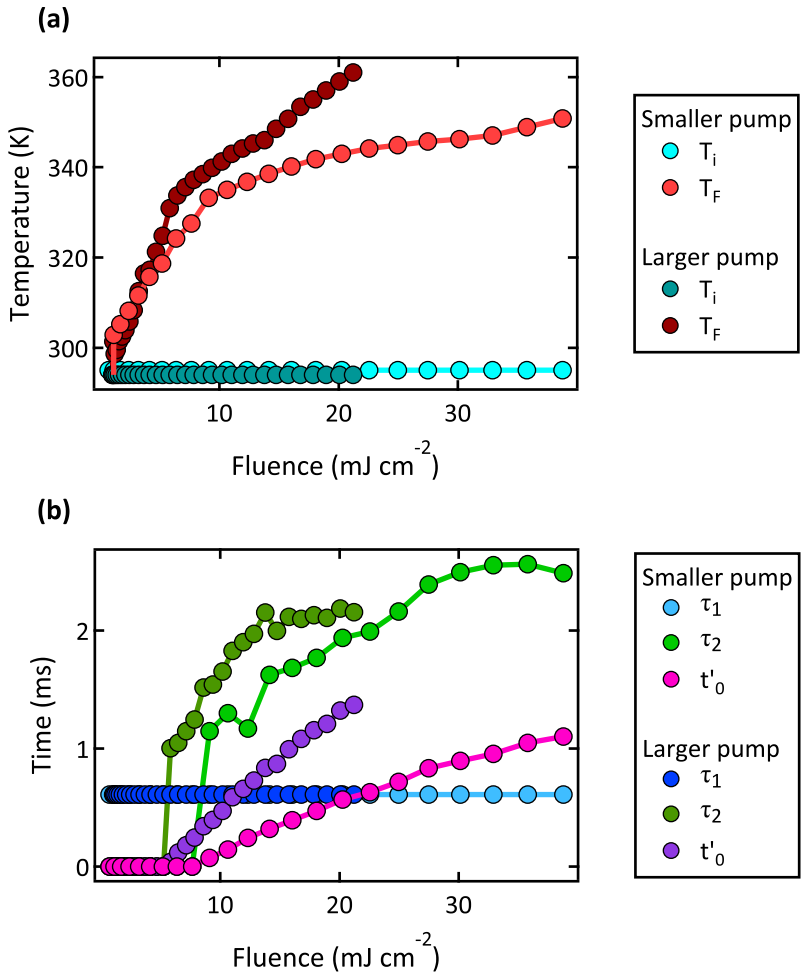

Fig. 3.15: Comparison of the thermal model parameters for excitations with different pump spot-sizes. (a) While in both cases the initial temperature (T_i) remains constant at room temperature, T_f exhibits a slower increase with fluence for excitation with a smaller spot-size. **(b)** Characteristic times of the recovery rates in the insulating phase (τ_1) and in the metallic phase (τ_2).

Case	F_{TH} (mJ cm^{-2})	T_{TH} (K)	τ_1 (ms)
50 Hz, 294 K, air	6.6	334	0.65
50 Hz, 294 K, vac.	5.1	335	6
50 Hz, 90 K, vac.	15.3	334.5	6
500 Hz, 294 K, air	6.2	-	-
50 Hz, 295 K, air (9x smaller pump)	10.5	334.5	0.61

Table 3.2: Correspondence of threshold fluence and temperature. While the required fluences are not the same for triggering the phase transition under different experimental conditions, the threshold temperature do coincide.

3.2.5 Discussion

Table 3.2 summarizes the threshold fluences measured within the different experimental cases. As it can be seen, they strongly depend on experimental factors, such as the ambient conditions (atmospheric pressure or vacuum), pump laser repetition rate, base temperature, and even the pump spot-size on the sample. Nonetheless, when simulating the dynamics with a simple temperature-based model, it is encountered that all the values correspond to excitation to a temperature in the range of 334–335 K. This value is lower than the defined T_C (of 340 K for this sample), but it corresponds to the beginning of the hysteresis behaviour of the transmission upon temperature, where the heating and cooling branches have split and fractions of the sample have already started to switch into the metallic phase. On the other hand, in a high-quality single crystal with a characteristic sharper transition, the threshold fluence is expected to coincide with T_C.

The results presented here display a good agreement between the recovery dynamics of the photo-induced phase transition in VO_2 and those simulated by a solely thermal model. This way, the temperature-dependent fluence threshold is merely the consequence of requiring a larger amount of energy to be absorbed for reaching the temperature of $\approx$334 K, rather than for achieving a critical carrier density for collapsing the band-gap, as hole photodoping should not depend on the base temperature of the material. Furthermore, in view of these new results, the divergence from thermal predictions reported at low temperatures in [101], in which the transition could be triggered by lower fluences than the corresponding to the difference in thermodynamic energies, may have a simpler explanation. Considering this experiment was conducted

on a thin film under vacuum conditions, the observed effect could arise from heat-accumulation that had already raised the temperature of the sample from its initial base.

The thermodynamic energy required for inducing the phase transition in VO_2 is given by the expression $E_{TH} = C_v \Delta T + H_L$, where C_v and H_L are the heat capacity and latent heat, respectively. Assuming that in the photo-induced phase transition all the absorbed pump-pulse energy is transformed into heat, the minimum incident fluence for thermally inducing the metallic state can be calculated with $F_{TH} = E_{TH} d/(1 - R)$, where d is the sample thickness (since it is thinner than the penetration depth), and R, the reflectivity of VO_2 at 800 nm (of 0.28). With a latent heat of $235\,\mathrm{J\,cm^{-3}}$ [102] and integrating the heat capacity over the desired temperature range [102], the optical thresholds for inducing the transition are calculated to be $\approx 4\,\mathrm{mJ\,cm^{-2}}$ and $\approx 8.5\,\mathrm{mJ\,cm^{-2}}$, for base temperatures of 295 K and 90 K, respectively.

The values measured here for the photo-induced transition are somewhat higher than these, an effect that might be related to superheating phenomena found to occur in many first-order phase transitions. It should be noted as well, though, that the thresholds measured at microsecond time-scales are expected to be generally higher than those obtained when measuring the response of VO_2 to photo-excitation within the picosecond regime, as volume expansion processes have an effect on the dynamics. This simple calculation represents a lower limit for the energy required for driving the transition, as many factors are neglected, in particular those specific to the employed sample. However, in none of the cases measured here the transition is photo-induced by exciting the sample with a *lower* fluence than that required by thermodynamics.

The strong dependency of the threshold fluence on experimental parameters hinders the utility this value can have for characterizing the phase transition process. It is important to notice that, despite these measurements being carried out in the millisecond regime, the fact that the system does not recover fast enough has a major effect also on femtosecond time-scales as a result from the repetitive nature of pump-probe measurements. As a final step in the investigation of threshold fluences, motivated by the claim that probing the photo-induced phase transition with different wavelengths leads to distinct thresholds, the fluence-dependent transmission of a thin film of VO_2 is measured after photoexcitation employing photon energies in the visible and mid-infrared regime.

3.3 Threshold-fluence measurements in the visible-MIR regime

In the experiments performed by Morrison *et al.* mentioned at the beginning of this chapter, 5-µm-wavelength laser pulses were employed to probe the electronic band-gap, which was found to collapse without the need of a structural distortion [51]. This claim was based on the fact that the threshold value for the closing of the band-gap was lower than that found by means of the structural probe provided by electron diffraction. Nonetheless, in light of the new information presented so far regarding the dependence of threshold fluences on so many external parameters, such important claim is now tested.

The photo-induced phase transition is probed here with a selection of photon energies that lie both below and above the band-gap of VO_2 ($\approx 0.6\,\text{eV}$). Whereas the shorter wavelengths are mainly sensitive to changes in the density of states above the insulating gap, and the regime around 800 nm has been shown to probe the structure through phonons measurements, the signal provided by energies well below the band-gap, such as 5 µm, are expected to probe the emergence of metallic-like conductivity from the intragap electronic states. The observed suppression of transmission at these lower photon energies immediately after strong photo-excitation has been taken as indication for the closure of the band-gap and the onset of a Drude-like response of free electrons in metallic VO_2 [48, 51, 100].

The pump-probe measurements presented here were performed by exciting the thin film of VO_2 with an 800 nm pump laser at a repetition rate of 100 Hz and probed with laser pulses of different wavelengths ranging from the visible to the mid infrared regime generated by difference frequency generation from the signal and idler beams of an IR optical parametric amplifier (OPA) (see Fig. 3.16). The sample was held at room temperature under atmospheric pressure conditions. The transmitted intensity was recorded by a photo-diode connected to the same oscilloscope as in the previous experiment. Additionally, the response of the sample was tested under these experimental conditions to check for a complete recovery between laser pulses.

It is worth mentioning that fluence determination is always accompanied by experimental uncertainties, mostly arising from small errors in spot-size measurements, losses in absorption/reflection at different angles of incidence, and sample inhomogeneities. Moreover, as seen in previous sections, experimental parameters may have major effects on the thresholds observed for the phase transition. Therefore, the importance of these results does not focus

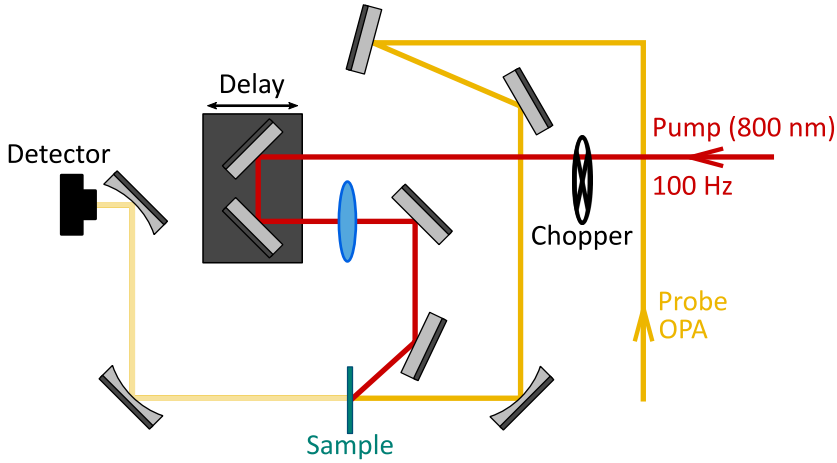

Fig. 3.16: MIR pump-probe experimental setup. The sample is excited with 800 nm pump pulses at 100 Hz and probed with wavelengths generated by an OPA, in the mid infrared and visible regime.

on the absolute values obtained, but on the relative differences between four measurements performed in the same experimental setup under the same conditions. Additional measures were taken to ensure that every probe deposited the minimum and equal power on the sample, as due to the nature of the frequency conversion processes, its efficiency is highly wavelength dependent, which results in different wavelengths having different intensities. This step is vital, as probe pulses can also act as a heating source in the same way the pump does, especially since they are typically focused to a much smaller spot-size.

Figure 3.17 displays the fluence-dependent differential transmission measured at 1 ps after photo-excitation employing the following wavelengths: 680 nm (1.82 eV), 1.375 µm (0.90 eV), 1.890 µm (0.66 eV), and 5 µm (0.25 eV). As performed for the fluence scans displayed in Fig. 3.8, the threshold values are defined as the intersection of the linear fits represented by the dashed lines for each wavelength. The results are collected in Table 3.3. As observed, all the values obtained lie within the range of 4.0–4.6 mJ cm^{-2}.

No significant differences can be observed neither in the fluence-dependent transmission behaviour, nor in the obtained threshold fluences. No evidence for the emergence of a metallic state at lower fluences can be extracted from these results and hence the claim for decoupled electronic and structural transitions have no support from this experiment. Instead, a single threshold value is found to describe the photo-induced phase transition in VO_2, which is assigned to the M_1-R transition.

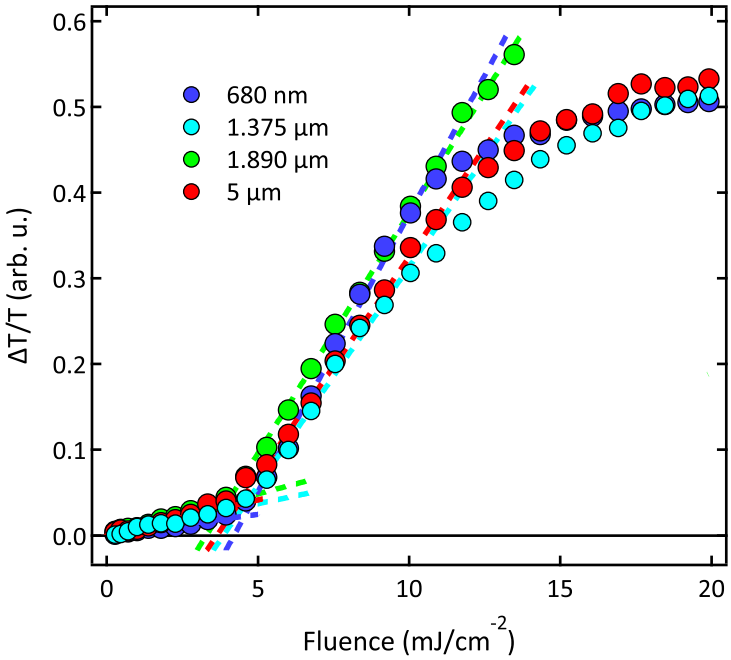

Fig. 3.17: Fluence-dependent transmission change at 1 ps in the visible-MIR regime. .

λ (µm)	F_{TH}
0.680	4.6
1.375	4.5
1.890	4.0
5	4.4

Table 3.3: Threshold fluences in the visible-MIR regime. Values of the threshold fluence of the photo-induced phase transition obtained by probing with different wavelengths.

3.4 Conclusions

This chapter has shown that the slow recovery dynamics of VO_2 are vital for the correct interpretation of threshold measurements, not only on the long time-scales measured here, but also on the femtosecond regime, as a result from the repetitive nature of pump-probe measurements. Heat buildup effects are of particular importance in experiments performed on free-standing thin films, where the lack of material that can act as a heat sink limits the rate of thermal diffusion. It is important to note, though, that the experimentally crucial quantities, such as the time it takes for the system to return to equilibrium conditions after excitation, are connected to the extrinsic properties of the experiment, rather than to intrinsic properties of VO_2. As a result, the recovery times of the investigated material should always be verified before conducting the final measurements.

On the other hand, from the physics perspective, this study has demonstrated that a simple thermal model is able to accurately reproduce the experimental observations on the recovery dynamics of VO_2. The agreement between experimental results and simulations is striking considering that the behaviour within the hysteresis region, which is non-trivial, is not included in the model. This further reinforces the existence of a common pathway for the thermal and photo-induced phase transitions.

The strong dependency of the threshold energy densities on experimental parameters and ambient conditions makes difficult the comparison of threshold values obtained from different measurements. Despite being reported in literature, laser-induced heating has mostly been neglected. While several experiments have considered heat buildup from the use of high laser repetition rates, the effect of pump spot-sizes, or working under vacuum or atmospheric pressure conditions has been generally ignored. As a result, it is highly probable that the reported discrepancies on VO_2 from the past years arise from such wrong practice when interpreting the threshold values of the transition. Moreover, in this chapter it has been shown that when performing pump-probe measurements employing different probe wavelengths but with a maximum control over external parameters, the differences between thresholds are vanished.

Interestingly, the results obtained by Morrison *et al.*, in which they claim the existence of a monoclinic metallic state, were based on the comparison of threshold fluences measured with ultrafast electron diffraction, sensitive to structural changes, and with a 5 µm probe, sensitive to the band-gap. However, UED was conducted in vacuum while the IR experiment was carried out at

atmospheric conditions. The work presented in this chapter demonstrates, though, that changing the ambient conditions of the experiment can lead to significant different results due to the 10 times lower recovery rate for the thin-film samples under vacuum. As a result, despite not being obvious in the measured dynamics, heat buildup and the consequent temperature rise can be significant high, making seriously difficult the direct comparison of fluence values from both data sets.

As a natural conclusion from the results presented in this chapter, the measurement of threshold values should not be employed as evidence for claims on the nature of the phase transition in VO_2, or any materials presenting a first-order photo-induced transformation. While these concerns are particularly significant for free-standing thin films, they are minor for single crystals, in which their bulky nature is expected to provide a sufficient heat sink. Yet, the recovery of thin films on substrates should still be considered, as thermal flow between sample and substrate may limit heat dissipation.

4 | Structural dynamics across the phase transition

This chapter presents time-resolved measurements of the insulator-metal phase transition of VO_2 in the soft and hard X-ray regimes with the aim of studying the role played by phonon dynamics in the transformation. Section 4.1 summarizes the key results published in literature on the structural transition of VO_2. Sections 4.2 and 4.3 present the results obtained by means of time-resolved soft X-ray absorption spectroscopy and ultrafast X-ray total scattering, respectively. The insight on lattice dynamics across the IMT obtained from both techniques provide a new description of the phase transition. The chapter ends with conclusions in Section 4.4.

4.1 Introduction

The exact role played by lattice dynamics in the ultrafast insulator-metal phase transition in VO_2 is currently still under debate. On one hand, phonon interactions are regarded as the main force that drives the transformation in a Peierls-mediated scenario. On the other hand, the lattice distortion is conceived as a side effect, consequence of the charge redistribution resulting from strong Coulomb forces acting within a Mott-physics picture. The main responsible mechanism may be reflected in discernible differences in the dynamics of the phase transition. In this regard, Cavalleri and co-workers suggested that by watching the transition directly, the nature of the driving mechanism could be revealed [46].

Generally, solid-solid crystallographic transitions where the system undergoes a symmetry change are characterized by a more symmetric high-temperature phase with respect to the low-temperature phase. Furthermore, the low-symmetry phase can be obtained from the high-symmetry phase by distorting the crystal structure along specific phonon coordinates at a particular wavevector. Such is the case in VO_2, with the rutile phase displaying a greater symmetry than the M_1 structure, and the phase transition expressed by modes at the R-point of the rutile structure [103]. To date, the ultrafast phase transition has been assumed to be displacive along this specific phonon coordinate. However, more recently, an alternative transformation pathway, resulting from disorder, has been suggested based on equilibrium measurements [104]. Understanding the type of transformation followed represents a key factor for the complete comprehension of the properties exhibited by the material, and opens up new directions for the efficient control of them.

In a displacive phase transition, the frequency of a specific phonon mode continuously decreases as the phase transition is approached, known as *phonon softening*, until the frequency reaches a zero value at T_c. A zero-frequency phonon implies an unstable lattice structure. A new mode hardens again below the phase transition as the system finds the new, displaced, equilibrium positions of the lower-symmetry phase. During this process, the atoms are shifted in a coherent motion following the soft vibrational mode that links the low- and high-symmetry structures. In contrast, in an order-disorder transition, the atoms move from one structure to the other in an incoherent way with no well-defined wave vector to conduct the transformation. Instead, diverse pathways can be followed by the atoms, to arrive to the same final destination. In this case, no phonon softening at any wavevector characterizes the phase transition. Notably, in both processes the average atomic positions may follow

a trajectory along the same coordinate between both symmetries, as illustrated in Fig. 4.1.

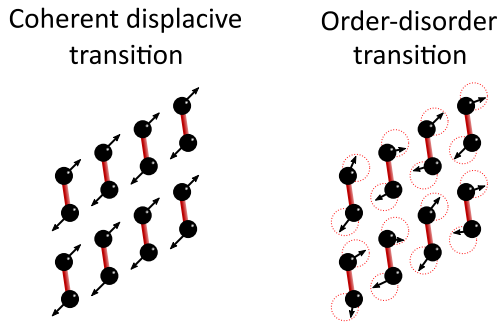

Fig. 4.1: Transition mechanisms between the M_1 and R phases of VO_2 upon photoexcitation. In a coherent displacive transition, the V ions collaboratively reshuffle their positions along the reaction coordinate towards the rutile structure. The disordering mechanism has no well-defined wavevector, and the V ions move towards the high-symmetry structure in a spatially incoherent fashion.

Initial symmetry analysis of the metallic rutile phase of VO_2 suggested that the crystallographic phase transition could be explained in terms of a phonon at the Brillouin-zone boundary, specifically at the rutile R-point, that softens on cooling towards the phase transition within a displacive process [103, 105, 106]. Rutile zone-boundary R-points are equivalent to zone-center Γ-points of the monoclinic phase. Therefore, the modes relevant to the structural transition belong to a low-energy optical branch of the M_1 phase that becomes a transverse acoustic branch in the rutile structure. Specifically, the phonons of the insulating phase often ascribed to the dimerization and rotation of the vanadium atoms are A_g modes at ~ 5.9 THz and ~ 6.7 THz, which soften significantly, in the high-temperature phase, to frequencies in the 2–4 THz range [46]. In order to measure the modes away from the Brillouin-zone center, probes with finite momentum are necessary.

Traditionally, the most powerful method for this has been inelastic neutron scattering (INS), which allows the study of lattice dynamics through phonon dispersion in several crystals. However, due to the extremely large incoherent cross-section of neutron scattering for vanadium, large single-crystals are required. The difficulty in growing sufficiently wide crystals, together with the tendency of such crystals to fracture across the phase transition, has made of INS a very challenging technique for studying VO_2. As a result, for many years the comprehension of lattice dynamics has relied mainly on Raman spectroscopy [107, 108], together with other indirect approaches able to probe

the evolution of phonons across the IMT, such as acoustic waves measurements [109]. These early measurements reported very different spectra for the monoclinic and rutile structures of VO_2. While the low-temperature phase appears to be characterized by sharp peaks at distinct phonon frequencies, the high-temperature phase consists of a broad frequency band [107, 108, 110]. This broadening stands as a signature of the heavy damping of phonons, which was attributed to strong electron-phonon coupling in the metallic phase that reduces phonon lifetime [107].

To overcome the limitations of Raman measurements and optical probes in general, only sensitive to modes at the Γ-point, a different approach was adopted, which exploited the larger penetration depth and higher photon momentum of hard X-rays to measure thermal diffuse scattering (TDS) [110]. The presumed softening of the R-point rutile phonon modes should give rise to an enhanced diffuse scattering across the corresponding regions of reciprocal-space. This experiment provided the first experimental observations compatible with such a phonon softening. The evidence was, though, hindered by the poor data quality from that time.

As a result, the VO_2 phase transition, as well as most ultrafast solid-solid transitions, has been generally considered as a chemical reaction, in which the system evolves along a reaction coordinate that links the two structures, corresponding to the wavevector of the rutile soft phonons. More recently, time-resolved studies of the structural transition based on ultrafast electron and X-ray diffraction gave support to the displacive description of the phase transition [45, 51, 56]. The coordinated atomic motion along a well-defined wavevector was found to limit the speed of the photo-induced transition leading to the so-called structural bottleneck [46], introduced in Section 1.3.

Until recently, mapping the entire phonon dispersions across the Brillouin zone had remained an unsolved challenge. But in 2014 a new experiment conducted by Budai *et al.* shed light into this issue. By combining inelastic X-ray and neutron scattering on small single-crystals and powder samples, respectively, they achieved the first detailed picture of the lattice dynamics over a wide $\boldsymbol{q}$-region across the phase transition in VO_2, supported by first-principles DFT-based phonon simulations [104]. This study showed how the structural transition is accompanied by large changes in the phonon spectrum over extended regions of the $\boldsymbol{q}$-space. In particular, the modes of the monoclinic optical branches appear to soften abruptly when transforming into the rutile acoustic branches, with an energy drop from ~ 25 meV to ~ 12 meV. The lattice potential in the high-temperature phase was found to be largely anharmonic, leading to a great increase of phonon entropy in the metallic phase.

Calculations concluded that phonons account for approximately two thirds of the total entropy raise across the transition from M_1 to R that eventually stabilizes the metallic phase. Notably, no zero-frequency modes were found at the R-point across the phase transition, disproving previous suggestions of a soft-mode transition at this wavevector [106, 110].

These recent results confirm early proposals about high phonon entropy responsible for stabilizing the metallic phase [111]. Considering phase stability as achieved by minimizing the Gibbs free energy, within this thermodynamic description, the phase transition results from the competition between minimizing the electronic energy in M_1 by V-V dimerization, and maximizing the entropy arising from soft anharmonic phonons in the metallic phase. Furthermore, the absence of phonon condensation close to T_c and the abrupt softening point towards an order-disorder type of transition, rather than a displacive process as generally believed.

As well as changing the existing view of the equilibrium phase transition, this work also challenges the current interpretation of the ultrafast transition. If there is not one specific mode responsible for the phase transition, it is hard to argue that it should proceed at a defined structural bottleneck time scale. However, it is also not obviously clear what limits the time scales when the transition is driven by disorder. Therefore, the fast electronic time scales reported by some previous studies could still be the result from lattice dynamics.

In order to shed light on the role played by phonon dynamics in the photo-induced insulator-metal phase transition in VO_2, the lattice evolution across the IMT is probed employing different methods. First, changes in the crystal field upon photoexcitation within the monoclinic and rutile structures are studied by means of time-resolved soft X-ray absorption spectroscopy within picosecond time scales. For deeper insight into the dynamics, these results are combined with femtosecond optical spectroscopy and coherent phonon generation, capable of probing phonons response near the Brillouin-zone centre with sub-50-fs temporal resolution. Finally, through an ultrafast hard X-ray diffuse scattering technique, femtosecond phonon dynamics over extended $\boldsymbol{q}$-regions of reciprocal space are investigated, providing the first measurements on the momentum-dependent phonon spectrum changes across the phase transition.

4.2 Time-resolved X-ray absorption spectroscopy

As presented in Section 2.2.2, XAS is a particularly useful technique for studying the insulator-metal phase transition in VO_2, as it is both sensitive to electronic and structural degrees of freedom, and is element specific. Extending this technique to the time domain can thus give insight into the evolution of these features across the IMT. Specifically, the XAS signal results from transitions from localized core states (initial states) into unoccupied levels of the conduction band (final states). In general, a time-resolved XAS signal can result from transient changes in either the initial or the final states, or both. Yet, in the soft X-ray region, where this work is carried out, the picture is simplified by the existence of large screening in the core states, so that changes in these initial states caused by photo-excitation or phase transitions are minimal, and any measured signal can be attributed to modifications of the final states alone. This is not the case, though, for measurements performed with lower-energy photons, such as XUV and optical frequencies, which gives soft XAS a distinct advantage over other techniques.

With regard to the final states, two phenomena can drive changes in them. Firstly, a redistribution of the electronic population within an unmodified band structure may block transitions into previously unoccupied states, or allow transitions into previously occupied ones. In the XAS signal, this results in changes predominantly affecting the spectral region that probes states near the Fermi energy. Alternatively, final states can be altered by changes in the band structure or crystal field, which can modify the distribution and density of the unoccupied states. This may not result in localized spectral changes in the XAS signal, but in broader modifications. Therefore, XAS spectra can probe both electron and state dynamics.

The first time-resolved XAS experiments on VO_2 were conducted by Cavalleri *et al.*, first on the picosecond [98] and later on femtosecond time scales [112], along the vanadium L- and oxygen K-edges with approximately 4 eV spectral resolution. The range of probed photon energies was therefore limited, which is of particular concern given that the relevant XAS features, that show changes across the IMT, are typically 1 eV wide. To date, further time-resolved studies in this important spectral region have not been performed.

The aim of this study is to probe the evolution of these XAS features across the photo-induced insulator-metal phase transition. The work is focused on the absorption features at the oxygen K-edge, as these have been proven essential for obtaining information about various aspects of the phase transition of VO_2,

such as the role of electronic correlations [44, 83], the existence of a monoclinic metallic state [25], the presence of other insulating phases [93], and to image phase separation with high spatial resolution, as performed in Chapter 2.

4.2.1 Experimental details

The time-resolved XAS measurements were carried out at the FemtoSpeX facility (UE56/1 ZPM beamline) of the BESSY II synchrotron radiation source [113, 114]. The employed samples, 75-nm-thick polycrystalline VO_2 thin films deposited onto 150-nm-thick free-standing Si_3N_4 membranes by PLD, have the same characteristics as those utilized in the holography experiments presented in Chapter 2 (see 2.3.2). During the experiments, the films were maintained under ultra-high vacuum conditions. Laser pulses of 50 fs duration and 800 nm central wavelength excited the sample, and soft X-rays from the isolated hybrid bunch in the normal multi-bunch pattern were gated to probe the response of the sample in transmission. The achieved temporal and spectral resolution were of ~ 75 ps and ~ 1 eV, respectively. At this beamline, the monochromator is optimized for the best compromise between flux and resolution of the X-ray pulses, hence the high spectral bandwidth.

High-resolution spectra measured at low and high temperatures obtained at the UE52-SGM beamline are displayed in Fig. 4.2(a). The relevant XAS features are clearly visible, with the small red-shift in the metallic phase of the π^* states probed at 529 eV, and the presence of an extra peak at 530.5 eV due to the split of the $d_{||}$ band (detailed description of the XAS features can be found in Section 2.2.2). Such features are washed out in the spectra measured at the FemtoSpex beamline due to the lower spectral resolution, as seen in the dashed trace in Fig. 4.2(b). A good agreement between both measurements can be found when comparing the low-resolution with the high-resolution spectra after convolution with a Gaussian function of 1 eV width. The small discrepancies observed are related to the fact that the FemtoSpeX facility is not optimized for static spectral measurements and can be more affected by background drifts. Despite the relatively low energy resolution, the two major absorption peaks can still be distinguished, and these spectra represent a factor of four improvement over previous time-resolved XAS [98, 112].

As shown in Chapter 3, heat accumulation can become significant when measuring free-standing thin-films under vacuum conditions, as the recovery of the sample between pump laser pulses is severely limited. Therefore, it is not possible to work at the usual repetition rate of 3 kHz of the FemtoSpeX facility. According to results presented in 3.2.3, an ideal measurement setup

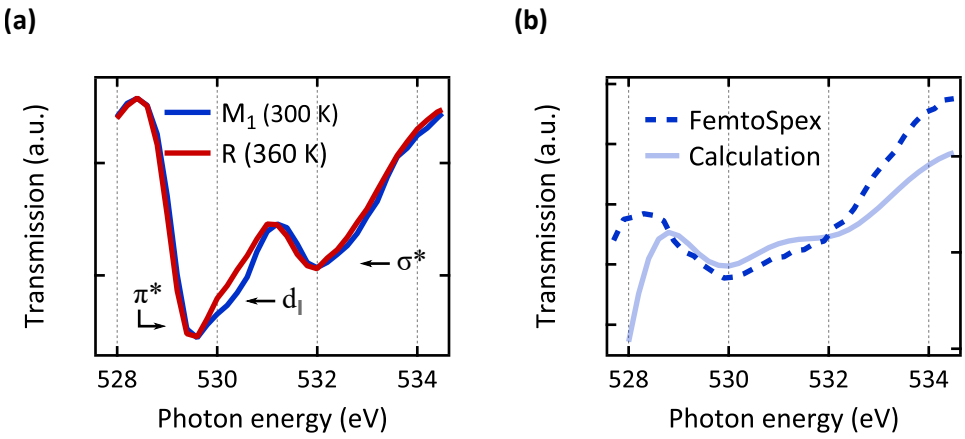

Fig. 4.2: X-ray transmission spectra of VO_2 at the O *K*-edge. **(a)** The high spectral resolution of 0.1 eV of the spectra obtained at beamline UE52-SGM allow for the clear distinction of the π^*, $d_{\|}$, and σ^* states. **(b)** The low-temperature spectrum with 1 eV resolution measured at the FemtoSpeX beamline is in good agreement with the M_1 trace in **(a)** after convolution with a 1-eV-width Gaussian function.

would require laser repetition rates of less than 50 Hz for a complete recovery of the sample at room temperature under vacuum conditions. However, this was not feasible at the FemtoSpeX facility because low repetition-rates have a very strong impact on the signal-to-noise ratio of the experiment, and the active beam stabilization of the pump laser required a minimum repetition rate of 600 Hz. Therefore, as a compromise, the pump laser repetition-rate was set to $R_{\mathrm{L}} = 600\,\mathrm{Hz}$, with the additional cooling down of the sample to a temperature of 90 K, which limits the induced temperature rise.

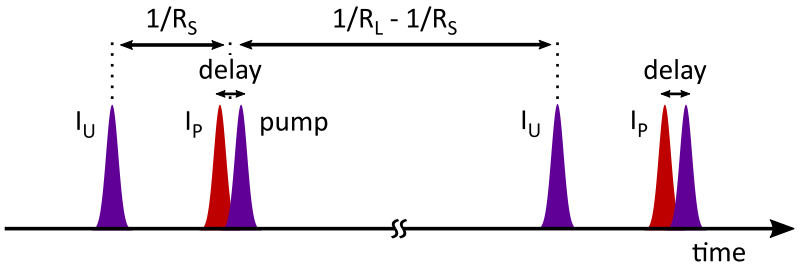

Fig. 4.3: Timings of the *pumped* and *unpumped* probe signals. While all the X-ray pulses from the bunch pattern impinge on the sample, only those labelled as I_{P} and I_{U} are detected within the pump-probe measurements to be afterwards compared to each other.

At this reduced pump frequency, the collected data suffers from much lower statistics. With the aim of improving the signal-to-noise ratio of the experiment by reducing noise from slow drifts and fluctuations in the detection,

extra measures were taken in the data acquisition process. Two X-ray pulses from the pulse train were used to probe the sample, giving rise to the *pumped* and *unpumped* signals. At this beamline, the pump laser is synchronized to a fraction of the repetition-rate of the synchrotron light source, which is $R_S = 1.25\,\text{MHz}$. In the following, the pumped signal, I_P, corresponds to the X-ray pulses that are timed with respect to the laser pulse, in the sense that the pump arrives to the sample at a controllable temporal delay within a window of $\pm\,1\,\text{ns}$ of the X-ray probe (see Fig. 4.3). On the other hand, the unpumped signal, I_U, corresponds to the detected X-ray pulse that arrives at a time $1/R_L - 1/R_S \simeq 1.666\,\text{ms}$ after the previous pump pulse, or 800 ns before the next. The transmission from these two X-ray pulses, I_P and I_U, is recorded by means of gated detection. 1.666 ms corresponds, then, to the maximum possible delay between pump and probe, which, in the ideal case, results in the unpumped channel probing the same state as that found when the laser is blocked. By doing so, any long-lived effects that could exist in the sample, in particular as a consequence of heat, are probed by the unpumped channel, which detects the new steady state of the sample immediately prior to the next excitation pulse.

4.2.2 Transient XAS spectra

Different transient signals were observed in the XAS spectra when exciting the sample with increasing pump fluences. In the following, the spectra are displayed in the differential form of transmission, i.e., $\Delta T/T = (I_P - I_U)/I_U$, to better reflect the change in the sample before and after excitation. Figure 4.4 shows the transient differential spectra measured within a pump fluence range of 1–18 $\text{mJ}\,\text{cm}^{-2}$. It can be seen that the largest changes occur at two different photon energies: 529 eV and 530.5 eV, with negative and positive changes, respectively, in comparison to the ground unpumped state. Recalling Chapter 2, these energies probe transitions into the π^* and $d_{\parallel}$ bands. The dependency of these states upon pump excitation is displayed in Fig. 4.5, where it is clear how both states start to change concomitantly above a threshold fluence of $3\,\text{mJ}\,\text{cm}^{-2}$, and the signals increase in amplitude up to $4.4\,\text{mJ}\,\text{cm}^{-2}$. After this point, they begin to decrease until no transient change is observed at $5\,\text{mJ}\,\text{cm}^{-2}$. Interestingly, raising the pump excitation above this level results in a different change of the XAS spectra, which show a signal at 530.5 eV that gradually increases in amplitude with opposite sign with respect to the low-fluence signal.

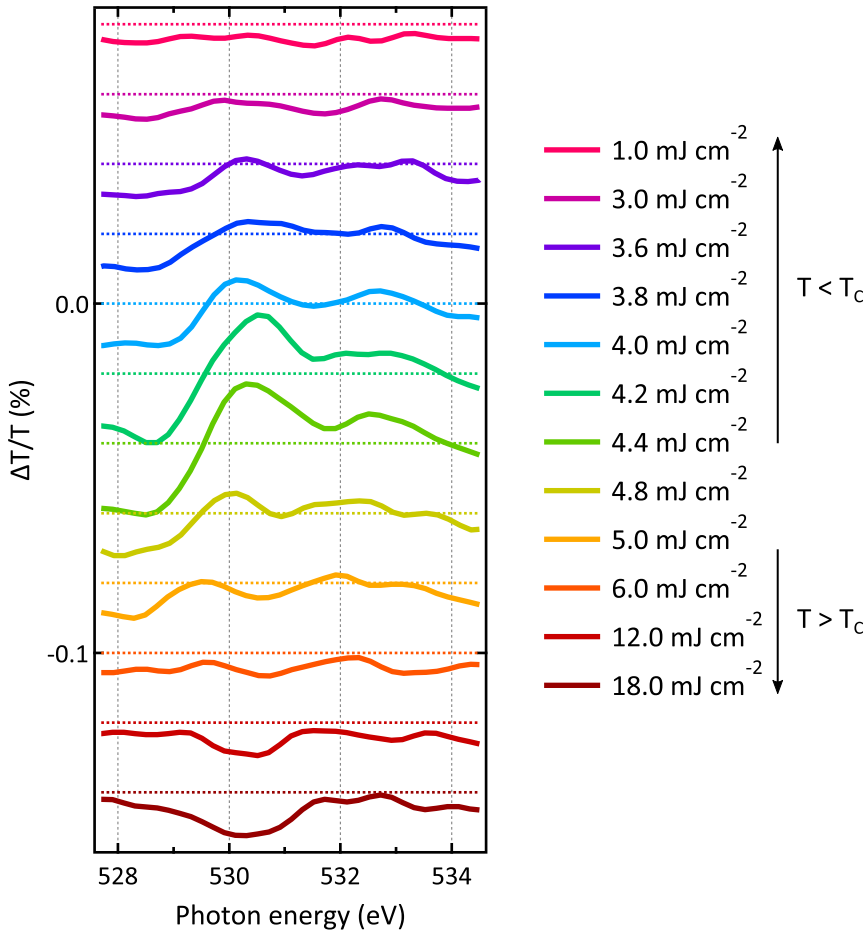

Fig. 4.4: Fluence dependent XAS spectra of VO_2 measured at +400 ps. The amplitude of the changes in transmission increases up to a pump fluence of 4.4 mJ cm^{-2}, where it reaches its maximum before decreasing until no transient change is observed at 5 mJ cm^{-2}. The traces are offset for clarity.

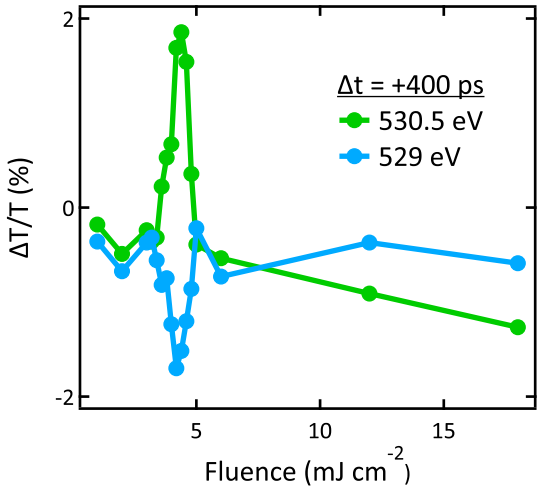

Fig. 4.5: Fluence dependence of the π^* and $d_{\parallel}$ states. Above a threshold of 3 mJ cm^{-2}, the amplitude of the change of both states start increase with fluence. After reaching 4.4 mJ cm^{-2}, they are reduced and there is no significant change already at 5 mJ cm^{-2}. For higher fluence, at 530.5 eV a signal with opposite sign with respect to the low-fluence signal is visible.

In order to understand this fluence-dependent behaviour, the full differential transient spectra at two crucial pump excitations are compared in Fig. 4.6 with the static differential spectrum. For a better comparison in terms of spectral resolution, the latter is calculated from the convolved static insulating and metallic spectra. A very good agreement is found between the static and transient spectra measured at 4.4 mJ cm^{-2}. A decrease of the $d_{\parallel}$ and an increase of the π^* states can be observed, which correspond to a transition from the insulating M_1 to the metallic R phase. Thus, from this it can be inferred that exciting with low fluences above a threshold of 3 mJ cm^{-2} induces the IMT. The discrepancy at the edges of the spectra coincide with those found between the equilibrium spectra in Fig. 4.2.

In Fig. 4.5, below 3 mJ cm^{-2}, no dynamics are observed above the level of signal-to-noise. At such low fluences, no structural transition is driven, hence no changes in the band structure and state dynamics are expected. Still, electron dynamics in the form of charge redistribution may be present after photoexcitation. This should primarily affect the conduction-band edge, probed with photon energies around 529 eV. The fact that no changes are observed in the present data suggests that either the carriers have already scattered their energy to the lattice on a much faster time-scale than the current resolution, or that the sensitivity of the experiment is not sufficient to probe such signal.

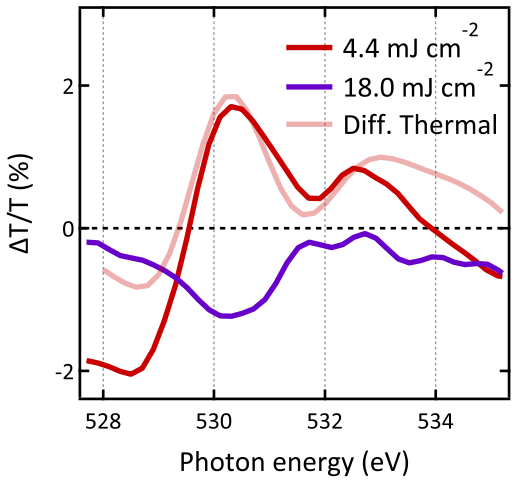

Fig. 4.6: Comparison of transient and static spectra. The differential transient transmission spectra measured at +400 ps at the oxygen K-edge display a different behaviour when excited by 4.4 mJ cm^{-2} (red trace) and by 18 mJ cm^{-2} (purple trace). The light-red trace corresponds to the calculated differential spectrum of the static spectra in Fig. 4.2(a) convolved with a spectral resolution of 1 eV.

On the contrary, when exciting with 18 mJ cm^{-2} (purple trace in Fig. 4.6), the transient spectrum displays a negative change in transmission with respect to the unpumped channel, that peaks around 530 eV, suggesting a different state is induced. Recalling the results presented in Chapter 3, the conditions under which this experiment was performed are not ideal for a complete recovery of the sample at high fluences to the ground state between pump pulses, so the sample remains above T_C. Therefore, above a fluence of 6 mJ cm^{-2}, the transient XAS signal is lost because the insulator-metal phase transition cannot be induced once the material is already in the metallic phase. And the signal that emerges above 18 mJ cm^{-2} corresponds to photo-excitation of the metallic phase. Further proof of the nature of the high-fluence data will be discussed in Section 4.2.3.

The temporal evolution of these observed changes is presented in Fig. 4.7, which represents three typical resolution-limited transient signals. The increase in transmission after photo-excitation at 530.5 eV and decrease at 529 eV are expected for the insulator-metal phase transition. The initial responses are resolution-limited, but, in the hundreds of picoseconds measured, they show no subsequent evolution, suggesting that the whole sample volume has transformed with no further growth of the metallic phase or thermal diffusion. The same can be said about the time scan measured with 18 mJ cm^{-2} in terms of temporal resolution, although this signal cannot be reconciled with the IMT,

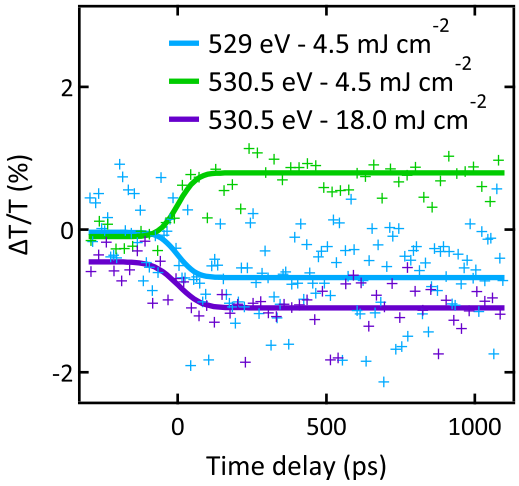

Fig. 4.7: Time delay scans at 529 eV and 530.5 eV. The time traces of the changes in the $d_{\|}$ and π^* states display the corresponding positive and negative responses when pumped with low fluence. At 530.5 eV there is a change of sign of the photo-induced changes in transmission.

but with the photo-excited rutile phase.

In view of the presented data, it is worth considering whether these spectra can represent an intermediate monoclinic metallic phase that emerges between the M_1 and R phases. The spectrum of such a state would result in an absorption peak at 530.5 eV due to the split $d_{\|}$ band characteristic of the monoclinic structure, and an energy shift of the π^* states, as they account for the metallic behaviour by crossing the Fermi level. Therefore, the differential XAS signal would display spectral shifts at 529 eV, with no changes in the 530.5 eV features [25]. However, by observing Fig. 4.5, both spectral features appear to change at the same fluence, strongly suggesting that the electronic and structural transitions are occurring concomitantly. Nonetheless, the possibility for the monoclinic metallic phase originating at an intermediate fluence within the range ∼3.4–3.6 mJ cm^{-2} and/or having a shorter life than the temporal resolution reported here, as suggested by previous ultrafast experiments [48, 51], cannot be completely excluded.

Summarizing, three fluence regimes can be defined in this experiment. For fluences below 3.4 mJ cm^{-2},the sample is initially in the insulating phase and the photo-excited M_1 is probed. For fluences within the range 3.4–4.4 mJ cm^{-2}, the phase transition is induced, and hence the M_1-to-R transition probed. Finally, above 4.4 mJ cm^{-2}, the photoexcited R phase is measured.

4.2.3 Heat effects in the structural transition

In order to determine the role played by laser-induced heat in the phase transition, the pumped and unpumped channels are analysed independently. As mentioned before, in ideal experimental conditions, the unpumped channel should probe the same state as if the laser was blocked, so it should never change regardless the excitation power. Moreover, this state should coincide with that probed by the pumped channels at negative time delays. This is not the case, though, in this experiment. Figure 4.8 shows the transient XAS spectra as measured by the pumped and unpumped probes separately. This way it can be observed how the trace pumped with $4.4\,\mathrm{mJ\,cm^{-2}}$, corresponding to the transient metallic phase, matches that of the unpumped channel when the sample is excited by $18\,\mathrm{mJ\,cm^{-2}}$. This proves that the differential signal found at this pump fluence reported in the previous section results from photo-excitation of the metallic phase.

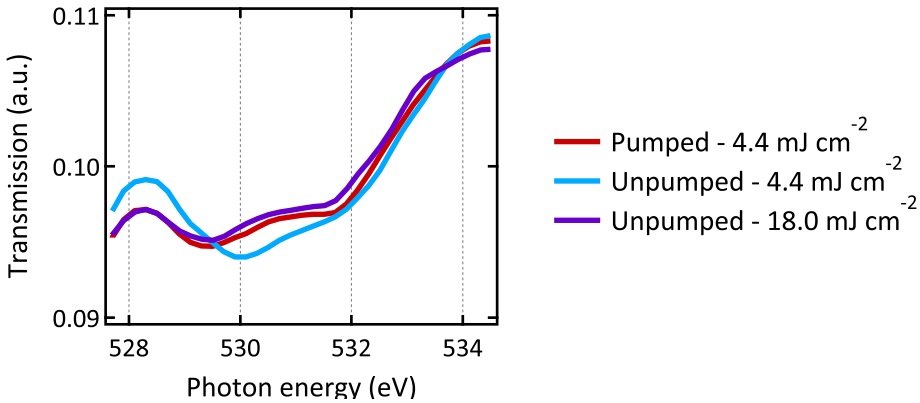

Fig. 4.8: Transient XAS spectra of the insulating and metallic states. For a pump fluence of $4.4\,\mathrm{mJ\,cm^{-2}}$ the phase transition is induced, with the unpumped channel probing the M_1 and the pumped channel probing the R phase. For a higher fluence of $18\,\mathrm{mJ\,cm^{-2}}$, the unpumped channel matches the spectrum of the metallic phase.

The transmitted intensities as a function of fluence of both channels, measured at positive and negative time delays, are plotted in Fig. 4.9. Figure 4.9(a) shows that at positive delay time, the pumped channel shows a decrease in transmission at $3.3\,\mathrm{mJ\,cm^{-2}}$, corresponding, as already seen before, to the IMT probed at 529 eV. However, the unpumped channel shows an abrupt change as well for a higher pump fluence, of $4.4\,\mathrm{mJ\,cm^{-2}}$. On the other hand, at negative time delays for the pumped signal, both channels decrease at once at the same fluence of $4.4\,\mathrm{mJ\,cm^{-2}}$. This variation of the unpumped channel can thus ac-

count for the reduced differential signal above 4.4 mJ cm^{-2} in Figures 4.4 and 4.5.

This demonstrates that, above such threshold, the steady-state properties of the material have changed due to laser-induced heat. As a result, for fluences above this value, at a repetition-rate of 600 Hz, the average temperature of the sample has been raised from 90 K by almost 300 degrees to lie above the insulator-metal transition temperature.

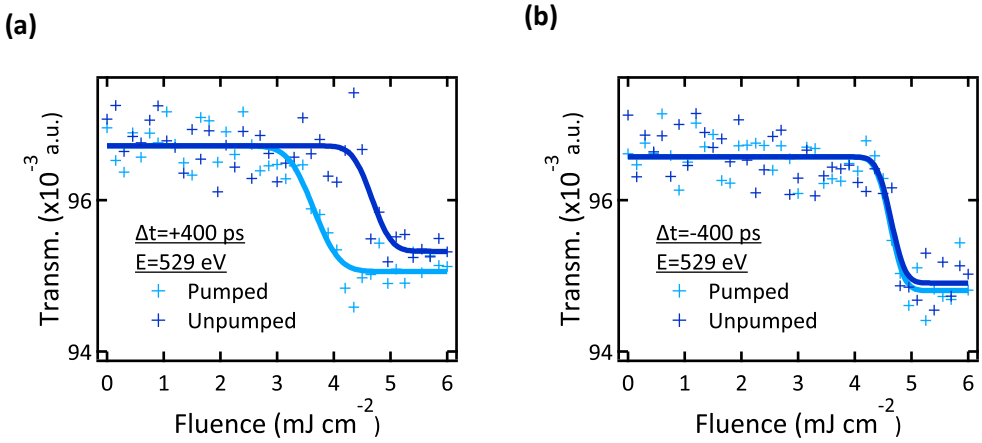

Fig. 4.9: Transmission as a function of fluence in the pumped and unpumped channels. **(a)** At positive time delays, a transient signal is observed in the pumped channel for fluences above 3 mJ cm^{-2}. From 4.4 mJ cm^{-2} on, the differential signal is reduced as the unpumped transmission changes as well. **(b)** At negative time delays, no differential signal is observed, but both channels change at the same fluence of 4.4 mJ cm^{-2}.

4.2.4 Transient optical response under equivalent conditions

In order to show that under these experimental conditions the material is truly in a long-lived metallic state for high pump fluences, complementary optical pump-probe measurements are performed under equivalent experimental conditions. However, measuring a real lattice-related response by means of optical measurements is a challenging approach. Whereas soft X-rays are capable of directly probing the crystal field, optical approaches are mainly sensitive to the overall density of valence states. Therefore, the results are always ambiguous in the sense that they can only probe the band structure in an indirect way through the dielectric function measurement. This hinders the separation of a metal-like signature resulting from a truly metallic response consequence of a band-gap collapse, and that arising from the presence of free carriers in

the conduction band due to photo-excitation but within an insulating band structure.

A method to overcome this difficulty and probe the structural changes associated to the IMT with an optical pump-probe measurement lies on probing the lattice potential through the generation of coherent optical phonons. This experiment was conducted in the optical laboratory at ICFO, employing the white-light generation setup shown in Fig. 4.10. The sample was maintained at 90 K in a cryostat under high-vacuum and the laser repetition-rate was set to 500 Hz. Note that the standard repetition-rate of 5 kHz of the optical laser can only be lowered by integer numbers, hence the speed discrepancy between the X-ray and optical measurements.

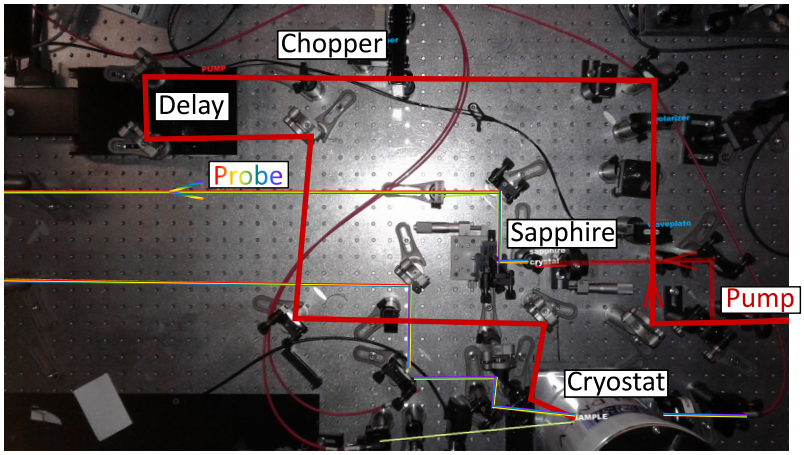

Fig. 4.10: White-light generation pump-probe optical setup. The sample, held in a cryostat, is excited with 800-nm pump laser pulses and probed by white-light pulses generated through a sapphire crystal. The transmitted intensity is recorded by a CCD camera inside a spectrometer.

Coherent phonon generation

In an absorbing material, photons from the pump pulse in the near-UV, visible, and near-IR regime couple to valence electrons, photoexciting them into previously unoccupied states. Such electronic charge redistribution within the solid generates a force onto the lattice. The restoring forces experienced by the ions upon their perturbation are dictated by the superposition of the phonon modes of the lattice potential. When the force is generated by an impulse-like excitation, with a duration shorter than the period of the phonons, coherent motions of the lattice are induced. Given that phonons modulate the dielectric

function of the material, these vibrations can be measured in the time domain through the transient reflection or transmission of the solid. When the symmetry of the system changes, as it happens upon a structural transition, the number and frequencies of the modes also typically change. This way, phonon modes can be employed as a signature of the current phase of the system.

In 2012, Wall *et al.* demonstrated how this process can be exploited to measure the temporal evolution of the phonon spectrum during the insulator-metal phase transition of VO_2 [57]. They found how, by exciting the material with sufficiently intense pump pulses, the phonon modes characteristic of the monoclinic M_1 phase dramatically collapse, an indication of the ultrafast modification of the entire lattice potential symmetry. This also suggests that, whereas in equilibrium the changes in ionic positions and in the phonon spectrum are concomitant processes, out-of-equilibrium the lattice potential may change before the ions have time to reach their new equilibrium positions. Thus, such a strong perturbation of the lattice potential may become enough for driving the system into the rutile phase. This way, the state of the system can be probed in a non-equilibrium situation.

The transient response of the sample at 600 nm is shown in Fig. 4.11(a). When the VO_2 film is excited by low fluences (2.2 mJ cm^{-2}, light-red trace), the ions in the M_1 symmetry vibrate around their equilibrium positions, giving rise to the observed coherent phonons oscillations. Increasing the pump excitation to 5.8 mJ cm^{-2} (red trace) causes a strong suppression of the phonon modes, indicative of the change in the lattice potential symmetry and the subsequent insulator-metal phase transition [57, 115]. At even higher fluences (dark-red trace), the optical response changes dramatically in two manners. Firstly, an offset is present at negative time delays, which indicates that the system is not in the equilibrium ground state when the pump pulse arrives. Secondly, the transient response follows a spike-like behaviour near zero time delay, a characteristic response of the metallic phase of VO_2. This can be confirmed by looking at the high-temperature pump-probe trace presented in Fig. 4.11(b). For this measurement, the cryostat temperature was maintained at 360 K, well above T_C, keeping the sample in the equilibrium metallic phase. The excited rutile phase shows the same spike-like response.

Noteworthy, an excellent agreement exists between the fluence regimes of the XAS and the optical measurements. At low fluences, there is no observable XAS signal in Fig. 4.5, as the lattice structure has not changed, and M_1 modes can be seen in the optical traces. In the intermediate fluence regime, the phonons suppression coincides with the changes in the π^* and $d_{\parallel}$ states, which are all signatures of the insulator-metal and structural transition. At

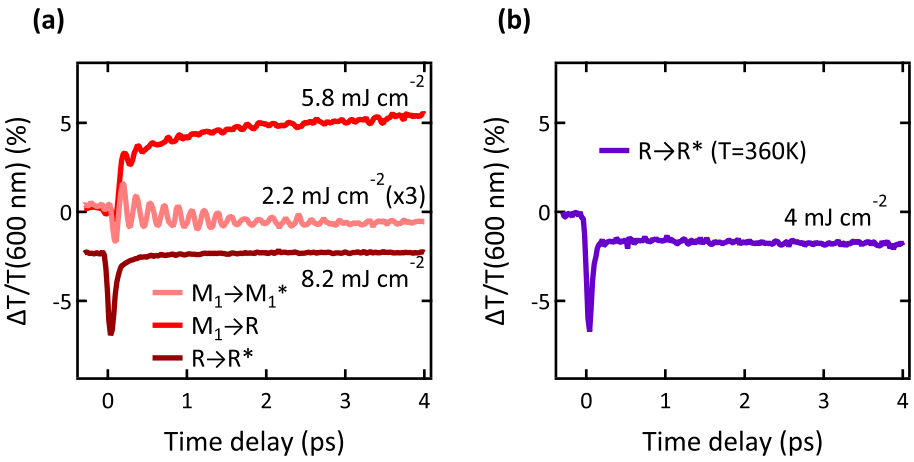

Fig. 4.11: Transient optical response at 600 nm. **(a)** Pump-probe traces measured with 800 nm pump-600 nm probe under similar experimental conditions as the time-resolved XAS. For low pump fluences (2.2 mJ cm^{-2}), the oscillations of the M_1 modes can be observed, which are suppressed when the sample is excited by higher fluences (5.8 mJ cm^{-2}), as expected for the M_1-R transition. Above 8 mJ cm^{-2}, the trace shows an offset at negative time delays and the transient response of the excited metallic state, indicating the sample has been heated above T_C. **(b)** Transient response of the equilibrium metallic phase, obtained by maintaining the sample at 360 K, well above T_C.

high fluences, the optical response shows an excited metallic behaviour, which confirms the previously presented interpretation of heat as the responsible for changing the steady-state properties of VO_2, raising the temperature of the sample above T_C. The excited rutile phase in the soft X-ray data appears as a change close to 530 eV, and will be further discussed in the following section. The small variations in threshold fluences between the two data sets arise from the different laser repetition-rates, slightly lower for the optical measurements, as already explained. This provides some more time for the sample to recover between pulses, and, therefore, a reduced temperature rise for the same fluence.

4.2.5 The photo-excited metallic state

Having established that at high excitation densities the pump-probe signal originates from the metallic phase, the reported transient absorption of the photoexcited metallic phase constitutes the first observation ever of such a signal in the soft X-ray regime.

In the metallic phase, the $d_{\|}$ band, located in the same energy region as the π^* states, is no longer split. Therefore, given the spectral position of the photo-excited rutile-phase signal, the system is treated as if only consisted of

the π^* states for simplicity. For a better comprehension, Figure 4.12 schematically depicts the band structure formed by the π^* states, probed with photon energies close to 529 eV, and the corresponding XAS signal that results from it, along different states of VO_2. Panels 4.12(a) and 4.12(b) illustrate the insulating M_1 and metallic R phases, respectively. In the former, the π^* states constitute the minimum of the conduction band, which lies just above the Fermi energy, and gives rise to the lower edge of the first absorption peak in the XAS spectrum. Upon transformation into the metallic phase, the π^* states move below the Fermi energy, leading to a red-shift of the absorption edge. This provides the existence of new states in the insulating gap, which results in an increase in absorption, or a decrease in transmission, close to 529 eV, as observed both statically and dynamically in Fig. 4.6. Notably, this change is not related to carrier dynamics, but a consequence of a modification of the band structure, as it occurs both in and out of equilibrium.

A reasonable question arises, though, about whether the signal observed in the transient excited metallic phase is due to a change in charge distribution, or, on the contrary, to a change in the density of states (DOS) and band structure. The first scenario is illustrated in Fig. 4.12(c), with a purely electronic response in which an increase of the electronic temperature leads to the depopulation of previously occupied states below the Fermi energy, while states above it become partially filled. Such a process is translated into a bipolar XAS feature close to 529 eV, as these photon energies probe states close to the Fermi energy. Specifically, below the initial edge, absorption increases (transmission decreases), given that X-rays can now probe lower-energy states that are less populated than they were before photoexcitation. Likewise, a small region above the Fermi level decreases in absorption (transmission increases), because previously empty states become now populated. These XAS features are not observed, however, in the transient spectra measured in the metallic phase in Fig. 4.6, but only an increase in absorption is observed at these photon energies.

The alternative scenario is represented in Fig. 4.12(d), with a change in the bandwidth of the π^* states. Such a process is consistent with the significant broadening of this band that occurs across the insulator-metal transition [13, 21]. A π^* band broadening results in an increase in absorption (decrease in transmission) above the Fermi energy, as new states at the top of the conduction band become available. This process might result counter-intuitive considering that thermal disorder and expansion reduces orbital overlap and, hence, bandwidths. However, this interpretation is in agreement with the recent experiment by Budai *et al.* [104] explained in Section 4.1, which showed

how the phonon anharmonicity of the rutile phase is decreased when increasing further the temperature away from the phase transition. Thus, phonon modes stiffen on heating, which actually reduces vibrational disorder. Interestingly, spectral weight is not conserved in this spectral region during such process, which also implies a change in hybridization with oxygen 2p or with other vanadium 3d levels, such as the $d_{\parallel}$ states. Further theoretical calculations are required for a definitive conclusion on this matter, which still represent a challenge nowadays. Yet, recent demonstrations that the properties of VO_2 can be captured through DFT in equilibrium [21] suggest that such studies might become available in the near future, even for complex materials as VO_2.

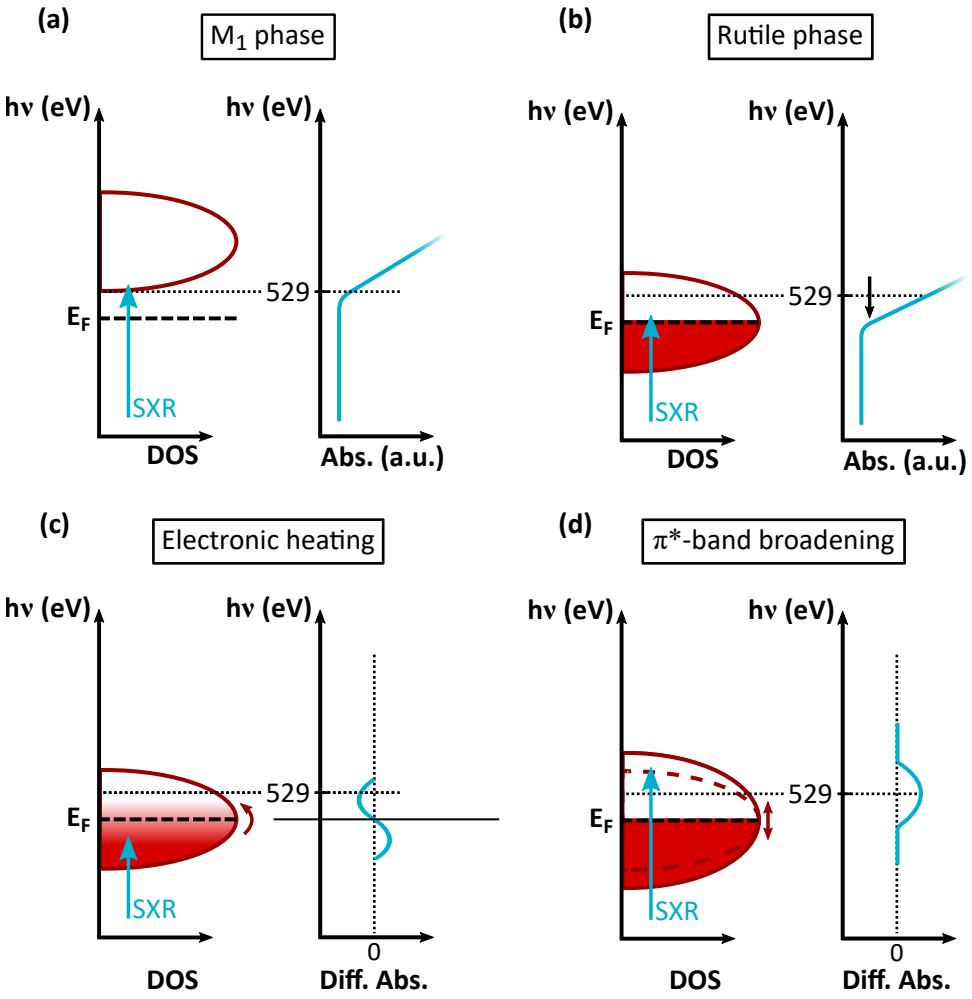

Fig. 4.12: Photoexcited metallic-state model. The scheme represents the density of states (DOS) probed by soft X-rays (SXR) through different states of VO_2 (for simplicity, only the π^* band is considered). **(a)** In the monoclinic insulating phase, absorption first occurs into the unoccupied states, separated from the Fermi level by the band-gap. **(b)** In the rutile metallic phase, the π^* states move below the Fermi level and XAS absorption occurs for lower energies than in the M_1 case. **(c)** A hot electronic state in the photo-excited metallic phase reduces occupation below the Fermi level and enhances it above, resulting in an increase in absorption at low photon energies and a decrease at higher ones. **(c)** Band broadening of the photo-excited metallic phase enables more absorption at higher photon energies without shifting the start of the absorption process.

4.2.6 Discussion

The results obtained here by means of time-resolved XAS are not in general agreement with those reported by Cavalleri and co-workers [98, 112]. However, it is important to notice that the samples employed for this work are of similar thickness than those used by Cavalleri *et al.* Therefore, the issue of the limited recovery of free-standing thin-film samples between pump pulses might have also affected those initial measurements. Those experiments were conducted at room temperature, with a repetition rate of 1 kHz and laser fluences of $25\,\mathrm{mJ\,cm^{-2}}$, which are significantly higher than those reported here. As a result, it appears highly probable that the pioneering measurements of the insulator-metal phase transition in VO_2 by time-resolved XAS were in fact conducted on the photoexcited metallic state, and did not, thus, reflect the dynamics of the IMT.

This work also presents the transient state of the metallic rutile phase upon photo-excitation in the soft X-ray regime for the first time. The results remark the major difference existing between the nature of this phase and the insulating one, which does not show any transient response at these time scales and photon energies. Moreover, the response of the rutile phase to photoexcitation agrees with the thermal response, which shows stiffening of the acoustic phonon branches when heating the system [104]. Such lattice hardening is a reflection of the reduced phonon anharmonicity and, thus, entropy in the material, which may lead to an increase in the states overlap and hybridization, causing an increase in absorption in the π^* states. However, the temporal resolution in the picosecond time-scales of this experiment is not sufficient to investigate the dynamics immediately after photo-excitation. In the following section, hard X-rays are employed to probe the lattice evolution across the phase transition with femtosecond temporal resolution.

4.3 Time-resolved hard X-ray diffuse scattering of VO_2

As discussed in the introduction of this chapter, lattice disorder plays an essential role in the equilibrium phase transition of VO_2. Yet, the importance of disorder in the ultrafast transition remains still unexplored. The main reason for this is that the techniques that can probe disorder on the ultrafast time scales have only recently been developed.

Current methods to probe the lattice have focused on Bragg scattering, which is a technique widely applied for the study of crystallographic structures. However, the advent of FELs has allowed in recent years to move beyond this, and measure not only Bragg peaks, but the total X-ray scattering arising from the sample, that is, including diffuse scattering. Non-equilibrium lattice dynamics can be investigated thereby within a typical pump-probe experimental setup in which X-ray pulses of sub-100-fs duration act as the probe. In order to understand the benefit from measuring this total X-ray scattering, a brief introduction of the concepts involved in the technique is given now.

When a monochromatic X-ray beam is diffracted from a periodic structure, such as a crystal, the constructive interference of the scattered beams from atomic planes gives rise to the so-called Bragg peaks. However, when density fluctuations are present within the lattice, the amplitude of such peaks is reduced, and the 'lost' intensity is redistributed into the inter-peaks background in the form of diffuse scattering. In that sense, diffuse scattering arises by departures from perfectly periodic arrays of atoms, the causes of which are wide, ranging from defects to thermal motion. The latter generates the so-called *thermal diffuse scattering* (TDS), which results from the population of phonon branches caused by the jittering of atoms around their equilibrium positions at non-zero temperatures. Larger displacements lead to more scattered X-rays. It is important to notice that, although the presence of defects also results in diffuse intensity, these scatter light elastically, while phonons do it inelastically. Whereas elastic Bragg scattering techniques measure the average atomic positions, providing thereby information on the long-range order, inelastic diffuse scattering is capable of probing the short-range structural order through the disorder of the system.

The total X-ray scattering approach adopted here exploits both features: discrete Bragg peaks and the diffuse scattering among them, allowing thereby the measurement of dynamics involved in the structural phase transition at all length scales. Such a technique is suitable for distinguishing between the two

types of structural transitions presented at the beginning of this chapter. Displacive and order-disorder processes give rise to different total X-ray scattering patterns, as schematically illustrated in Fig. 4.13. If increasing the temperature above T_C induces a displacive process, the vanadium atoms arranged in dimers collectively change their positions driven by spatially coherent vibrations of phonons with wavevector at the rutile R-point. At low temperatures, defined Bragg peaks, corresponding to the M_1 structure, can be observed. When the temperature is increased towards T_C, the diffraction peaks decrease in intensity as the V ions move away from their original positions until no M_1 peaks are visible above T_C. This 'lost' intensity is transferred among peaks, that is, while the amplitudes of the M_1 peaks get weaker, those of the R peaks get stronger.

Alternatively, in an order-disorder transition (Fig. 4.13(b)), the atoms move from the low- to the high-symmetry structure in an uncorrelated manner, with no defined wavevector. The intensity of the Bragg peaks also decrease in intensity when warming towards T_C, but, whereas in the displacive case a peak at a particular Bragg angle disappears because the atoms have reshuffled their positions, in this type of transition, the peak vanishes due to a lack of constructive interference at this wavevector. In this case, the 'lost' intensity is transferred both to the R peaks and the diffuse scattering, which results in the former not getting quite as intense as they would be in a displacive process. Additionally, the uncorrelated disorder leads to large-amplitude motions of the vanadium ions that still scatter the impinging X-rays, giving rise to extended diffuse scattering across reciprocal space. Distinguishing these two scenarios by means of Bragg scattering alone can be considered a nearly impossible task, as to do so, an extremely large number of Bragg peaks needs to be measured with good signal-to-noise ratio.

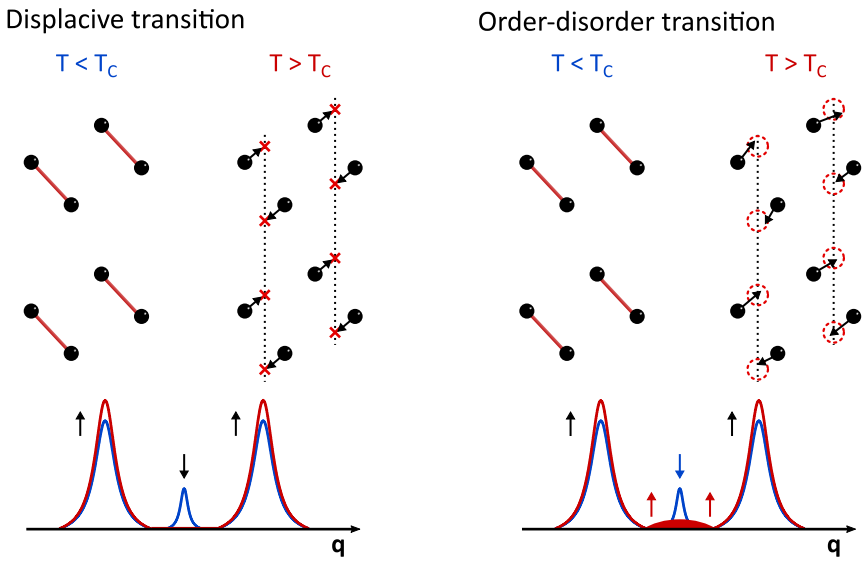

Fig. 4.13: Total X-ray scattering for displacive and order-disorder transitions. (a) In a displacive transition, diffraction peaks decrease in intensity as the phase transition is approached due to the cooperative motion of the V ions towards their new positions in the rutile structure (red crosses). Above T_C, no intensity is recorded at that particular wavevector, as the V ions have shifted into their new rutile positions. **(b)** In an order-disorder transition, the lack of coherence motion of the V ions when approaching the phase transition leads to a reduced Bragg peak amplitude, but X-rays are still reflected incoherently into a diffuse background. Above T_C, the positions of the V ions can be found at any point within the red circles.

4.3.1 Ultrafast disordering of vanadium dimers

Time-resolved XDS measurements were carried out at the XPP end-station [116] at the Linac Coherent Light Source (LCLS) X-ray FEL, using 1.5 eV pump pulses and 9.5 keV probe pulses on high-quality single crystals of VO_2. Complementary measurements were performed at beamline BL3 of SACLA FEL under the same conditions. The laser repetition rate was set to 120 Hz and the sample was held in air, although enclosed in a helium purge box to reduce air scattering of the X-rays, which can be of similar magnitude as the diffuse intensity. A sketch of the experimental setup is illustrated in Fig. 4.14. In order to match the penetration depth of the optical pump and X-rays probe beams, a grazing-incidence geometry was adopted. The X-rays impinged on the sample at an angle of 0.5° and the pump laser was incident at 2.3°. Scattered X-rays were recorded with a large-area detector, a Cornell-SLAC Pixel Array Detector (CSPAD), which allowed for the measurement of extended $\boldsymbol{q}$-regions of reciprocal space.

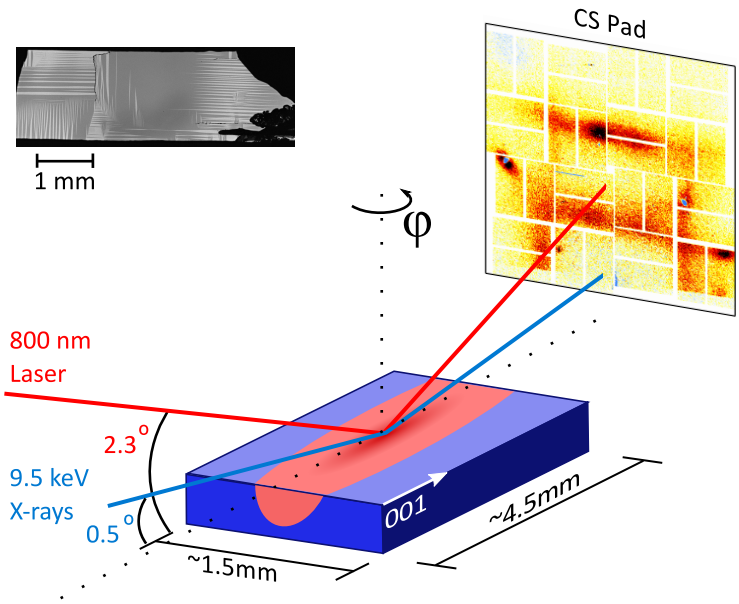

Fig. 4.14: Scheme of the experimental setup for time-resolved XDS. The sample was mounted at grazing incidence to match the pump and probe penetration depths. Rotations around the sample normal enabled the measurement of different regions of the total scattering pattern. A zero φ angle corresponds to the beam incident along the rutile c-axis. The upper left insert shows a polarized-light microscopy image of the VO_2 single crystal used in the experiment. The light and dark patches correspond to M_1 twin domains.

The sample mount was connected to a heating stage to measure the total X-ray scattering patterns of the insulating and metallic equilibrium phases of VO_2. Figure 4.15(a) shows the static TDS patterns for the monoclinic structure measured at room temperature, characterized by the presence of Bragg peaks at defined wavevectors. When heating the sample above T_C, the scattering dramatically changes, as can be seen in false-colour plot of the differential TDS between the 353 K pattern and the M_1 displayed in Fig. 4.15(b). This is dominated by the suppression of Bragg peaks of the M_1 phase (blue negative spots) and the emergence of a strong rectangular-shaped diffuse feature. Simulations of the change in total scattering based on the equilibrium force constants obtained via DFT calculations are capable of reproducing these TDS patterns, and indicate that the rise of diffuse scattering originates from the soft transverse acoustic phonons of the rutile phase that correspond to the vanadium ions that dimerize in the monoclinic phase [104]. The calculated thermal difference (panel (c)) is in excellent agreement with the measurements, reproducing the loss of M_1 peaks and the diffuse scattering enhancement. More interestingly, when photo-exciting the sample in the saturation regime, the X-ray scattering

recorded after 350 fs, displayed in 4.15(c), shows a strong resemblance to the thermal changes in 4.15(b). Notably, the regions where the diffuse intensity is strongly enhanced are confined to those expected for the equilibrium metallic phase. This shows that, on this rapid time scales, not only has the long-range symmetry of the crystal changed, as indicated by the fast suppression of the M_1 peaks, but also the vanadium atoms have already adopted a rutile-like displacement distribution.

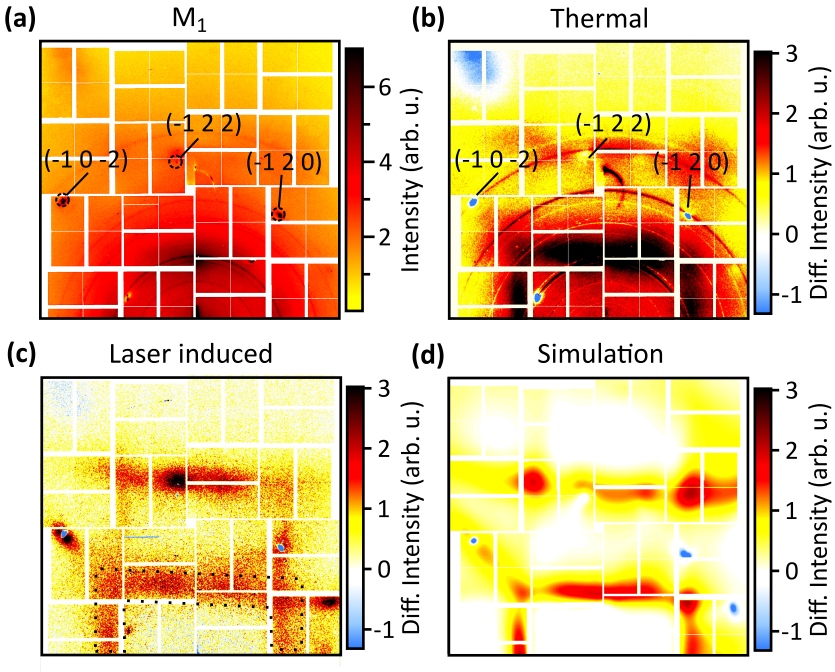

Fig. 4.15: Total X-ray scattering patterns of the low- and high-temperature structures. **(a)** In the thermal M_1 phase, the scattering pattern is dominated by the tails of three Bragg peaks. The small amount of diffuse scattering is an indication that the vanadium dimers are tightly bound, with only small-amplitude oscillations of the bond lengths and angles. **(b)** In the thermal difference R-M_1 TDS, Bragg peaks are lost and there is a large increase of diffuse scattering with a box-like shape. **(c)** The scattering pattern recorded 350 fs after photo-excitation with 20 mJ cm^{-2} shows a dramatic suppression of the M_1 peaks and a strong increase of diffuse scattering. Remarkably, this is enhanced in the same regions as those in the equilibrium metallic pattern. **(d)** The simulated differential pattern obtained with the equilibrium force constants extracted from DFT calculations is in excellent agreement with (b).

Notably, observing the temporal evolution of the Bragg peaks and the momentum-dependent diffuse scattering intensities displayed in Fig. 4.16, it becomes apparent that the decrease of the former and the increase of the latter occur on the same time scales, as soon as 50 fs after photo-excitation, the experimental time resolution. This proves that local disorder happens as fast as the loss of the long-range M_1 symmetry, which indicates that the transition is dominated by disordering of the vanadium ions rather than by a coherent atomic motion along a single wavevector. The resemblance to the diffuse distribution of the equilibrium rutile phase is found to be achieved at 150 fs, showing little subsequent changes after this point. Remarkably, the time scales for the structural transition appear to be at least twice as fast as previously reported transition velocities from ultrafast X-ray diffraction measurements [51, 56].

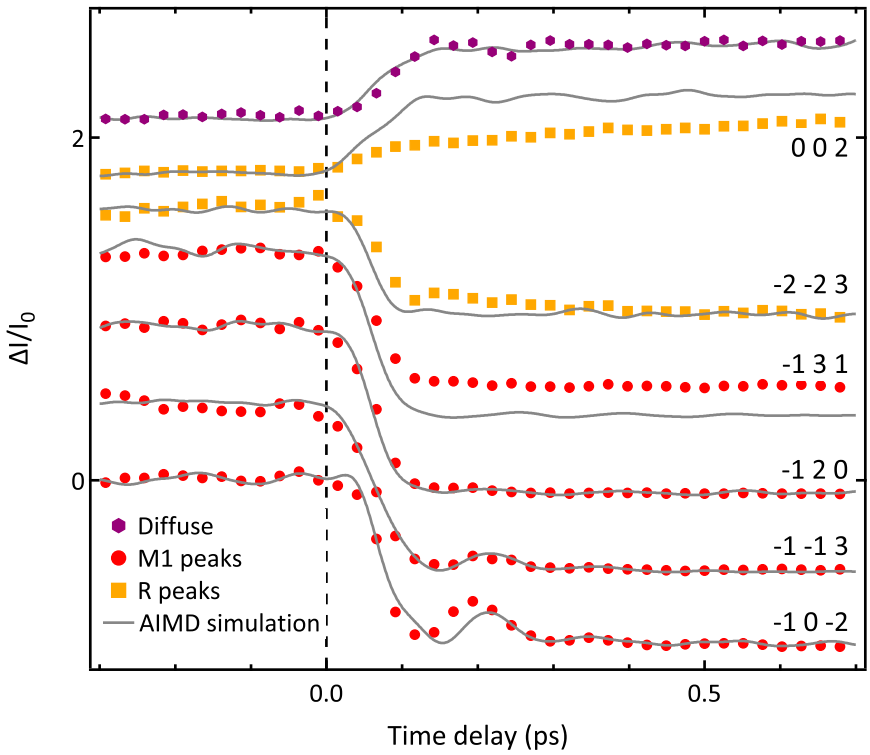

Fig. 4.16: Time dependence of the Bragg peaks and diffuse scattering. Data from the Bragg peaks is normalized to the pre-time zero amplitude for both experiments and calculations with no further scale factors. The traces are in excellent agreement with AIMD simulations (solid lines). The diffuse scattering data is obtained from integration over the boxed area in Fig. 4.15(c), and compared to the variance of the V positions extracted from AIMD simulations.

Ab initio molecular dynamics (AIMD) simulations of the photo-induced phase transition were performed to gain better insight into the dynamics observed. With this aim, the effect of laser photoexcitation is modelled as a prompt increase in the electronic temperature of the system within 1 fs. The structural transition from M_1 to R was found to show a threshold-like behaviour with T_{el}, above which the V dimerization is lost, as well as the twisting angle of the V atoms. This provides the electronic temperature value required to drive the phase transition, and hence to be included in the AIMD simulations. To simulate the effect of the laser pulse, at each time step of 1 fs, the charge redistribution resulting from the temperature jump is used to calculate the force constants on the atoms by means of DFT calculations (same method as in [104]). From the ionic positions extracted, both the time-dependent Bragg and diffuse scattering intensities were calculated, represented by the solid lines in Fig. 4.16. An excellent agreement can be observed in terms of the time scale dynamics and the amplitude changes.

The effect of changing the electronic temperature by photoexcitation is also simulated on the change in V-V bond lengths, schematically represented in Fig. 4.17(a). At negative time delays, the monoclinic dimerization pattern is represented by the bimodal initial distribution formed by the short dimerized bonds (2.50 Å) and the long bonds (3.16 Å) along the rutile *c*-axis. After the abrupt transition, both distances merge into the same value, leading to the equidistant configuration expected for the rutile structure. Interestingly, similar dynamics are observed for the twisting angle, suggesting that changes in bond lengths and angle occur concomitantly and within less than 300 fs, as opposed to previous results based on Bragg scattering analysis alone [56], and other reported scenarios in which the V-V melting was claimed to be decoupled from the vanishing of the twisting angle, leading to an intermediate monoclinic metallic phase [42]. As a result from AIMD simulations, the bonding dynamics change on very fast time scales consistent with those found for the diffuse scattering rise.

Contrary to displacive processes, in which the normal frequencies of the driving phonons limit the speed of the transition, here the vanadium atoms adopt a rutile-like displacement distribution faster than the oscillation period of any of the relevant modes, and much faster than the time required for a cooperative unit cell rearrangement. This implies that the energy from the laser pulses is transferred extremely rapid to the lattice, which can only occur if the system finds itself beyond the harmonic motion regime. The AIMD simulations show, in fact, that the interatomic potential induced by photoexcitation is strongly anharmonic and flat, allowing for the vanadium atoms

to adopt large displacements about their average positions in the rutile phase, as illustrated in Fig. 4.17(b). This uncorrelated motion stands actually as the origin of the high phonon entropy of the equilibrium metallic phase previously reported [104, 111].

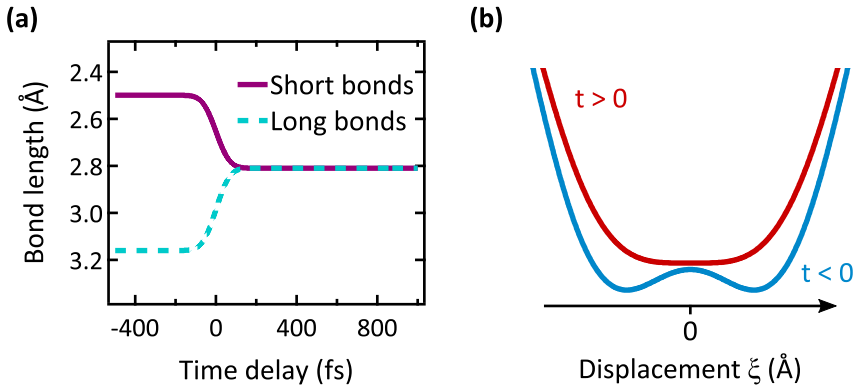

Fig. 4.17: Lattice potentials and V-V bonding upon photo-excitation. **(a)** At negative time delays, the V bond lengths are divided in short and long distances, corresponding to the M_1 dimerization. After photo-excitation, they quickly collapse to one distance corresponding to the rutile chains of equidistant V atoms. **(b)** Local potentials along the reaction coordinate dramatically change after photo-excitation. The M_1 phase is characterized by a double-well potential that corresponds to the V-V dimers. The large-amplitude vibrations induced by above-threshold fluences lead to a sudden lifting of the two minima, stabilizing the rutile flat anharmonic potential. (The actual simulations can be found in [117].)

These measurements, confirmed by simulations, demonstrate that the photo-induced phase transition in VO_2 is of the order-disorder type, driven by an ultrafast change of the lattice potential that suddenly disorders the vanadium dimers and yields large-amplitude rutile-like uncorrelated motions of the V ions. The flat dispersiveless transverse acoustic phonon branches in which this results proves that the transformation does not follow a single well-defined wavevector, but proceeds without spatial coherence.

4.3.2 Fluence dependence of the structural transition

As mentioned above, the AIMD simulations predict a threshold-like behaviour of the M_1 structure when varying the electronic temperature of the system. Namely, above ∼2900 K, the short and long V-V bonds abruptly collapse to the same value, while the twisting angles become 180°, resulting in a rutile-like structure. This is consistent with the first-order nature of the phase transi-

tion, and hence, with the existence of a laser fluence threshold for triggering the process. Experimentally, the intensity of both the Bragg peaks and the diffuse scattering show a threshold-like behaviour with pump fluence, changing abruptly above $\sim 5\,\mathrm{mJ\,cm^{-2}}$, as displayed in Fig. 4.18. The Bragg peak decreases linearly in intensity with absorbed fluence below the threshold, after which the change is more rapid until saturation. In fact, the dynamics are clearly different below and above threshold, as shown in Fig. 4.19. At low fluences, the response of the Bragg peak's intensity is modulated by coherent oscillations of the 5.7 THz phonon mode of the M_1 phase, which are lost by increasing the fluence above threshold, in agreement with optical measurements in Fig 4.11 and in [57]. On the other hand, the prompt rise of diffuse scattering above $\sim 5\,\mathrm{mJ\,cm^{-2}}$ indicates that the vanadium ions only adopt the rutile-like distribution above a critical fluence, which is the same for the loss of long-range order.

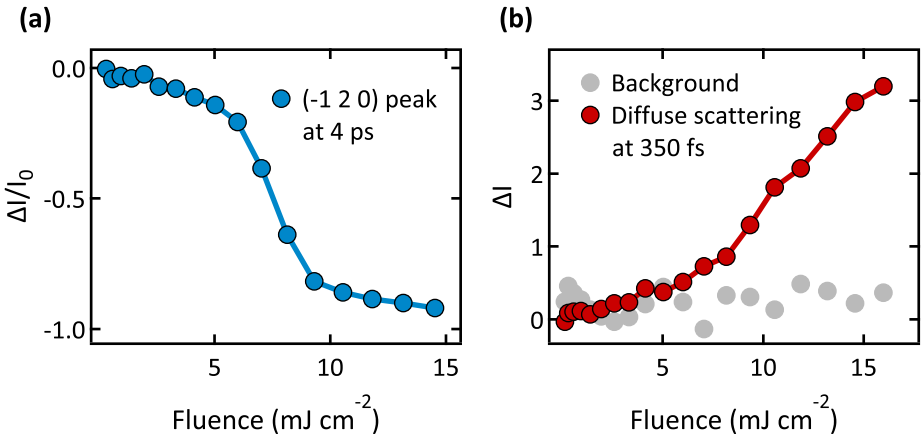

Fig. 4.18: Pump fluence dependence of the diffuse scattering and an M_1 Bragg peak. **(a)** The (-1, 2, 0) M_1 peak amplitude, visible in Fig. 4.15(a), presents a linear decrease in intensity for fluences below a threshold $\sim 5\,\mathrm{mJ\,cm^{-2}}$, after which the change is rapid until saturation. **(b)** The mean diffuse scattering, integrated over the squared box in Fig. 4.15(c), shows an abrupt rise above a similar value of $\sim 5\,\mathrm{mJ\,cm^{-2}}$. The grey dots represent the background, taken as the mean intensity measured at low scattering angles.

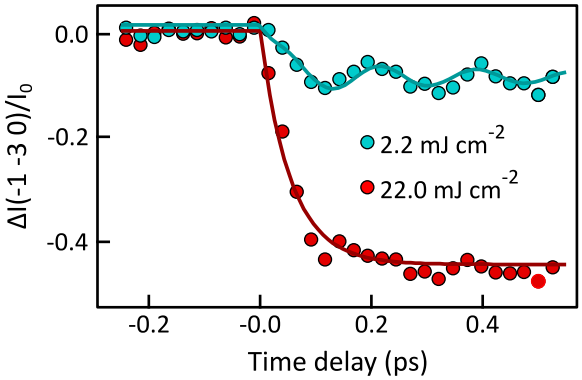

Fig. 4.19: Below- and above-threshold dynamics of a M_1 Bragg peak. Coherent phonon oscillations can be observed for low fluences, which are well fitted by a 5.7 THz phonon mode. At higher fluences, the Bragg intensity is strongly suppressed and the oscillation is lost.

As explained in Chapter 3, the existence of different threshold fluences for changes in the optical and structural probes has been provided as evidence for the existence of a transient metallic monoclinic state. From the results of Chapter 3, though, it was concluded that the threshold for different wavelength probes is the same, at least within the optical regime. Here it has been demonstrated that scattered X-rays directly probe the evolution of the lattice across the phase transition. Therefore, if the threshold measured for the structural transition were higher than that encountered with optical probes sensitive to free carriers, this could be proof for the metal-like monoclinic phase. With this aim, the fluence thresholds for the structural transition of the same type of single crystal as that employed in the XDS experiment is also measured and is shown in Fig. 4.20. The optical measurements were conducted with a 800 nm probe at a pump repetition rate of 1 kHz, with the sample held at room temperature and atmospheric pressure. The threshold is found to be of $\sim 6.3\,\mathrm{mJ\,cm^{-2}}$. This value is in good agreement with the threshold found by means of hard X-rays considering the different experimental conditions. In particular, the XDS measurements were performed in a grazing configuration, where the large angle of incidence requires additional reflectivity factors to account for the absorbed fluence. This may result in extra discrepancies between the measurements in the two experimental setups.

As a result, no decoupling of the change in optical and structural properties can be determined from these results. Instead, the insulator-metal phase transition is characterized by a single fluence threshold, above which the electronic and structural properties change abruptly due to the rapid disorder of

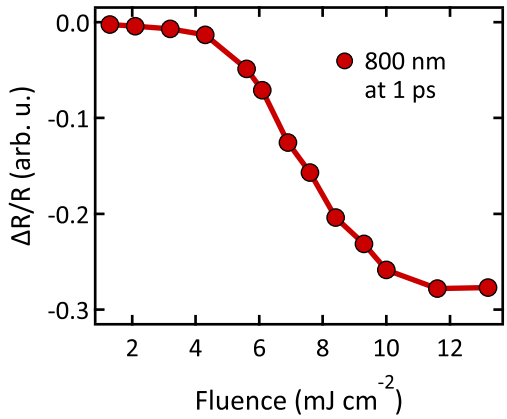

Fig. 4.20: Pump fluence dependence of the optical response. A VO_2 single crystal, probed with 800 nm, gives a threshold fluence of $\sim 6.3\,\mathrm{mJ\,cm^{-2}}$.

the vanadium ions. Such pump laser threshold appears to be directly related to the electronic temperature of the system, which is transferred to the lattice in less than 100 fs, leading to a dramatic change of the potential symmetry.

4.3.3 Discussion

These results lead to a new description of the photo-induced phase transition in VO_2, in disagreement with several previous reports. Traditional symmetry considerations and analysis based on Bragg scattering data alone have led to the general conception of a conventional soft-mode transition driven coherently by phonons of well-defined wavevector that limit the speed of the transition, without considering the role played by fluctuations and entropy. As a result, the ultrafast community attempted to solve the "Mott vs Peierls" competition by separating the two types of transitions in the time domain, considering that electronic correlations should act faster. The results presented in this thesis strongly challenge this rather simple interpretation, as the instantaneous change of the lattice potential induced by photoexcitation causes the V ions to quickly vibrate as if they were in the rutile phase within at most 50 fs. This is reflected in the prompt emergence of the diffuse scattering signal characteristic of the flat anharmonic rutile potential, which, considering that it is dominated by low-energy acoustic phonons, means that such "slow" modes are responding in a non-equilibrium situation in much shorter time scales than those set by their equilibrium frequencies. Therefore, a photo-induced phase transition driven in an ultrafast fashion is no longer necessarily an electronic-driven process.

Still, the rapid excitation of vanadium ions into the rutile potential observed here is faster than other disorder-driven transformations [97, 118]. The non-equilibrium order-disorder transition time scales are dictated by the time required for the ions displacements to become uncorrelated and reach a quasi-equilibrium distribution. The dynamics observed in this experiment are fast due to the relatively short distances between the V positions in the M_1 and the R structures, found to be of 0.24 Å. The average vanadium velocity at room temperature is 3.8 Å ps^{-1}, which means that they could traverse such distance in approximately 60 fs. The speed of the transition is, thus, mainly limited by the initial velocity distribution of the ions. The broader the initial thermal distribution, the less it takes for the vibrations to reach the final large amplitudes.

The rapid disordering and evolution to the quasi-equilibrium rutile structure is enabled by the strongly anharmonic lattice, which leads to a great phonon entropy that ultimately stabilizes the metallic phase. These observations of the ultrafast phase transition are interestingly in accordance with the thermal transition described by Budai *et al.* [104]. Remarkably, the induced lattice potential of both the thermal and ultrafast transition can be described by a hot-electron distribution within the DFT framework, without the need of additional strong Hubbard electronic correlations parameters. As a result, the in- and out-of-equilibrium transformations appear to follow the same pathway towards the high-temperature metallic phase.

4.4 Conclusions

The results presented in this chapter obtained by probing the structural response of VO_2 across the insulator-metal phase transition demonstrate that the conventional conception of this extensively studied phenomenon needs to be re-addressed.

On one hand, the XAS experiment presented here stands as the first time-resolved measurement of the phase transition of VO_2 in the soft X-ray regime, as the pioneering results of Cavalleri *et al.* were most likely conducted on the metallic state of VO_2 due to heat-accumulation-related issues. Here it is shown how simple steps can be taken for measuring the insulator-metal phase transition at reasonable repetition rates, which should be considered in future similar experiments performed on thin films samples with lack of a heat sink. Extending these measurements to the femtosecond time domain will enable the study of charge dynamics immediately after photoexcitation within the π^* and $d_{\|}$ states. This could be achievable at FELs, which would also benefit the measurements due to their lower operating repetition rate.

On the other hand, the ultrafast total X-ray scattering measurements reveal that the traditional idea of the *molecular movie*, in which information about the atomic positions as a function of time is obtained through elastic Bragg scattering, provides an incomplete picture of the microscopic physics. In order to obtain insight into the forces that drive atomic motion, the inelastic components of the scattering signal are also essential, shedding light on the entropy of the system. Yet, the high photon momenta together with the femtosecond temporal resolution required for studying such lattice dynamics are currently only achievable in X-ray FELs. As a secondary outcome, thus, this work also reflects the importance of large-scale facilities development for investigating these complex materials, in which entropy and lattice anharmonicity are believed to play a major role.

From the theoretical perspective, the missing component of DFT calculations for understanding the properties of transition metal oxides like VO_2 has traditionally been considered to be related to electronic correlations. Yet, most models of the so-called correlated materials do not include anharmonic phonon interactions either. Works by Eyert [21] and Budai and coworkers [104] have recently demonstrated that DFT can effectively reproduce the physics of VO_2 provided the right hybrid functionals are employed, without the need of adding strong Hubbard electronic correlations. AIMD simulations within the DFT framework are capable of accounting for anharmonic effects and ade-

quately describe the properties of VO_2 in a non-equilibrium situation as well. As a result, lattice anharmonicity may be the missing component for a complete understanding of complex materials that present such strong electron-phonon coupling. The development of these theoretical approaches may result, in the near future, in a complete description of XAS transient spectra and a definitive assessment of the physics behind the observed photoexcited metallic state.

The two experiments presented here provide results in good agreement with each other. The rapid energy transfer within 100 fs from electrons to the lattice when photoexciting VO_2 above threshold supports the interpretation given for the transient XAS features observed of the photoexcited insulating and metallic phases based on changes in the crystal field rather than charge dynamics, as electrons have already transferred their excess energy to the lattice at the longer picoseconds time scales measured. Furthermore, this strong electron-phonon coupling, which is ultimately responsible for driving the phase transition, is manifested in the π^* states broadening of the photoexcited metallic stated probed by time-resolved XAS.

As a final remark, it is worth noting that none of the results reported here suggest the existence of a transient monoclinic state with metallic properties, as previously reported by structural time-resolved studies [51, 56]. The rapid dynamics of changes in both Bragg peaks and diffuse scattering observed within 50 fs makes it unlikely that the reason for not measuring a transient monoclinic metallic XAS spectra is the short-lived nature of it. Moreover, the pump fluences required for triggering the transition appear to be the same when probing the optical and structural properties, which disproves previous results attributing a lower threshold for the emergence of metallic-like properties and a higher one for the structural distortion. In conclusion, all evidence provided here suggest instead a direct transformation from the M_1 to the R phase within an order-disorder process via the same pathway for both the ultrafast and thermal transitions.

5 | Conclusions and outlook

The insulator-metal phase transition of vanadium dioxide has been an active area of research for the past 50 years. The central issue has been focused on whether electron-electron interactions or electron-phonon coupling are responsible for triggering the phase transformation. Several experimental and theoretical studies have provided contradictory results, which challenged even more the understanding of the physics behind this process. One of the main open questions is the existence of a monoclinic metallic phase of VO_2. Whether such a transient state emerges during the phase transition, either dynamically or in equilibrium, has been actively investigated over the past years. The interpretation of the experimental results is hindered by the use of various types of samples (single crystals, thin films, free-standing, nanobeams), which can exhibit very different behaviours.

In an attempt to unify previous investigations in a single scenario that explains the inconsistencies and provides a new understanding of the phase transition, an extensive and complete study of the phase transition of VO_2 was carried out in this thesis, both in and out of equilibrium. To do so, this thesis exploited light of wavelengths spanning an ultra-broad spectral range, from the mid-IR to hard X-rays, which has enabled the examination of samples from the atomic to nanometer length scales, and from the femtosecond to microsecond time scales.

The outcome of this research strongly suggests that when appropriate care is taken, the results obtained from different measurements can be combined in a consistent way. In doing so, the conclusions reached is that there is no transient monoclinic state with metallic properties, neither in equilibrium nor out of it, and that the ultrafast phase transient transition is consistent with a phonon-mediated process, just like the thermal transition.

More specifically, the achievements and findings from this extensive research are summarized in the following.

In **Chapter 2**, a holographic imaging technique that exploits the use of resonant soft X-rays is applied for the first time to study the thermal insulator-metal phase transition. This method can track the onset and evolution of phase separation with increasing temperature, with a clear visualization of the growth of nano-sized domains. Thanks to the capability of the technique to resolve polarization- and energy-dependent XAS features, the heterogeneous response of the material can be distinguished in terms of the electronic and structural degrees of freedom. Defects are found to play a major role in the phase transformation, as they are responsible for modifying the local strain environment, leading to the formation of additional insulating phases, such as the monoclinic M_2. Nucleation of the different phases occurs at subsequent temperatures, which can explain the different transition temperatures found by other studies, which were assigned, probably due to their lack of nanoscale spatial resolution, to decoupled electronic and structural transitions. The major advantage of holography is the feasibility of combining this imaging approach with ultrashort X-ray pulses from FEL sources to directly visualize the nanoscale dynamics of the photo-induced phase transition in real-time with sub-100 fs temporal resolution. This experiment stands, thus, as the first step towards dynamical imaging, and the experimental challenges needed to be overcome to achieve this are presented in Appendix A.

In analogy to the claim of different transition temperatures that trigger decoupled electronic and structural transitions, the existence of different threshold fluences for the photo-induced phase transition has also been reported. Motivated by this, in **Chapter 3** the effect of laser-induced heat on the phase transition is investigated. To do so, a semi-ultrafast approach is applied, based on the use of a continuous-wave laser source for probing the sample response after photoexcitation. This way, the recovery dynamics in the millisecond regime could be measured. The threshold fluence of the phase transition is found to be dramatically dependent on the experimental conditions. External factors, such as the pump laser repetition rate and spot-size, holding the sample in air or vacuum, and even the probe fluence (not always negligible) can lead to need of longer times for the sample to relax back to the ground state, resulting in heat accumulation that raises the initial temperature of the sample. Interestingly, these long-time dynamics can be reproduced by a simple thermal model. Furthermore, in this chapter it has been demonstrated that, when the experimental conditions are strictly controlled, the threshold values obtained by probing the electronic band-gap (mid IR) and the structure (visible) are the

same, indicating there is only one photo-induced transition in VO_2.

The sensitivity of soft X-rays within the oxygen K-edge to the structural distortion of VO_2 observed in Chapter 2 was again exploited in **Chapter 4** to probe the evolution of the crystallographic structure during the photo-induced phase transition on picosecond time scales. Again, in agreement with the findings from the previous chapter, the XAS features that exhibit changes across the phase transition do so above the same threshold fluence, displaying no decoupled processes. These time-resolved measurements of the insulator-metal phase transition of VO_2 in the soft X-ray regime turned out to be the first, as previous attempts were hindered by laser-induced heat effects, now clear from the studies of Chapter 3. Furthermore, this experiment provides the first time-resolved XAS measurement of the transient state of the metallic phase upon photoexcitation, which exhibits a lattice potential stiffening through the broadening of the π^* band. The phonon spectrum dynamics were measured in the femtosecond time scales by means of ultrafast hard X-ray total scattering. This experiment demonstrated that, as it occurs in the thermal transition in [104], the photo-induced process is also driven by the entropy of the system provided by a strong electron-phonon coupling. The phonon spectrum was found to adopt the rutile-like symmetry in less than 50 fs (resolution-limited), much faster than the time scales set by their equilibrium frequencies, leading to a new description of the phase transition in terms of an order-disorder rather than a displacive process.

A new physical description of the phase transition of VO_2

In this new description of the insulator-metal transition, the atoms displacements towards their new equilibrium positions is dictated by their initial thermal velocity distribution. This also gives an explanation for the temperature dependency of the threshold fluence reported in Chapter 3. For lower base temperatures of the sample the initial thermal distribution becomes narrower, and therefore, more energy density is required for the ions to achieve the rutile-like large-amplitude oscillations that provide the entropy that stabilizes the metallic phase. As a result, the threshold fluence is higher at lower temperatures.

Regarding the question about the possible different mechanisms lying behind the thermal and ultrafast phase transitions, there is enough evidence from the different experiments performed in the scope of this thesis to suggest a common pathway for them:

- The recovery dynamics of the photo-induced phase transition are well

described by a simple thermal model that only accounts for the difference in temperatures within the system.

- The threshold fluences measured, although different under diverse experimental conditions, are always higher than the thermodynamic energy required for thermally inducing the phase transition.
- The phonon entropy-driven phase transition found in equilibrium in [104] is perfectly compatible with the findings of the ultrafast XDS experiment in Chapter 4.
- The phonon stiffening found when heating the R phase in [104] is also observed when photo-exciting the metallic state in the time-resolved XAS measurements in Chapter 4, reflected in the broadening of the π^* states.

Although several claims have been made for the existence of a monoclinic metallic phase and, hence, for the electronic nature of the phase transition, the evidence provided has been mostly indirect, based on decoupled transition temperatures and threshold fluences. As a whole, this thesis has shown that the apparent decoupled transitions can be explained by experimental factors, rather than by truly intrinsic properties of VO_2.

It is important to notice that the suggestion of VO_2 as a typical Mott insulator, in which electronic correlations are the main responsible for the exhibited properties, first arose due to the failure of band-theory-based DFT calculations in correctly describing the ground state of VO_2. However, this thesis has demonstrated that with the later advances in theoretical simulations, such descriptions have become possible, both statically and out of equilibrium. This, together with the suggested transition mechanism, which challenges the simple conception of fast processes being necessarily of electronic nature, discredit the foundations for electron-electron interactions as the main trigger for the phase transition of VO_2. Instead, a Peierls distortion driven by the competition between the lower enthalpy of the insulating phase with the higher entropy of the metallic state is perfectly compatible with the observations and new calculations of the light- and thermally induced phase transitions.

Outlook

While this work has provided a thorough examination of the phase transition, there are still many further avenues for investigation:

- While bulk single crystals are expected to recover within the repetition rates generally employed in pump-probe measurements, this is not the

case for free-standing thin films. Equivalent measurements as those conducted in Chapter 3 are required to study the dynamics of thin films on substrates.

- Whereas in Chapter 2 the reversibility of the domain landscape was established after thermally cycling the sample, the process of domain recovery after ultrafast photoexcitation remains still unknown. In order to include this parameter in the thermal model of Chapter 3, a combination of soft X-ray holography with a femtosecond optical laser could be employed for imaging the domain distribution before and after photo-excitation. Such reversibility would stand as a key point for the light-control of VO_2 for technological applications.
- Extending the time-resolved XAS experiments to the femtosecond timescales would reveal the dynamics of the relevant states involved in the phase transition, namely, the $d_{\|}$ and π^* states, immediately after photoexcitation.
- Ultrafast XDS measurements with a higher temporal resolution could reveal the fundamental time scales of phonon response. This crucial question is relevant not only for the understanding of VO_2, but of every material undergoing structural transitions in which lattice entropy plays a major role.
- The model proposed in Chapter 4 for an order-disorder phase transition in VO_2 predicts slower temporal dynamics of the transformation when the sample is held at lower base temperatures. Conducting the same ultrafast XDS measurements at $\sim 100\,\mathrm{K}$ could easily verify this behaviour. If true, and VO_2 reaches in fact a crossover point into a displacive transition, this would open up new options for coherent control of the phase transition, as the lower temperatures could be exploited for reducing the impact from disorder.
- Conducting pump-probe experiments in doped or highly strained samples would enable the measurement of the M_2-R phase transition, and compare the transient dynamics with those observed in the M_1-R transition.

All these approaches could be implemented in a very near future. Having a full comprehension of the mechanism behind the insulator-metal phase transition in VO_2 will shed light into the physics behind the exotic properties of other complex materials, such as high-temperature superconductors. Furthermore, the techniques and concepts developed in this thesis can be used to study the transient response of other materials in order to build a unified picture on how

their properties can be controlled on demand.

A | Towards time-resolved holography

The work in this thesis provides a thorough study of the properties of VO_2 and the insulator-metal transition. Employing such a wide range of techniques makes this a very complete investigation, as they enable to probe the different degrees of freedom interacting across the phase transition in VO_2. The ultimate goal of this research has been to extend the holographic imaging technique to the time domain in order to directly visualize the photo-induced phase transformation in real time. This approach would combine all the knowledge acquired from the results of previous chapters in a single experiment sensitive to electronic and structural degrees of freedom, and merging high spectral, spatial, and temporal resolution.

While the experiment presented in Chapter 2 provided a description of phase separation and domain growth during the thermal phase transition, the aim now is to determine how these phases dictate the dynamics of the ultrafast phase transition of VO_2, both extrinsic, in the form of grain boundaries and interfaces, as well as intrinsic, in the form of phase coexistence.

The extremely bright and ultrafast X-ray pulses delivered by free-electron lasers offer a unique opportunity to implement lensless imaging techniques into a pump-probe setup. Femtosecond imaging with the use of FELs as the probe source has already been exploited for more than ten years [119–121]. Furthermore, the Fourier-transform holography technique presented in Chapter 2, in transmission geometry, has also been successfully performed in the femtosecond time domain by collaborators of this work [122, 123]. This method is expected to offer numerous advantages over previous time-resolved imaging experiments on VO_2 using optical techniques [124]. On one hand, the available temporal resolution is higher, and, on the other hand, it will allow for the simultaneous probing of electronic and structural features, while providing element specificity. This chapter briefly presents the first attempts made to

perform time-resolved holographic imaging on VO_2 together with the reasons for the unsuccessful results and corresponding solutions.

The measurements were carried out at the SXR end-station [125] at the Linac Coherent Light Source X-ray FEL, using 800 nm pump pulses and soft X-ray probe pulses with energies across the vanadium L- and oxygen K-edges and sub-100 fs temporal resolution. The focusing and, hence, fluence of the X-ray pulses is tunable, and the large photon flux of this beamline enables also to measure in the single-shot regime. The samples are free-standing thin films mounted on the same mask-sample ensemble described in Section 2.3.1, which was enclosed within a vacuum chamber and connected to a heating stage. The images are recorded by a CCD camera in the same geometry as in the static experiment, so that a spatial resolution in the sub-50-nm range over a wide field of view of 2 µm is expected. Figure A.1 shows the holography images obtained at this beamline, proving the feasibility of the experiment.

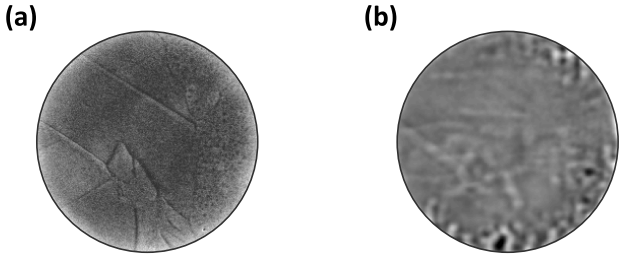

Fig. A.1: Comparison of the SEM with the holographic image obtained at LCLS. (a) SEM of the sample. **(b)** Image of the sample measured at room temperature by holographic imaging.

The reason for not achieving success in imaging the femtosecond dynamics of domain formation is twofold. Firstly, the initial attempts were carried out before the study in Chapter 3 of the recovery dynamics of these free-standing thin films of VO_2. As a result, despite the relatively low pump-laser repetition rate, of 120 Hz, it has been demonstrated in this thesis that under vacuum conditions, a repetition rate as low as 50 Hz leads to an increase of the initial temperature of the sample. This, together with the fact that X-ray pulses were generally tightly focused to ensure enough photon counts on the sample area for high-quality images, caused the combination of the pump and probe pulses to excite the sample with much higher fluence than that considered. As a result, the initial state of the sample was not the insulating phase, but it was most likely already permanently switched into the metallic state. It is important to note that domains are only distinguishable within the coexistence region, and this range is a relative narrow range of temperatures or, in this case, pump

fluences. Therefore, a strict control over the excitation densities is required for observing the right dynamics.

On the other hand, once the heat accumulation issue was minimized, the second problem arose, related to sample morphology. The samples employed in the static imaging experiments, grown by pulsed laser deposition, consist of regions with micron-sized crystals among smaller nanoscale crystallites, as shown in Figs. 2.9 and 2.12. The domain growth was found indeed in these larger crystals within the films. However, most of the samples employed for this experiment at LCLS present a different topology. Figure A.2 shows the SEM images of some of the samples used. Image in Fig. A.2(a) corresponds to a sample grown by sputtering deposition, and Figs. A.2(b), (c), and (d) to samples obtained by PLD processes. As it can be observed, the only film that exhibits larger crystals, on micrometer length scales is (d), which belongs to the same batch as those employed in the static imaging experiments. And, in fact, this is the only one where metallic domains are visible. In the other samples, with a more uniform polycrystalline structure and hence, much smaller grains, it is not possible to observe domain growth with this 50-nm-resolution technique.

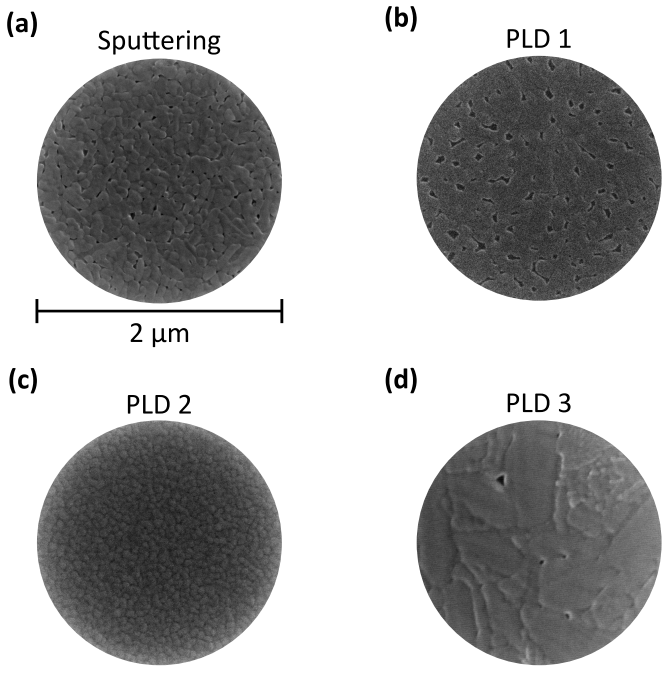

Fig. A.2: SEM image of a thin sample used for time-resolved holography. **(a)** Sample grown by sputtering deposition. **(b)**, **(c)**, **(d)** Thin-film samples grown by pulsed laser deposition.

Although the unsuccessful attempt, negative results should also be regarded as positive findings. Imaging domain growth with holography requires samples that are formed by crystallites relatively large with respect to the field of view, so that domain sizes, which generally span the sizes of the crystals, lie above the experimental resolution provided by the holography setup. Furthermore, the phase transition threshold under the specific laser and vacuum conditions needs to be properly calibrated, as the fluence region in which domains are expected to be visible is quite narrow. Having these parameters determined, it will be possible to successfully image domain dynamics in real time across the photo-induced phase transition in VO_2 in a very near future.

Abbreviations

AIMD	**A**b **I**nitio **M**olecular **D**ynamics
CDMFT	**C**luster **D**ynamical **M**ean- **F**ield **T**heory
CDI	**C**oherent **D**iffraction **I**maging
DFT	**D**ensity **F**unctional **T**heory
DOS	**D**ensity **O**f **S**tates
FEL	**F**ree-**E**lectron **L**aser
FFT	**F**ast **F**ourier **T**ransform
FTH	**F**ourier **T**ransform **H**olography
IMT	**I**nsulator-**M**etal **T**ransition
LDA	**L**ocal **D**ensity **A**pproximation
MD	**M**olecular **D**ynamics
MIR	**M**id **I**nfra**R**ed
OPA	**O**ptical **P**arametric **A**mplifier
ROI	**R**egion **O**f **I**nterest
SEM	**S**canning **E**lectron **M**icroscopy
SXR	**S**oft **X**-**R**ay
TMO	**T**ransition-**M**etal **O**xide
UED	**U**ltrafast **E**lectron **D**iffraction
XAFS	**X**-ray **A**bsorption **F**ine **S**tructure
XAS	**X**-ray **A**bsorption **S**pectroscopy
XDS	**X**-ray **D**iffuse **S**cattering

Publications

The work presented in this thesis comprises the following publications:

Chapter 2 Luciana Vidas, Christian M. Günther, Timothy A. Miller, Bastian Pfau, Daniel Perez-Salinas, Elías Martínez, Michael Schneider, Erik, Gührs, Pierluigi Gargiani, Manuel Valvidares, Robert E. Marvel, Kent A. Hallman, Richard F. Haglund, Jr., Stefan Eisebitt, Simon Wall. Imaging nanometer phase coexistence at defects during the insulator-metal phase transformation in VO_2 thin films by resonant soft X-ray holography, *Nano Lett.* **18**, 3449-3453 (2018).

Chapter 3 Luciana Vidas, Elías Martínez, Kent A. Hallman, Richard F. Haglund, Simon Wall. The role of heat and threshold fluences in the insulator-metal phase transition of VO_2. *In preparation.*

Chapter 4 Luciana Vidas, Daniel Schick, Elías Martínez, Daniel Perez-Salinas, Alberto Ramos-Álvarez, Kent A. Hallman, Richard F. Haglund, Jr., Simon Wall. Transient soft X-ray absorption spectroscopy of the photo-induced and heating effects in insulating and metallic states of VO_2, *Submitted.*

Simon Wall, Shan Yang, Luciana Vidas, Matthieu Chollet, James M. Glownia, Michael Kozina, Tetsuo Katayama, Thoman Henighan, Mason Jiang, Timothy A. Miller, David A. Reis, Lynn A. Boatner, Olivier Delaire, Mariano Trigo. Ultrafast disordering of vanadium dimers in photoexcited VO_2, *Science* **362**, 572-576 (2018).

Bibliography

[1] Morin, F. J. Oxides which show a metal-to-insulator transition at the neel temperature. *Phys. Rev. Lett.* **3,** 34–36 (1959).

[2] Westman, S. Note on a phase transition in VO_2. *Acta Chem. Scand.* **15,** 217 (1961).

[3] Goodenough, J. B. The two components of the crystallographic transition in VO_2. *J. Solid State Chem.* **3,** 490–500 (1971).

[4] Zylbersztejn, A & Mott, N. F. Metal-insulator transition in vanadium dioxide. *Phys. Rev. B* **11,** 4383–4395 (1975).

[5] Roach, W. R. & Balberg, I. Optical induction and detection of fast phase transition in VO_2. *Solid State Commun.* **9,** 551–555 (1971).

[6] McWhan, D. B., Marezio, M., Remeika, J. P. & Dernier, P. D. X-ray diffraction study of metallic VO_2. *Phys. Rev. B* **10,** 490–495 (1974).

[7] Budai, J. D., Tselev, A., Tischler, J. Z., Strelcov, E., Kolmakov, A., Liu, W. J., Gupta, A. & Narayan, J. In situ X-ray microdiffraction studies inside individual VO_2 microcrystals. *Acta Mater.* **61,** 2751–2762 (2013).

[8] Longo, J. M. & Kierkegaard, P. A refinement of the structure of VO_2. *Acta Chem. Scand.* **24,** 420–426 (1970).

[9] Verleur, Hans W., Barker, A. S., Berglund, C. N. Optical Properties of VO_2 between 0.25 and 5 eV. *Phys. Rev.* **172,** 788–798 (1968).

[10] Shin, S., Suga, S., Taniguchi, M., Fujisawa, M., Kanzaki, H., Fujimori, A., Daimon, H., Ueda, Y., Kosuge, K. & Kachi, S. Vacuum-ultraviolet reflectance and photoemission study of the metal-insulator phase transitions in VO_2, V_6O_{13}, and V_2O_3. *Phys. Rev. B* **41,** 4993–5009 (1990).

[11] Kucharczyk, D & Niklewski, T. Accurate X-ray determination of the lattice parameters and the thermal expansion coefficients of VO_2 near the transition temperature. *J. Appl. Crystallogr.* **12,** 370–373 (1979).

[12] Kawakubo, T. & Nakagawa, T. Phase transition in VO_2. *J. Phys. Soc. Jpn* **19,** 517–519 (1964).

[13] Eyert, V. The metal-insulator transitions of VO_2: A band theoretical approach. *Ann. der Phys.* **11,** 650–702 (2002).

[14] Wentzcovitch, R. M., Schulz, W. W. & Allen, P. B. VO_2: Peierls or Mott-Hubbard? A view from band theory. *Phys. Rev. Lett.* **72,** 3389–3392 (1994).

[15] Kittel, C. *Introduction to solid state physics* 6th (John Wiley & Sons, Inc., 1986).

[16] Ashcroft, N. W. & Mermin, N. D. *Solid state physics* (Saunders College, 1976).

[17] Hubbard, J. Electron correlations in narrow energy bands. *Proc. R. Soc. London* **276,** 238–257 (1963).

[18] Rice, T. M., Launois, H & Pouget, J. P. Comment on "VO_2: Peierls or Mott-Hubbard? A view from band theory". *Phys. Rev. Lett.* **73,** 3042 (1994).

[19] Kim, H.-T., Lee, Y. W., Kim, B.-J., Chae, B.-G., Yun, S. J., Kang, K.-Y., Han, K.-J., Yee, K.-J. & Lim, Y.-S. Monoclinic and correlated metal phase in VO_2 as evidence of the Mott transition: Coherent phonon analysis. *Phys. Rev. Lett.* **97,** 266401 (2006).

[20] Yuan, X., Zhang, Y., Abtew, T. A., Zhang, P. & Zhang, W. VO_2: Orbital competition, magnetism, and phase stability. *Phys. Rev. B* **86,** 235103 (2012).

[21] Eyert, V. VO_2: A novel view from band theory. *Phys. Rev. Lett.* **107,** 016401 (2011).

[22] Petek, H. & Ogawa, S. Femtosecond time-resolved two-photon photoemission studies of electron dynamics in metals. *Prog. Surf. Sci.* **56,** 239–310 (1997).

[23] Suh, J. Y., Lopez, R., Feldman, L. C. & Haglund, Jr., R. F. Semiconductor to metal phase transition in the nucleation and growth of VO_2 nanoparticles and thin films. *J. Appl. Phys.* **96,** 1209–1213 (2004).

[24] Narayan, J. & Bhosle, V. M. Phase transition and critical issues in structure-property correlations of vanadium oxide. *J. Appl. Phys.* **100,** 103524 (2006).

[25] Gray, A. X., Jeong, J., Aetukuri, N. P., Granitzka, P., Chen, Z., Kukreja, R., Higley, D., Chase, T., Reid, A. H., Ohldag, H., Marcus, M. A., Scholl, A., Young, A. T., Doran, A., Jenkins, C. A., Shafer, P., Arenholz, E., Samant, M. G., Parkin, S. S. & Dürr, H. A. Correlation-driven insulator-metal transition in near-ideal vanadium dioxide films. *Phys. Rev. Lett.* **116,** 116403 (2016).

[26] Prieur, J., Seznec, P. & Ziolkiewicz, S. Temperature variation of ultrasonic attenuation and phase velocity in VO_2 and V_2O_3 crystals. *J. Phys. Lettres* **38,** 25–28 (1977).

[27] Wu, J., Gu, Q., Guiton, B. S., de Leon, N. P., Ouyang, L. & Park, H. Strain-induced self organization of metal-insulator domains in single-crystalline VO_2 nanobeams. *Nano Lett.* **6,** 2313–2317 (2006).

[28] Guo, H., Chen, K., Oh, Y., Wang, K., Dejoie, C., Syed Asif, S. A., Warren, O. L., Shan, Z. W., Wu, J. & Minor, A. M. Mechanics and dynamics of the strain-induced M1-M2 structural phase transition in individual VO_2 nanowires. *Nano Lett.* **11,** 3207–3213 (2011).

[29] Atkin, J. M., Berweger, S., Chavez, E. K., Raschke, M. B., Cao, J., Fan, W. & Wu, J. Strain and temperature dependence of the insulating phases of VO_2 near the metal-insulator transition. *Phys. Rev. B* **85,** 020101 (2012).

[30] Sohn, J. I., Joo, H. J., Ahn, D., Lee, H. H., Porter, A. E., Kim, K., Kang, D. J. & Welland, M. E. Surface-stress-induced Mott transition and nature of associated spatial phase transition in single crystalline VO_2 nanowires. *Nano Lett.* **9,** 3392–3397 (2009).

[31] Zhang, S., Chou, J. Y. & Lauhon, L. J. Direct correlation of structural domain formation with the metal insulator transition in a VO_2 nanobeam. *Nano Lett.* **9,** 4527–4532 (2009).

[32] Tselev, A, Luk'yanchuk, I. A., Ivanov, I. N., Budai, J. D., Tischler, J. Z., Strelcov, E., Kolmakov, A. & Kalinin, S. V. Symmetry relationship and strain-induced transitions between insulating M1 and M2 and metallic R phases of vanadium dioxide. *Nano Lett.* **10,** 4409–4416 (2010).

[33] Cao, J., Fan, W., Chen, K., Tamura, N., Kunz, M., Eyert, V. & Wu, J. Constant threshold resistivity in the metal-insulator transition of VO_2. *Phys. Rev. B* **82,** 241101 (2010).

[34] Wei, J., Wang, Z., Chen, W. & Cobden, D. H. New aspects of the metal-insulator transition in single-domain vanadium dioxide nanobeams. *Nat. Nanotechnol.* **4,** 420–424 (2009).

[35] Cao, J., Ertekin, E., Srinivasan, V., Fan, W., Huang, S., Zheng, H., Yim, J. W., Khanal, D. R., Ogletree, D. F., Grossman, J. C. & Wu, J. Strain engineering and one-dimensional organization of metal-insulator domains in single-crystal vanadium dioxide beams. *Nat. Nanotechnol.* **4,** 732–737 (2009).

[36] Cao, J., Gu, Y., Fan, W., Chen, L. Q., Ogletree, D. F., Chen, K., Tamura, N., Kunz, M., Barrett, C., Seidel, J. & Wu, J. Extended mapping and exploration of the vanadium dioxide stress-temperature phase diagram. *Nano Lett.* **10,** 2667–2673 (2010).

[37] Marezio, M., McWhan, D. B., Remeika, J. P. & Dernier, P. D. Structural aspects of the metal-insulator transitions in Cr-doped VO_2. *Phys. Rev. B* **5,** 2541–2551 (1972).

[38] Pouget, J. P., Launois, H., D'Haenens, J. P., Merenda, P. & Rice, T. M. Electron localization induced by uniaxial stress in pure VO_2. *Phys. Rev. Lett.* **35,** 873–875 (1975).

[39] Park, J. H., Coy, J. M., Kasirga, T. S., Huang, C., Fei, Z., Hunter, S. & Cobden, D. H. Measurement of a solid-state triple point at the metal-insulator transition in VO_2. *Nature* **500,** 431–434 (2013).

[40] Jones, A. C., Berweger, S., Wei, J., Cobden, D. & Raschke, M. B. Nano-optical investigations of the metal-insulator phase behavior of individual VO_2 microcrystals. *Nano Lett.* **10,** 1574–1581 (2010).

[41] Arcangeletti, E., Baldassarre, L., Di Castro, D., Lupi, S., Malavasi, L., Marini, C., Perucchi, A. & Postorino, P. Evidence of a pessure-induced metallization process in monoclinic VO_2. *Phys. Rev. Lett.* **98,** 196406 (2007).

[42] Yao, T., Zhang, X., Sun, Z., Liu, S., Huang, Y., Xie, Y., Wu, C., Yuan, X., Zhang, W., Wu, Z., Pan, G., Hu, F., Wu, L., Liu, Q. & Wei, S. Understanding the nature of the kinetic process in a VO_2 metal-insulator transition. *Phys. Rev. Lett.* **105,** 226405 (2010).

[43] Laverock, J, Kittiwatanakul, S, Zakharov, A. A., Niu, Y. R., Chen, B, Wolf, S. A., Lu, J. W. & Smith, K. E. Direct observation of decoupled structural and electronic transitions and an ambient pressure monoclinic metallic phase of VO_2. *Phys. Rev. Lett.* **113,** 216402 (2014).

[44] Biermann, S, Poteryaev, A, Lichtenstein, A. I. & Georges, A. Dynamical singlets and correlation-assisted Peierls transition in VO_2. *Phys. Rev. Lett.* **94,** 026404 (2005).

[45] Cavalleri, A, Tóth, C., Siders, C. W., Squier, J. A., Ráksi, F, Forget, P & Kieffer, J. C. Femtosecond structural dynamics in VO_2 during an ultrafast solid-solid phase transition. *Phys. Rev. Lett.* **87,** 237401 (2001).

[46] Cavalleri, A, Dekorsy, T., Chong, H. H. W., Kieffer, J. C. & Schoenlein, R. W. Evidence for a structurally-driven insulator-to-metal transition in VO_2: A view from the ultrafast timescale. *Phys. Rev. B* **70,** 161102 (2004).

[47] Hilton, D. J., Prasankumar, R. P., Fourmaux, S., Cavalleri, A., Brassard, D., El Khakani, M. A., Kieffer, J. C., Taylor, A. J. & Averitt, R. D. Enhanced photosusceptibility near T_c for the light-induced insulator-to-metal phase transition in vanadium dioxide. *Phys. Rev. Lett.* **99,** 226401 (2007).

[48] Kübler, C., Ehrke, H., Huber, R., Lopez, R., Halabica, A., Haglund, R. F. & Leitenstorfer, A. Coherent structural dynamics and electronic correlations during an ultrafast insulator-to-metal phase transition in VO_2. *Phys. Rev. Lett.* **99,** 116401 (2007).

[49] Pashkin, A., Kübler, C., Ehrke, H., Lopez, R., Halabica, A., Haglund, R. F., Huber, R. & Leitenstorfer, A. Ultrafast insulator-metal phase transition in VO_2 studied by multiterahertz spectroscopy. *Phys. Rev. B* **83,** 195120 (2011).

[50] Tao, Z., Han, T.-R., Mahanti, S., Duxbury, P., Yuan, F., Ruan, C.-Y., Wang, K. & Wu, J. Decoupling of structural and electronic phase transitions in VO_2. *Phys. Rev. Lett.* **109,** 166406 (2012).

[51] Morrison, V. R., Chatelain, R. P., Tiwari, K. L., Hendaoui, A., Bruhacs, A., Chaker, M. & Siwick, B. J. A photoinduced metal-like phase of monoclinic VO_2 revealed by ultrafast electron diffraction. *Science* **346,** 445–448 (2014).

[52] Haverkort, M. W., Hu, Z., Tanaka, A., Reichelt, W., Streltsov, S. V., Korotin, M. A., Anisimov, V. I., Hsieh, H. H., Lin, H. J., Chen, C. T., Khomskii, D. I. & Tjeng, L. H. Orbital-assisted metal-insulator transition in VO_2. *Phys. Rev. Lett.* **95,** 196404 (2005).

[53] Aetukuri, N. B., Gray, A. X., Drouard, M., Cossale, M., Gao, L., Reid, A. H., Kukreja, R., Ohldag, H., Jenkins, C. A., Arenholz, E., Roche, K. P., Dürr, H. A., Samant, M. G. & Parkin, S. S. Control of the metal-insulator transition in vanadium dioxide by modifying orbital occupancy. *Nat. Phys.* **9,** 661–666 (2013).

[54] Wegkamp, D., Herzog, M., Xian, L., Gatti, M., Cudazzo, P., McGahan, C. L., Marvel, R. E., Haglund, Jr, R. F., Rubio, A., Wolf, M. & Stähler, J. Instantaneous band gap collapse in photoexcited monoclinic VO_2 due to photocarrier doping. *Phys. Rev. Lett.* **113,** 216401 (2014).

[55] Hada, M., Okimura, K. & Matsuo, J. Characterization of structural dynamics of VO_2 thin film on c-Al_2O_3 using in-air time-resolved x-ray diffraction. *Phys. Rev. B* **82,** 153401 (2010).

[56] Baum, P., Yang, D.-S. & Zewail, A. H. 4D visualization of transitional structures in phase transformations by electron diffraction. *Science* **318,** 788–792 (2007).

[57] Wall, S, Wegkamp, D, Foglia, L, Appavoo, K, Nag, J, Haglund Jr., R. F., Stähler, J & Wolf, M. Ultrafast changes in lattice symmetry probed by coherent phonons. *Nat. Commun.* **3,** 721 (2012).

[58] Cheong, S.-W, Sharma, P. A., Hur, N, Horibe, Y & Chen, C. H. Electronic phase separation in complex materials. *Phys. B* **318,** 39–51 (2002).

[59] Dagotto, E., Hotta, T. & Moreo, A. Colossal magnetoresistant materials: The key role of phase separation. *Phys. Rep.* **344,** 1–153 (2001).

[60] Campi, G., Bianconi, A., Poccia, N., Bianconi, G., Barba, L., Arrighetti, G., Innocenti, D., Karpinski, J., Zhigadlo, N. D., Kazakov, S. M., Burghammer, M., Zimmermann, M. v., Sprung, M. & Ricci, A. Inhomogeneity of charge-density-wave order and quenched disorder in a high-T_c superconductor. *Nature* **525,** 359–362 (2015).

[61] Le Tacon, M., Bosak, A., Souliou, S. M., Dellea, G., Loew, T., Heid, R., Bohnen, K. P., Ghiringhelli, G., Krisch, M. & Keimer, B. Inelastic X-ray scattering in $YBa_2Cu_3O_{6.6}$ reveals giant phonon anomalies and elastic central peak due to charge-density-wave formation. *Nat. Phys.* **10,** 52–58 (2013).

[62] Lang, K. M., Madhavan, V., Hoffman, J. E., Hudson, E. W., Eisaki, H., Uchida, S. & Davis, J. C. Imaging the granular structure of high-T_c superconductivity in underdoped $Bi_2Sr_2CaCu_2O_{8+\delta}$. *Nature* **415,** 412–416 (2002).

[63] Ricci, A., Poccia, N., Campi, G., Joseph, B., Arrighetti, G., Barba, L., Reynolds, M., Burghammer, M., Takeya, H., Mizuguchi, Y., Takano, Y., Colapietro, M., Saini, N. L. & Bianconi, A. Nanoscale phase separation in the iron chalcogenide superconductor $K_{0.8}Fe_{1.6}Se_2$. *Phys. Rev. B* **84,** 060511 (2011).

[64] Park, J. T., Inosov, D. S., Niedermayer, C., Sun, G. L., Haug, D, Christensen, N. B., Dinnebier, R, Boris, A. V., Drew, A. J., Schulz, L, Shapoval, T, Wolff, U, Neu, V, Yang, X., Lin, C. T., Keimer, B & Hinkov, V. Electronic phase separation in the slightly underdoped iron pnictide superconductor. *Phys. Rev. Lett.* **102,** 117006 (2009).

[65] Liu, M., Sternbach, A. J., Wagner, M., Slusar, T. V., Kong, T., Bud 'ko, S. L., Kittiwatanakul, S., Qazilbash, M. M., Mcleod, A., Fei, Z., Abreu, E., Zhang, J., Goldflam, M., Dai, S., Ni, G.-X., Lu, J., Bechtel, H. A., Martin, M. C., Raschke, M. B., Averitt, R. D., Wolf, S. A., Kim, H.-T., Canfield, P. C. & Basov, D. N. Phase transition in bulk single crystals and thin films of VO_2 by nanoscale infrared spectroscopy and imaging. *Phys. Rev. B* **91,** 245155 (2015).

[66] Qazilbash, M. M., Tripathi, A., Schafgans, A. A., Kim, B.-J., Kim, H.-T., Cai, Z., Holt, M. V., Maser, J. M., Keilmann, F., Shpyrko, O. G. & Basov, D. N. Nanoscale imaging of the electronic and structural transitions in vanadium dioxide. *Phys. Rev. B* **83,** 165108 (2011).

[67] Kilcoyne, A. L., Tyliszczak, T., Steele, W. F., Fakra, S., Hitchcock, P., Franck, K., Anderson, E., Harteneck, B., Rightor, E. G., Mitchell, G. E., Hitchcock, A. P., Yang, L., Warwick, T. & Ade, H. Interferometer-controlled scanning transmission X-ray microscopes at the Advanced Light Source. *J. Synchrotron Radiat.* **10,** 125–136 (2003).

[68] Lu, M. *Nanofabrication of Fresnel zone plates for soft X-ray imaging at carbon edge.* PhD thesis (Stony Brook University, 2006).

[69] Goodman, J. W. *Introduction to Fourier optics* (McGraw-Hill Companies, Inc., 1968).

[70] Gerchberg, R. W. & Saxton, W. O. A practical algorithm for the determination of phase from image and diffraction plane pictures. *Optik (Stuttg).* **35,** 237–246 (1972).

[71] Fienup, J. R. Phase retrieval algorithms: a comparison. *Appl. Opt.* **21,** 2758–2769 (1982).

[72] Als-Nielsen, J. & McMorrow, D. *Elements of modern X-ray physics* (John Wiley & Sons, Ltd., 2001).

[73] Mills, D. M. *Third generation hard x-ray synchrotron radiation sources* (John Wiley & Sons, Inc., 2002).

[74] Miao, J., Charalambous, P., Kirz, J. & Sayre, D. Extending the methodology of X-ray crystallography to allow imaging of micrometre-sized non-crystalline specimens. *Nature* **400,** 342–344 (1999).

[75] Gabor, D. A new microscopic principle. *Nature* **161,** 777–778 (1948).

[76] McNulty, I. The future of X-ray holography. *Nucl. Inst. Methods Phys. Res. A* **347,** 170–176 (1994).

[77] McNulty, I, Kirz, J, Jacobsen, C, Anderson, E. H., Howells, M. R. & Kern, D. P. High-resolution imaging by Fourier transform X-ray holography. *Science* **256,** 1009–1012 (1992).

[78] Eisebitt, S, Lüning, J, Schlotter, W. F., Lörgen, M, Hellwig, O, Eberhardt, W & Stöhr, J. Lensless imaging of magnetic nanostructures by X-ray spectro-holography. *Nature* **432,** 885–888 (2004).

[79] Schlotter, W. F., Rick, R., Chen, K., Scherz, A., Stöhr, J., Lüning, J., Eisebitt, S., Günther, C., Eberhardt, W., Hellwig, O. & McNulty, I. Multiple reference Fourier transform holography with soft x rays. *Appl. Phys. Lett.* **89,** 163112 (2006).

[80] Gaskill, J. & Goodman, J. Use of multiple reference sources to increase the effective field of view in lensless Fourier-transform holography. *Proc. IEEE* **57,** 823–825 (1969).

[81] Abbate, M, Pen, H, Czyzyk, M. T., de Groot, F. M. F., Fuggle, J. C., Ma, Y. J., Chen, C. T., Sette, F, Fujimori, A, Ueda, Y & Kosuge, K. Soft X-ray absorption spectroscopy of vanadium oxides. *J. Electron Spectros. Relat. Phenomena* **62,** 185–195 (1993).

[82] Ruzmetov, D., Senanayake, S. D. & Ramanathan, S. X-ray absorption spectroscopy of vanadium dioxide thin films across the phase-transition boundary. *Phys. Rev. B* **75,** 195102 (2007).

[83] Koethe, T. C., Hu, Z., Haverkort, M. W., Schüßler-Langeheine, C., Venturini, F., Brookes, N. B., Tjernberg, O., Reichelt, W., Hsieh, H. H., Lin, H. J., Chen, C. T., Tjeng, L. H. & Schu, C. Transfer of spectral weight and symmetry across the metal-insulator transition in VO_2. *Phys. Rev. Lett.* **97,** 116402 (2006).

[84] Weber, C., O'Regan, D. D., Hine, N. D. M., Payne, M. C., Kotliar, G. & Littlewood, P. B. Vanadium dioxide: A Peierls-Mott insulator stable against disorder. *Phys. Rev. Lett.* **108,** 256402 (2012).

[85] De Groot, F. & Kotani, A. *Core level spectroscopy of solids* (CRC Press, 2008).

[86] De Groot, F. M. F., Grioni, M., Fuggle, J. C., Ghijsen, J., Sawatzky, G. A. & Petersen, H. Oxygen 1s x-ray absorption edges of transition-metal oxides. *Phys. Rev. B* **40,** 5715–5723 (1989).

[87] Abbate, M, de Groot, F. M. F., Fuggle, J. C., Ma, Y. J., Chen, C. T., Sette, F., Fujimori, A., Ueda, Y. & Kosuge, K. Soft-x-ray-absorption studies of the electronic-structure changes through the VO_2 phase transition. *Phys. Rev. B* **43,** 7263–7266 (1991).

[88] Strelcov, E., Tselev, A., Ivanov, I., Budai, J. D., Zhang, J., Tischler, J. Z., Kravchenko, I., Kalinin, S. V. & Kolmakov, A. Doping-based stabilization of the M2 phase in free-standing VO_2 nanostructures at room temperature. *Nano Lett.* **12,** 6198–6205 (2012).

[89] Marini, C., Arcangeletti, E., Di Castro, D., Baldassare, L., Perucchi, A., Lupi, S., Malavasi, L., Boeri, L., Pomjakushina, E., Conder, K. & Postorino, P. Optical properties of $V_{1-x}Cr_xO_2$ compounds under high pressure. *Phys. Rev. B* **77,** 235111 (2008).

[90] Abrudan, R., Brüssing, F., Salikhov, R., Meermann, J., Radu, I., Ryll, H., Radu, F. & Zabel, H. ALICE - An advanced reflectometer for static and dynamic experiments in magnetism at synchrotron radiation facilities. *Rev. Sci. Instrum.* **86,** 063902 (2015).

[91] Appavoo, K., Lei, D. Y., Sonnefraud, Y., Wang, B., Pantelides, S. T., Maier, S. A. & Haglund, Jr, R. F. Role of defects in the phase transition of VO_2 nanoparticles probed by plasmon resonance spectroscopy. *Nano Lett.* **12,** 780–786 (2012).

[92] Barla, A., Nicolás, J., Cocco, D., Valvidares, M., Herrero-Martín, J., Gargiani, P., Moldes, J., Ruget, C., Pellegrin, E. & Ferrer, S. Design and performance of BOREAS, the beamline for resonant X-ray absorption and scattering experiments at the ALBA synchrotron light source. *J. Synchrotron Radiat.* **23,** 1507–1517 (2016).

[93] Quackenbush, N. F., Paik, H., Wahila, M. J., Sallis, S., Holtz, M. E., Huang, X., Ganose, A., Morgan, B. J., Scanlon, D. O., Gu, Y., Xue, F., Chen, L. Q., Sterbinsky, G. E., Schlueter, C., Lee, T. L., Woicik, J. C., Guo, J. H., Brock, J. D., Muller, D. A., Arena, D. A., Schlom, D. G. & Piper, L. F. J. Stability of the M2 phase of vanadium dioxide induced by coherent epitaxial strain. *Phys. Rev. B* **94,** 085105 (2016).

[94] Liu, M., Wagner, M., Zhang, J., McLeod, A., Kittiwatanakul, S., Fei, Z., Abreu, E., Goldflam, M., Sternbach, A. J., Dai, S., West, K. G., Lu, J., Wolf, S. A., Averitt, R. D. & Basov, D. N. Symmetry breaking and geometric confinement in VO_2: Results from a three-dimensional infrared nano-imaging. *Appl. Phys. Lett.* **104,** 121905 (2014).

[95] O'Callahan, B. T., Jones, A. C., Hyung Park, J., Cobden, D. H., Atkin, J. M. & Raschke, M. B. Inhomogeneity of the ultrafast insulator-to-metal transition dynamics of VO_2. *Nat. Commun.* **6,** 6849 (2015).

[96] Sokolowski-Tinten, K., Bialkowski, J., Boing, M., Cavalleri, A. & von der Linde, D. Thermal and nonthermal melting of gallium arsenide after femtosecond laser excitation. *Phys. Rev. B* **58,** 805–808 (1998).

[97] Waldecker, L., Miller, T. A., Rudé, M., Bertoni, R., Osmond, J., Pruneri, V., Simpson, R. E., Ernstorfer, R. & Wall, S. Time-domain separation of optical properties from structural transitions in resonantly bonded materials. *Nat. Mater.* **14,** 991–995 (2015).

[98] Cavalleri, A., Chong, H. H., Fourmaux, S., Glover, T. E., Heimann, P. A., Kieffer, J. C., Mun, B. S., Padmore, H. A. & Schoenlein, R. W. Picosecond soft x-ray absorption measurement of the photoinduced insulator-to-metal transition in VO_2. *Phys. Rev. B* **69,** 153106 (2004).

[99] Rini, M., Hao, Z., Schoenlein, R. W., Giannetti, C., Parmigiani, F., Fourmaux, S., Kieffer, J. C., Fujimori, A., Onoda, M., Wall, S. & Cavalleri, A. Optical switching in VO_2 films by below-gap excitation. *Appl. Phys. Lett.* **92,** 181904 (2008).

[100] Mayer, B, Schmidt, C, Grupp, A, Oelmann, J, Marvel, R. E., Haglund, R. F., Oka, T, Brida, D, Leitenstorfer, A & Pashkin, A. Tunneling breakdown of a strongly correlated insulating state in VO_2 induced by intense multiterahertz excitation. *Phys. Rev. B* **91,** 235113 (2015).

[101] Cocker, T. L., Titova, L. V., Fourmaux, S, Holloway, G, Bandulet, H.-C., Brassard, D, Kieffer, J.-C., El Khakani, M. A. & Hegmann, F. A. Phase diagram of the ultrafast photoinduced insulator-metal transition in vanadium dioxide. *Phys. Rev. B* **85,** 155120 (2012).

[102] Berglund, C. N. & Guggenheim, H. J. Electronic properties of VO_2 near the semiconductor-metal transition. *Phys. Rev.* **185,** 1022–1033 (1969).

[103] Brews, J. R. Symmetry considerations and the vanadium dioxide phase transition. *Phys. Rev. B* **1,** 2557–2568 (1970).

[104] Budai, J. D., Hong, J., Manley, M. E., Specht, E. D., Li, C. W., Tischler, J. Z., Abernathy, D. L., Said, A. H., Leu, B. M., Boatner, L. a., McQueeney, R. J. & Delaire, O. Metallization of vanadium dioxide driven by large phonon entropy. *Nature* **515,** 535–539 (2014).

[105] Gupta, M., Freeman, A. J. & Ellis, D. E. Electronic structure and lattice instability of metallic VO_2. *Phys. Rev. B* **16,** 3338–3351 (1977).

[106] Gervais, F. & Kress, W. Lattice dynamics of oxides with rutile structure and instabilities at the metal-semiconductor phase transitions of NbO_2 and VO_2. *Phys. Rev. B* **31,** 4809–4814 (1985).

[107] Srivastava, R. & Chase, L. L. Raman spectrum of semiconducting and metallic VO_2. *Phys. Rev. Lett.* **27,** 727–730 (1971).

[108] Schilbe, P. Raman scattering in VO_2. *Phys. B* **316-317,** 600–602 (2002).

[109] Maurer, D., Leue, A., Heichele, R. & Müller, V. Elastic behavior near the metal-insulator transition of VO_2. *Phys. Rev. B* **60,** 13249–13252 (1999).

[110] Terauchi, H. & Cohen, J. B. Diffuse x-ray scattering due to the lattice instability near the metal-semiconductor transition in VO_2. *Phys. Rev. B* **17,** 2494–2496 (1978).

[111] Hearn, C. J. Phonon softening and the metal-insulator transition in VO_2. *J. Phys. C Solid State Phys.* **5,** 1317–1334 (1972).

[112] Cavalleri, A., Rini, M., Chong, H. H. W., Fourmaux, S., Glover, T. E., Heimann, P. A., Kieffer, J. C. & Schoenlein, R. W. Band-selective measurements of electron dynamics in VO_2 using femtosecond near-edge X-ray absorption. *Phys. Rev. Lett.* **95,** 067405 (2005).

[113] Holldack, K., Bahrdt, J., Balzer, A., Bovensiepen, U., Brzhezinskaya, M., Erko, A., Eschenlohr, A., Follath, R., Firsov, A., Frentrup, W., Le Guyader, L., Kachel, T., Kuske, P., Mitzner, R., Müller, R., Pontius, N., Quast, T., Radu, I., Schmidt, J. S., Schüßler-Langeheine, C., Sperling, M., Stamm, C., Trabant, C. & Föhlisch, A. FemtoSpeX: a versatile optical pump-soft x-ray probe facility with 100fs x-ray pulses of variable polarization. *J. Synchrotron Radiat.* **21,** 1090–1104 (2014).

[114] Schick, D., Le Guyader, L., Pontius, N., Radu, I., Kachel, T., Mitzner, R., Zeschke, T., Schüßler-Langeheine, C., Föhlisch, A. & Holldack, K. Analysis of the halo background in femtosecond slicing experiments. *J. Synchrotron Rad.* **23,** 700–711 (2016).

[115] Wall, S., Foglia, L., Wegkamp, D., Appavoo, K., Nag, J., Haglund, R. F., Stähler, J. & Wolf, M. Tracking the evolution of electronic and structural properties of VO_2 during the ultrafast photoinduced insulator-metal transition. *Phys. Rev. B* **87,** 115126 (2013).

[116] Chollet, M., Alonso-mori, R., Cammarata, M., Damiani, D., Defever, J., Delor, J. T., Feng, Y., Glownia, J. M., Langton, J. B., Nelson, S., Ramsey, K., Robert, A., Sikorski, M., Song, S., Stefanescu, D., Srinivasan, V., Zhu, D., Lemke, H. T. & Fritz, D. M. The X-ray pump–probe

instrument at the Linac Coherent Light Source. *J. Synchrotron Radiat.* **22,** 503–507 (2015).

[117] Wall, S., Yang, S., Vidas, L., Chollet, M., Glownia, M., Kozina, M., Katayama, T., Henighan, T., Jiang, M., Miller, T. A., Reis, D. A., Boatner, L. A., Delaire, O. & Trigo, M. Ultrafast disordering of vanadium dimers in photoexcited VO_2. *Science* **362,** 572–576 (2018).

[118] Lindenberg, A. M., Larsson, J, Sokolowski-Tinten, K, Gaffney, K. J., Blome, C, Synnergren, O, Sheppard, J, Caleman, C, MacPhee, A. G., Weinstein, D, Lowney, D. P., Allison, T. K., Matthews, T, Falcone, R. W., Cavalieri, A. L., Fritz, D. M., Lee, S. H., Bucksbaum, P. H., Reis, D. A., Rudati, J, Fuoss, P. H., Kao, C. C., Siddons, D. P., Pahl, R, Als-Nielsen, J, Duesterer, S, Ischebeck, R, Schlarb, H, Schulte-Schrepping, H, Tschentscher, T., Schneider, J, von der Linde, D, Hignette, O, Sette, F, Chapman, H. N., Lee, R. W., Hansen, T. N., Techert, S, Wark, J. S., Bergh, M, Huldt, G, van der Spoel, D, Timneanu, N, Hajdu, J, Akre, R. A., Bong, E, Krejcik, P, Arthur, J, Brennan, S, Luening, K & Hastings, J. B. Atomic-scale visualization of inertial dynamics. *Science* **308,** 392–395 (2005).

[119] Chapman, H. N., Barty, A., Bogan, M. J., Boutet, S., Frank, M., Hau-Riege, S. P., Marchesini, S., Woods, B. W., Bajt, S., Benner, W. H., London, R. a., Plönjes, E., Kuhlmann, M., Treusch, R., Düsterer, S., Tschentscher, T., Schneider, J. R., Spiller, E., Möller, T., Bostedt, C., Hoener, M., Shapiro, D. a., Hodgson, K. O., van der Spoel, D., Burmeister, F., Bergh, M., Caleman, C., Huldt, G., Seibert, M. M., Maia, F. R.N. C., Lee, R. W., Szöke, A., Timneanu, N. & Hajdu, J. Femtosecond diffractive imaging with a soft-X-ray free-electron laser. *Nat. Phys.* **2,** 839–843 (2006).

[120] Marchesini, S., Boutet, S., Sakdinawat, A. E., Bogan, M. J., Bajt, S., Barty, A., Chapman, H. N., Frank, M., Hau-Riege, S. P., Szöke, A., Cui, C., Shapiro, D. a., Howells, M. R., Spence, J. C. H., Shaevitz, J. W., Lee, J. Y., Hajdu, J. & Seibert, M. M. Massively parallel X-ray holography. *Nat. Photonics* **2,** 560–563 (2008).

[121] Barty, A., Boutet, S., Bogan, M. J., Hau-Riege, S., Marchesini, S., Sokolowski-Tinten, K., Stojanovic, N., Tobey, R., Ehrke, H., Cavalleri, A., Düsterer, S., Frank, M., Bajt, S., Woods, B. W., Seibert, M. M., Hajdu, J., Treusch, R. & Chapman, H. N. Ultrafast single-shot diffraction imaging of nanoscale dynamics. *Nat. Photonics* **2,** 415–419 (2008).

[122] Pfau, B., Günther, C. M., Schaffert, S., Mitzner, R., Siemer, B., Roling, S., Zacharias, H., Kutz, O., Rudolph, I., Treusch, R. & Eisebitt, S. Femtosecond pulse X-ray imaging with a large field of view. *New J. Phys.* **12,** 095006 (2010).

[123] Günther, C. M., Pfau, B, Mitzner, R, Siemer, B, Roling, S, Zacharias, H, Kutz, O, Rudolph, I, Schondelmaier, D, Treusch, R & Eisebitt, S. Sequential femtosecond X-ray imaging. *Nat. Photonics* **5,** 99–102 (2011).

[124] Dönges, S. A., Khatib, O., O'Callahan, B. T., Atkin, J. M., Park, J. H., Cobden, D. & Raschke, M. B. Ultrafast Nanoimaging of the Photoinduced Phase Transition Dynamics in VO2. *Nano Lett.* **16,** 3029–3035 (2016).

[125] Schlotter, W. F., Turner, J. J., Rowen, M., Heimann, P., Holmes, M., Krupin, O., Messerschmidt, M., Moeller, S., Krzywinski, J., Soufli, R., Fernndez-Perea, M., Kelez, N., Lee, S., Coffee, R., Hays, G., Beye, M., Gerken, N., Sorgenfrei, F., Hau-Riege, S., Juha, L., Chalupsky, J., Hajkova, V., Mancuso, A. P., Singer, A., Yefanov, O., Vartanyants, I. A., Cadenazzi, G., Abbey, B., Nugent, K. A., Sinn, H., Lning, J., Schaffert, S., Eisebitt, S., Lee, W. S., Scherz, A., Nilsson, A. R. & Wurth, W. The soft x-ray instrument for materials studies at the linac coherent light source x-ray free-electron laser. *Rev. Sci. Instrum.* **83,** 043107 (2012).

Acknowledgements

The work and achievements accomplished in this thesis would not have been possible without the great support and help from several people. First, I would like to thank Simon Wall for giving me the opportunity of joining his recently formed group for my PhD. It has been a privilege for me to be his first PhD-student and I feel lucky for having such a great support from him, both from the scientific as well as the personal side. My suggestions and complaints have always been heard and considered, and I am grateful for the trust he has placed in me and my work.

This work, a major part of it being carried at large-scale facilities abroad, has benefited from the expertise and knowledge of collaborators from outside ICFO. I would like to mention here the people in Stefan Eisebitt's group: Christian Günther, Bastian Pfau, and Daniel Schick, for their vital help in the holography experiments; the guys from the BOREAS beamline at ALBA for giving me numerous opportunities to work in their beamline: Manuel Valvidares and Pierluigi Gargiani; the people that worked with me at LCLS and SACLA in the XDS beamtimes: Mariano Trigo and Olivier Delaire; the people from the BESSY slicing beamline: Daniel Schick again, Christian Schüβler-Langeheine, Torsten Kachel, and Niko Pontius for their help during the XAS beamtimes; and the guys that provided us the VO_2 samples from Richard Haglund, Jr.'s group: Robert Marvel and Kent Hallman.

I would also like to thank all the UODS group members for making the office, lab and beamlines such nice and fun work environments, those who have left already as well as those who are still here.

Un gracias de todo corazón va a todos mis amigos, tanto los que viven aquí como los que están fuera, por darme su apoyo y cariño y tener tanta fe en mí. La mayoría no han ayudado precisamente a acelerar este trabajo, sino todo lo contrario, pero su compañía lo merecía.

Por último, mis gracias más especiales y verdaderas son para Ángel y mi familia. Ellos, que no se han perdido ni un capítulo de esta tesis, son el

verdadero pilar sobre el que se sostiene todo este trabajo.